7-8-2015

Novel Optical Diagnostic Methods for the Study of Combustion and Extinction

Kathryn R. Gosselin
University of Connecticut - Storrs, krgosselin@gmail.com

Novel Optical Diagnostic Methods for the Study of Combustion and Extinction

Kathryn Renée Gosselin, PhD

University of Connecticut, 2015

Despite the movement toward alternative and renewable energy sources, combustion is still responsible for the majority of energy production in the world. Thus, there is a need for measurements in canonical and practical flames, the results of which are used to improve modeling efforts. Laser and optical diagnostics are the benchmark of combustion research, but obtaining temporally- and spatially-resolved multi-scalar measurements in turbulent flows is complex and expensive. Measurements in practical burners present an additional challenge of optical access, which limits the number and type of diagnostics which may be used.

This work describes the development of several optical techniques for the study of combustion, including three dimensional structures, turbulent combustion, and extinction. A Cassegrain optical system and maximum entropy deconvolution method are used to produce spatially-resolved chemiluminescence images of a three-dimensional flow field. Abel inversion is used to recover spatially-resolved temporal statistics from a turbulent jet. Finally, a local extinction event is studied via various optical and modeling methods. The feasibility of indirectly measuring scalar dissipation rate in the presence of a local extinction event via laser-induced fluorescence (LIF) of a single scalar – formaldehyde – is examined, and the results are used in conjunction with computational fluid dynamics results to draw conclusions about the effect of heat transfer through an extinction edge.

Novel Optical Diagnostic Methods for the Study of Combustion and Extinction

Kathryn Renée Gosselin

B.S., University of Connecticut, 2009

A Dissertation

Submitted in Partial Fulfillment of the

Requirements for the Degree of

Doctor of Philosophy

at the

University of Connecticut

2015

APPROVAL PAGE

Doctor of Philosophy Dissertation

Novel Optical Diagnostic Methods for the Study of Combustion and Extinction

Presented by

Kathryn Renée Gosselin, B.S.

Major Advisor _____
Michael W. Renfro

Associate Advisor _____
Baki M. Cetegen

Associate Advisor _____
Chih-Jen Sung

University of Connecticut
2015

Acknowledgements

I could not have done any of this without my major advisor, Mike Renfro. Thank you for pushing me, for (repeatedly) assuring me that I would actually graduate someday, and most of all, for instilling in me the virtues of the WDES method. I am also grateful to my committee members, Professors Cetegen, Sung, Lu, and Jordan, for their guidance and support. Thank you for asking the hard questions and pushing me further.

I've had too many labmates over the past 7+ years to possibly list everyone, but you know who you are. Our countless laughs, pranks, beers, Ted's lunches, and weird lab smells have made this whole thing a heck of a lot more fun. On the subject of pranks: I hereby name Steve and James as the undisputed Prank Champions of the Renfro Lab. The Chiu Crew also receives special recognition for their ongoing, fruitful partnership with the Renfro Lab. Together, we advance science!

Although my family and friends have often not understood what I'm doing or why I'm doing it, they've been indispensable throughout this process. To my parents: thank you for pushing me in various ways – both subtle and less so – to study engineering at UConn. I can honestly say that I never dreamed of loving what I do this much, and I have you both to thank for that. To my brothers: you're the best siblings and friends I could ever ask for. I am lucky to have many other amazing friends as well, but I extend special gratitude to Kelly, my biffle and favorite classmate, for making undergrad so much fun. Finally, to Mike and Sabrina (and Isaac!): I can't possibly begin to list all you've done for me. I certainly couldn't have survived these past 6 months without your love, support, and fantastic dinners.

Last but not least, I couldn't imagine doing this without Andy, my boyfriend, best friend, adventure buddy, and partner. Thanks for putting up with me at my worst and pushing me to my best. This is *way* better than dying alone.

Table of Contents

List of Tables

List of Figures

1. Introduction

1.1 Background and Motivation

Despite the move toward alternative and renewable energy sources in recent years, combustion of fossil fuels still accounts for the overwhelming majority of energy production in the United States. The U.S. Energy Information Administration reports that in 2013, fossil fuels provided almost 82% of energy consumed in the United States (*Monthly Energy Review, October 2014*, 2014). However, the burning of fossil fuels is largely responsible for a predicted global temperature rise of 4 to 8 degrees Fahrenheit by the years 2100 (Future Climate Change, 2014). Slowing climate change requires curtailing the use of fossil fuels, which in turn demands the development of new, more efficient engine technology. This development depends heavily on the use of numerical simulations, and accurate prediction of behavior in new engine geometries and conditions is of utmost importance. Internal combustion engines are characterized by high flow rates in relatively small geometries, and thus rely upon turbulent combustion for rapid and efficient energy production. Turbulent combustion presents a number of challenges with respect to numerical simulation due to the complex interaction of chemical reactions and fluid mechanics. Mixing, reactions, and dynamic processes such as extinction occur at timescales on the order of μs or smaller and length scales on the order of μm. Although combustion simulation has advanced considerably over the past few decades, particularly with recent advances in processor speed, graphics processing unit (GPU) computing, and massively parallel computing, the ability to predict behavior in new geometries and fuels remains out of reach.

In order to improve modeling efforts, well-resolved, highly accurate measurements of temperature, velocity, and various species in turbulent flames are needed. Traditional probe methods such as thermocouples are undesirable because they disturb the flow, and the ability to capture time-resolved, spatially-resolved data in complex flow structures is difficult. Thus, much combustion research relies on optical techniques, particularly laser diagnostics. Obtaining temporally- and spatially-resolved measurements in a multi-scalar, turbulent environment is a challenge from several perspectives. First, ultrafast and high repetition rate laser systems are expensive, limiting some measurements to a handful of facilities. Data collection and processing in these systems is also complex, which reduces the flexibility of the measurements and requires expert users. Laser measurements require optical access in two or more directions, which inhibits their application in practical burners that are typically enclosed and require special optical access to be installed. Thus, there is a need to develop optical diagnostic techniques that collect similarly useful data but with lower cost, less complexity, and limited optical access, allowing measurements to be taken more easily. That quest is the focus of this dissertation.

Accurately capturing the morphology of three-dimensional flame structures is important to many applications, including understanding thermo-acoustic coupling (Broda *et al.*, 1998), characterizing the effects of flame orientation of dissipation (Karpetis and Barlow, 2005), and understanding the effects of flame curvature on propagation (Chen and Im, 1998). Techniques to measure flame shapes in two dimensions are readily available using planar laser-induced fluorescence (PLIF) (Seitzman *et al.*, 1985). Extending these measurements to three dimensions requires additional laser sheets and multiple cameras (Olofsson *et al.*, 2006), which increases the cost and complexity significantly. Alternatively, flame shapes can be estimated from natural chemiluminescence without using a laser to define the plane of interest. This simpler approach

has been used successfully in many cases where the flame is two-dimensional or axisymmetric (Luque *et al.*, 2000), but it is limited to simple flame geometries and is generally difficult to interpret in turbulent flames, which often have features of interest in multiple planes. For true three-dimensional flame surfaces, chemiluminescence imaging typically only recovers the path integrated signal, and variations in the flame along the line of sight are not resolved. Tomographic techniques have been applied to resolve out of plane variations, but these techniques require multiple viewing angles and multiple cameras to compute the contribution to signal at various planes (Gilabert *et al.*, 2007). This approach requires optical access in three or more directions, or a burner that has been built specifically for this purpose. One goal of the work in this dissertation, described in Chapter 3, is to develop a new method for measuring three dimensional flame topology from chemiluminescence with only a single direction of optical access.

In additional to structural information, temporal data is vital to understanding the behavior of turbulent flames. Time-series statistics in turbulent flames have been used to validate Large Eddy Simulation (LES) models (Renfro *et al.*, 2004), for example, and these comparisons provide a unique way to constrain turbulent combustion models. Previous work has successfully collected time series of minor species (Renfro *et al.*, 2000c), temperature (Wang *et al.*, 2008), and strain rate (Coriton and Frank, 2014), among other scalars, as well as time series of velocity (Kheirkhah and Gülder, 2013). However, these time series have been obtained almost exclusively using high repetition rate lasers. These systems are expensive, and they require optical access in multiple directions (one for laser excitation and a second for signal imaging); thus, experimental setup can be complex in practical burners with limited access. Some attempts have been made to measure spatially-resolved chemiluminescence in order to recover time series

statistics, but this work was limited to point measurements (Akamatsu *et al.*, 1999). A second goal of this dissertation, described in Chapter 4, is to develop signal processing for path-integrated chemiluminescence imaging that can be used to extract spatially resolved fluctuations (similar to Abel inversion for mean signals but extended to time-resolved signals).

In many non-premixed turbulent flames, the rapid mixing between fuel and air can exceed the time scales for chemical reactions, causing a local extinction of the flame. These local events are of interest because they can lead to global flame blowoff. Measuring scalar dissipation rate, an indicator of mixing in non-premixed flames, is vital to understanding the extinction process. In practical combustors, rapid premixing of fuel and air often produces complex flows with locally large scalar dissipation rates. In the reaction zone of the flame, these varying scalar dissipation rates alter time scales for mixing in non-premixed systems. When scalar dissipation rate exceeds a critical value that the chemical reaction rates can support, local extinction occurs (Rolon *et al.*, 1995). However, there are two complications to measuring scalar dissipation rate. First, extinction is an inherently transient process, which makes it difficult to study. Carnell and Renfro (2005) previously demonstrated that a co-annular counterflow burner can produce a stationary, off-axis local extinction point, providing a canonical two dimensional flame. Second, measuring scalar dissipation rate directly requires accurately measuring a number of major and minor species, which requires multiple simultaneous laser diagnostics. This has been done successfully (Karpetis and Barlow, 2005), but it is prohibitively expensive for the majority of laboratories. Bijjula and Kyritsis (2005) examined a number of one- and two-species measurements to see if any might be suitable as a marker for scalar dissipation rate. They discovered that formaldehyde fluorescence is a marker for scalar dissipation rate. However, these measurements were only obtained in strongly burning flames using methane as a fuel. To assess the usefulness of this

measurement for broader applications, it must be performed in the presence of an extinction event. A third goal of this dissertation, described in Chapter 5, is to examine formaldehyde fluorescence in regions of local extinction to assess its broader utility as a marker for local scalar dissipation rate.

Finally, previous work by Carnell and Renfro (Carnell, Jr. and Renfro, 2006) examined the influence of heat flux in the extinction process and determined that advection through a negative edge supported the edge at scalar dissipation rates above the centerline extinction value. This observation may provide insight into the evolution of local extinction events. However, predicting the extinction behavior of this particular negative edge burner was elusive, as the relationship between advection and scalar dissipation rate is complicated. Additionally, this analysis was only performed in flames utilizing methane as a fuel, and so the effects of varying diffusion rates must be examined more closely in order to apply this insight more broadly. The final goal of this dissertation, described in Chapter 6, is to perform axisymmetric, steady-state simulations in additional fuels in order to extend the previous analysis. The relationship between advection and extinction scalar dissipation rate in a negative edge flame will be studied, as will the impact of varying fuel diffusivity.

1.2 Research Objectives

While various diagnostic techniques exist for making spatially- and temporally-resolved measurements in turbulent flames, their application is often limited by cost, complexity, and optical access. The purpose of this work is to develop and study diagnostic methods for studying

combustion and extinction that improve upon those limitations. A narrow depth-of-field optical system has been developed and supplemented with a deconvolution algorithm to produce spatially-resolved, three-dimensional measurements of chemiluminescence. This system is capable of resolving non-axisymmetric average flame structures to a depth of field of 1 mm, it requires optical access in only a single direction, and its cost is significantly lower than a basic PLIF system (Gosselin and Renfro, 2011). Time-resolved, line-integrated chemiluminescence of a round, turbulent jet has also been examined. An Abel inversion routine has been applied to the resulting frequency spectra in order to recover spatially-resolved temporal statistics. These measurements use a high-speed camera rather than a high repetition rate laser system, so the cost and need for optical access are both reduced (Gosselin *et al.*, 2015c). Formaldehyde fluorescence measurements have been performed in the presence of a local extinction event and with various fuels to assess its utility as a marker for scalar dissipation rate. These measurements show promise for identifying and quantifying local extinction events in turbulent flames, and the measurement complexity and cost are both significantly lower than current scalar dissipation rate measurements, as is the need for optical access (Carnell, Jr. *et al.*, 2009, Gosselin *et al.*, 2013a, Gosselin *et al.*, 2015a). A local extinction event has been studied numerically in order to better understand the effects of scalar dissipation and heat loss in the extinction process. The role of heat flux, particularly advection, through a negative edge flame is examined in order to provide insight into the evolution of local extinction events (Gosselin *et al.*, 2015b).

2. Literature Review and Theoretical Background

2.1 Three-Dimensional Flame Imaging

When imaging three-dimensional, semi-transparent objects such as chemiluminescence in combustion, the depth of field of the optical system is a chief parameter in defining the out of plane resolution. With broad depth of field, line of sight integration of signal introduces interference from structures outside the plane of interest and greatly decreases the quality of the image. To overcome this, many applications rely on laser techniques such as planar laser-induced fluorescence (PLIF) or particle image velocimetry (PIV) in order to artificially create a narrow imaging plane. These methods have successfully been used to measure minor species (Watson *et al.*, 2000, Li *et al.*, 2010), temperature (Seitzman *et al.*, 1985), and velocity (Zhao *et al.*, 2004), among others. Though these methods can achieve a spatial resolution on the order of tens of μm (Shimura *et al.*, 2011), they are generally limited to imaging in a single plane, diminishing their usefulness in application where out of plane features are important. Some researchers have calculated three-dimensional flame area from planar images by studying the degree of wrinkling (Yamamoto *et al.*, 2011), while others have determined flame front orientation via two crossed PLIF sheets (Karpetis *et al.*, 2004), but these pseudo-three-dimensional measurements are limited by the assumptions required to make them. A true three-dimensional laser imaging system was created by Olofsson *et al.* (2006), who used four Nd:YAG lasers and eight individual intensified CCD cameras to create spatially- and temporally-resolved PLIF and PIV images. However, the equipment required for such an experiment limits its practical use, and this experiment requires optical access in two or more directions, which is

often difficult. The analysis of the resulting signal can be complicated due to non-uniform laser illumination and non-homogeneous temperature and quenching environments.

Another method sometimes used when three-dimensional structures are of interest is computed tomography. In this technique, a network of lasers, electrodes, x-rays, or other sensors is placed around the flame field, and variations in absorption or electrical capacitance caused by combustion are used to extrapolate the location of the flame front. Generally, this is a two-dimensional method, producing an image of only a single slice of the flame, although Gut and Wolanski (2010) expanded Electrical Capacitance Tomography to a three-dimensional application by using stacked networks of electrodes capable of sensing capacitance changes due to ions created during the combustion process. This simple, inexpensive method was useful in reproducing three-dimensional structure without the need for optical access. However, the combustor must be able to accommodate the electrodes, and spatial resolution is limited by the number of electrodes available in the experiment. Likewise, with laser absorption tomography, optical access is required around the flame, and spatial resolution is limited by the number of laser paths (Wolfe and Byer, 1982).

An even simpler approach is that of traditional chemiluminescence imaging, which requires optical access in only one direction. Flame emission imaging can be applied to a variety of experiments, including those confined to small spaces, and is significantly less demanding in terms of equipment and analysis. Moreover, the in-plane spatial resolution can be very high, limited only by the size of the camera chip, magnification, and true optical resolution. Unfortunately, the technique is affected by line-of-sight integration, which decreases the quality of the image and typically destroys out-of-plane spatial resolution. In axisymmetric cases, an Abel transform can be used to remove the effects of line of sight integration, as described in

(VanDerWege *et al.*, 1999). However, this approach fails when the flame is not axisymmetric, particularly when deviations from axisymmetry are of interest, as in turbulent flows.

Several attempts have been made to extend chemiluminescence imaging to three dimensions. One approach utilized a single planar image and various assumptions to extrapolate measured properties across the entire flame. Veynante *et al.* (2010) attempted to reconstruct flame surface densities across a flame field using a single planar image. To do so, it was assumed that the flames were statistically two-dimensional, and that the measured plane was a plane of symmetry, either by rotation or translation. Similarly, Brisley *et al.* (2005) extended two-color radiation thermometry from a single camera to three dimensions by assuming rotational symmetry. While both of these techniques were successful, they were limited to symmetric applications.

The symmetry issue was addressed by Bheemul *et al.* (2002, 2005), who placed three CCD cameras at various locations around the flame field, similar to computed tomography. A combination of processing algorithms, including edge detection, contour extraction, and mesh generation were used to reconstruct the three-dimensional surface structure. More recently, Upton *et al.* (2010) performed similar experiments on turbulent flame fields, capturing three-dimensional, high-resolution images of turbulent flame structure. Though these methods were successful in determining the surface flame structure, they required multiple directions of optical access and multiple cameras operating simultaneously. In the latter case, 6 cameras were used, and 180 degrees of optical access were required (Upton *et al.*, 2010).

Another approach has recently been attempted by Bolan *et al.* (2014), who used a plenoptic camera, often called a light-field camera, which is capable of capturing images in multiple focal planes simultaneously. Rather than a single large objective lens focusing a single focal plane

onto a camera chip, a plenoptic camera uses a microlens array over a subdivided chip to capture angular ray information that is then used to reconstruct images from several focal lengths. They have had some success with this; however, they have shown that when reconstructing images, out-of-plane and cross-plane interference still plays a large role. The depth of field of any of the focal planes was at least 40 mm (Bolan *et al.*, 2014). That is, objects that were 40 mm out of focus still contributed significantly to the image.

In an attempt to remove this out of plane interference via processing, one group utilized optical sectioning, in which a simple single-lens system with a CCD camera was used to image a flame field. By translating the camera and lenses forward and backward, a series of images was produced, each one focused at a different known depth within the flame. Then, a linear deconvolution algorithm was used to reconstruct the three-dimensional structure. This method, as exercised by Zhou *et al.* (2011), recognized that the image produced by focusing on a particular plane is influenced by all out-of-focus portions of the object, and that by combining a series of such images and accounting for out-of-focus contributions, a closed system is created. Thus, a three-dimensional structure may be determined by deconvolution. In this case, the combination was successful in reconstructing measured three-dimensional temperature data; however, it was still affected by line-of-sight integration, which limits the resolution.

In an attempt to reduce line-of-sight integration during the data collection phase rather than during processing, one group used a novel optical approach: a Cassegrain imaging system. Cassegrain systems, which consist of concave and convex mirrors arranged on a single optical axis as shown in Fig. 2.1 have long been used in telescopes and are known for their narrow depth of field due to the placement of the convex mirror in the line of sight. Recently, Akamatsu *et al.* (1999) showed that they can be modified for use at short working distances. These systems are

also advantageous because the curvature and location of the two mirrors may be chosen as to virtually cancel any spherical aberration, which decreases the size of the circle of least confusion, illustrated in Fig. 2.2, and increases the resolution of the optical system. Akamatsu *et al.* (1999) found that such a system can attain a resolution approximately three orders of magnitude finer than an equivalent single lens system, such as the one used by Zhou *et al.* (2011). Additionally, a Cassegrain system is not subject to chromatic aberration as its surfaces are reflective, rather than transmissive. The translation of either mirror also moves the focal plane in a predictable way, which can be used for flame scanning, similar to the work of Zhou *et al.* (2011). A Cassegrain system has previously been used to obtain spatially-resolved chemiluminescence and ion current time series at individual points in a turbulent Bunsen flame (Akamatsu *et al.*, 1999), but this was not extended to planar or three-dimensional images.

In order to improve 3-D object recovery from a measured image, a maximum entropy deconvolution algorithm, often called the maximum entropy method (MEM), is used in this work. In image processing via deconvolution, the data set to be deconvoluted (i.e. the image) is often incomplete and/or noisy, which means that the 3-D object solution may not exist, and if it does exist, it is very likely non-unique. In order to solve the issue of existence, the solution constraints may be relaxed, so that it is no longer limited by noisy or missing data. However, this may cause the solution to be non-unique. In this situation, MEM algorithms choose the best solution based on maximizing the total entropy of the solution, which is equivalent to minimizing the information in the solution (Wu, 1997).

In statistical mechanics and thermodynamics, entropy is a measure of the disorder in a thermodynamic system, given by the Boltzmann relation

$$S = k_B \ln W \tag{2.1}$$

where S is entropy, k_B is the Boltzmann constant, and $W$is the number of possible microstates within the given system (Laurendeau, 2005). In the field of information theory, a similar quantity, H, is a measure of the uncertainty in an information source. This is commonly referred to as entropy and, for a system of n units of information (often pixels), is given by

$$H(p_1, \dots, p_n) = -k \sum_{i=1}^{n} p_i \log p_i \tag{2.2}$$

where k is an arbitrary coefficient usually set to be unity, and p_i is the prior probability that a random variable X assumes the value x_i. In addition to maximizing entropy, MEM algorithms include other constraints, such as conservation of energy and fit to a priori information about the data (Wu, 1997). One of the most important principles of data inversion is that the solution should incorporate all relevant data – that is, the image to be inverted – but be as noncommittal as possible with respect to missing data. That is, the chosen solution should be the most probable with respect to available data, without making any additional assumptions about missing data (Bevensee, 1993).

MEM as applied to image processing uses comparisons between the measured image and a reconstruction of the object convoluted with a known point spread function to adjust the reconstruction incrementally based on the entropy of the image as well as the mean squared error between the original image and the projection of the reconstruction. This method was first applied to optical signals by Frieden (1972), who used it to restore simulated, noisy images consisting of random impulses, as well as experimental line spectra data and found that its reconstruction abilities exceeded the prediction given by the Rayleigh criterion.

The method was extended to astronomy in the late 1970's, where it has found the most use. Bryan and Skilling (1980) used it to reconstruct an image of the M87 galaxy. The algorithm removed much interference, as well as defining structures that could not be seen in the original image. Later, Gull and Skilling (1984) made advances in the maximum entropy method, finding that it was an optimal tradeoff between resolution and noise. This is largely due to the fact that the algorithm tends toward the smoothest object with the least detail which still accurately produces the original image. This method's success in planar reconstruction is well-known, and in fact, Wang *et al.* (2005) attempted to use it to produce three-dimensional reconstructions of a tetragonal crystal by piecing together two-dimensional reconstructions. In this case, a series of images was taken using a high resolution electron microscope, and each image was deconvoluted separately. The resulting reconstructions were each compared with known structures determined by another, more complicated imaging method. The resulting reconstructions closely matched the known structure. While this approach was successful, it relied on a single image to produce a three-dimensional reconstruction, which was possible compared to the present work since the crystal's structure is more regular than that of a flame. To that end, this work extends the maximum entropy algorithm to a true three-dimensional reconstruction. A series of images taken at varying depths using the Cassegrain system, and the known relationships among the images were used to deconvolute all images simultaneously, creating a three-dimensional model of the object.

A useful algorithm for image processing using MEM was derived by Cornwell and Evans (1985). The numerical method in this work follows their derivation, where we describe an extension of this method to 3-D object imaging and show applications to three-dimensional flame surface reconstruction.

2.2 Turbulent Time Series Measurement

Improving turbulence models, particularly with respect to the complex turbulence-chemistry interaction, relies on experimental data from optical diagnostics of turbulent flames. For this purpose, a number of canonical burners have been developed in conjunction with the International Workshop on Measurement and Computation of Turbulent Nonpremixed Flames (TNF Workshop). Several of these canonical flames will be referred to throughout this chapter and elsewhere, so the flow conditions and monikers of several such burners have been listed in Table 2.1 for reference. These burners arise from a need to generate and document specific turbulent phenomena, and they have been studied by numerous diagnostics in order to improve the understanding and modeling of turbulence.

To reach a more complete understanding of turbulence, a variety of laser diagnostics have been utilized. Techniques such as particle image velocimetry (PIV) or laser Doppler velocimetry (LDV – also known as laser Doppler anemometry, LDA) are often used to record local velocities. Laser-induced fluorescence (LIF) or PLIF is used to record the concentrations of various minor species of interest to the combustion process. This includes hydroxyl (OH) and methylidine (CH), which form within the reaction zone and are therefore used as markers of the flame front location, as well as formaldehyde (HCHO or CH_2O), which is often used to identify ignition processes due to its role in the autoignition of many hydrocarbons, particularly methane. Additionally, nitric oxide (NO), an important combustion product and pollutant, may be measured to assess methods of reducing pollution (Law, 2006). Various techniques may be recorded to measure temperature, including Rayleigh and Raman scattering (Laurendeau, 1988). Broadly understood, there are three major approaches to measurements in turbulent flames:

instantaneous, time-averaged, and temporally-resolved. Instantaneously and time-averaged (mean) flow and scalar measurements are generally simpler and less expensive to achieve than temporally-resolved measurements, but are limited in their scope and usefulness.

For example, Barlow *et al.* (Barlow *et al.*, 2000) used a combination of Rayleigh scattering, Raman scattering, and LIF of OH and NO to analyze the behavior of a turbulent carbon monoxide/hydrogen/nitrogen jet. The reported averaged profiles showed a strong coupling between flow time scales and certain reaction time scales and yielded potentially useful conditional statistics for improving modeling of turbulence-chemistry interactions. Kiefer *et al.* (2008) used simultaneous OH and CH PLIF to examine both instantaneous flame structures and average profiles in a turbulent jet flame. Single-shot images of turbulent structures revealed a two-layer flame structure near the jet exit, as well as reignition regions downstream, and Reynolds-averaged profiles were calculated with the goal of validating numerical results. Li *et al.* (2010) used a combination of OH, CH, and HCHO PLIF to make close examinations of instantaneous flame structure in a premixed, turbulent flame and discovered that as turbulence intensity increases, the width of the HCHO signal increases due to enhanced heat and mass transfer. Several groups (Paul and Najm, 1998, Ayoola *et al.*, 2006) have shown that the overlap of hydroxyl and formaldehyde fluorescence is a good marker for heat release, which has been utilized to investigate the response of a turbulent premixed flame to acoustic coupling. Balachandran *et al.* (2005) showed that the heat release increased nonlinearly with velocity due to vortical roll-up of the shear layers, which enhanced the heat transfer.

While these studies of instantaneous or averaged flame structure are useful, they lack the temporal information necessary for a complete understanding of turbulent flames. The advent of ultrafast and high repetition rate lasers has allowed for better analysis of the turbulence-

chemistry interaction because of their improved temporal resolution and acquisition rates (Gord *et al.*, 2008). Initially, many of these studies were focused on measuring the probability density functions (PDF's) of various flow variables, although this statistic is also available from uncorrelated single shot measurements.

Various statistical measures are useful in characterizing the stochastic nature of turbulent flow. The cumulative distribution function (CDF) may be used to calculate the probability of any particular event (Kuo and Acharya, 2012). The CDF is defined by

$$F(V) = P\{u < V\} \tag{2.3}$$

That is, the cumulative distribution function describes the probability that the value of some variable, u, is less than V. From the CDF, one can calculate the probability density (or generally, distribution function), which is the derivative of the CDF.

$$f(V) \equiv \frac{dF(V)}{dV} \tag{2.4}$$

For a given probability density function, the probability that $a < u < b$ can be calculated by integrating the probability distribution function from a to b, which is the same as the difference between the difference between the CDF evaluated at a and b.

$$P\{a < u < b\} = \int_a^b f(V)dV = F(a) - F(b) \tag{2.5}$$

It is often convenient to express any time series, such as $u = u(t)$ as a function of its mean and fluctuating components, such that

$$u(t) = \bar{u} + u' \tag{2.6}$$

where $\bar{u}$ is the time-averaged value of the time series, and u' is the instantaneous deviation from this mean value. The variance of the time series, also called the mean-square fluctuation, is given by (Pope, 2011)

$$Var(u) = \sigma^2 = \int_{-\infty}^{\infty} (u(t) - \bar{u})^2 f(V) dV \tag{2.7}$$

Probability density functions of flow and scalar quantities were recorded by Hult *et al.* (2005), who studied the DLR_B burner using high-frequency PIV (HFPIV), Rayleigh scattering, and OH PLIF to track PDF's of OH fluorescence, temperature, and velocity in the presence of local extinction events. This work demonstrated that local extinction is related to deviations in the joint PDF's of temperature and OH fluorescence intensity. More recently, Coriton and Frank (2014) utilized HFPIV to measure strain rate PDF's in three conditions: an air jet, Sandia Flame C, and a burner similar to Flame C but with a reduced pilot flow in order to induce extinction events more frequently. They characterized the strain field of the three jets and determined that the strain field of the extinction-prone reacting jet showed similarities to both the stably burning flame and the non-reacting jet, which may prove useful in improving LES sub-models.

Measured PDF's have been utilized to improve models in a number of cases. Landenfeld *et al.*, for example, showed that a presumed PDF model can sufficiently capture mean properties in the Sandia D burner (Landenfeld *et al.*, 2002). Additionally, a flamelet/progress variable (FPV) model has been used in LES simulations to predict extinction and ignition of Sandia D and Sandia E. This work determined that the second moment of the presumed PDF is most important for fully capturing this behavior (Ihme and Pitsch, 2008). Understanding statistics such as PDF is clearly useful for improving various models, but this approach is limited in its impact and fails to

fully leverage the temporal resolution offered by high repetition rate lasers. Additional statistics such as power spectral density (PSD) and autocorrelation function (ACF) are needed to fully capture temporal behavior.

Given a time series $u(t)$, the power spectral density may be calculated as (Box *et al.*, 2008)

$$PSD^*(f) = \left|\mathcal{F}\big(u(t)\big)\right|^2 \tag{2.8}$$

The power spectral density describes how the fluctuations of $u(t)$ are distributed in terms of frequency. That is, the signal power contained between frequencies a and b is given by

$$Power(a < f < b) = \int_a^b PSD(f)\, df \tag{2.9}$$

In the case of discrete signals, the PSD is often normalized by the product of the sampling rate, S, and the number of samples, N. Additionally, the PSD's in this work have been normalized by the signal variance in order to compare signals in different regions and under different flow conditions.

$$PSD(f) = \frac{1}{N \cdot S}\frac{\left|\mathcal{F}\big(u(t)\big)\right|^2}{\sigma^2} \tag{2.10}$$

The power spectral density is also useful because it is a Fourier transform pair with the autocorrelation function, which is a measure of a signal's temporal correlation with itself. Generally, the autocorrelation function is given by

$$\rho(\Delta t) = \frac{\int_{-\infty}^{\infty} u(t)u(t+\Delta t)dt}{\sigma^2} \tag{2.11}$$

It may also be calculated from the PSD by

$$\rho(\Delta t) = \mathcal{F}^{-1}[PSD(f)] = \mathcal{F}^{-1}\left[\left|\mathcal{F}\left(u(t)\right)\right|^2\right] \tag{2.12}$$

From the autocorrelation function, it is possible to calculate the integral time scale, which is the largest time interval over which the signal is meaningfully correlated (Pope, 2011). This is given by integrating the autocorrelation function as a function of time interval

$$\tau_I = \int_0^\infty \rho(\Delta t)\Delta t \tag{2.13}$$

In addition to time scales, length scales are important to understanding turbulent phenomena. The largest of these length scales is the integral length scale, ℓ_0, which is the largest length scale over which the flow is meaningfully correlated. For example, in a turbulent pipe flow, the integral length scale is on the order of the diameter of the pipe. The concept of the turbulent energy states that turbulence and turbulent energy is generated by instabilities or external forces operating at approximately the integral length scale. This scale is therefore often referred to as the energy-containing scale, because it is responsible for the initial generation of turbulent kinetic energy, k. This energy then dissipates to the intermediate length scales, also known as the inertial subrange. Within this range, energy is transferred to smaller scales without any losses due to viscosity. This energy is then transferred to the smallest scales in the dissipation subrange. In this region, turbulent kinetic energy is dissipated via viscous heat loss (Kuo and Acharya, 2012).

Kolmogorov (1991) proposed several hypotheses about the energy cascade, specifically with respect to the self-similarity of energy dissipation among the scales. One of the most important outcomes of Kolmogorov's work was the -5/3 power law, sometimes called the $\kappa^{-5/3}$ law or

simply the 5/3 power law. This law states that in the inertial subrange, the kinetic energy density in wavenumber space is proportional to $\kappa^{-5/3}$, where κ is the wavenumber, which is inversely proportional to the length scale ℓ and has units of $\frac{1}{L}$. If a turbulent kinetic energy spectrum is plotted with respect to wavenumber, the inertial subrange will have a log-log slope of -5/3 (Kuo and Acharya, 2012). As will be seen in the subsequent literature review, the -5/3 power law governs a great many turbulent processes.

Ida and Ohtake (1997) demonstrated the usefulness of temporal statistics when they used high repetition rate Rayleigh scattering to measure temperature fluctuations in a turbulent hydrogen/methane diffusion flame. The calculated PSD's displayed the -5/3 law as well as the -1 power law, which governs molecular thermal diffusion, in regions with air entrapment, indicating that molecular diffusion and turbulent mixing are both of import to the turbulent-chemistry interaction. Self-similarity among the PSD's at various Reynolds numbers was also demonstrated. More recently, Wang *et al.* (2008) used high-repetition rate thermometry to determine turbulent time scales in a nonpremixed jet flame and determined that proper normalization allows the resulting downstream energy and dissipation spectra to collapse. Comparisons to model spectra proposed by Pope (2011) were also successful.

Renfro *et al.* (2000b, 2000c) were the first to calculate PSD's and ACF's, as well as integral time scales, from OH and CH fluorescence and concentration time series in canonical turbulent diffusion flames. This work determined that both OH and CH autocorrelation functions are nearly identical for regions away from the jet exit, and that in many cases they collapsed into a single curve. Consequently, it is possible that minor-species concentration fluctuations could be modeled with a single timescale for a given burner and Reynolds number (Renfro *et al.*, 2000c).

These time series statistics were compared to results from a laminar flamelet model, which used measured mean and rms values for the mixture fraction (Z) as well as realistic PDF's, PSD's, and integral time scales. The results were able to predict several complex phenomena, such as the radial dependence of OH time scales (Renfro *et al.*, 2002). Similar measurements of OH time series in a hydrogen jet were used to assess the ability of an LES model to predict integral time scales. The model was able to correctly predict normalized power spectral density shapes, but underestimated integral time scales by a factor of approximately 2, likely due to insufficient characterization of velocity and mixture fraction time scales at the inflow boundary (Renfro *et al.*, 2004).

Time series measurements have also been utilized to measure a number of other flow properties, including soot formation and flame structure. Geitlinger *et al.* (1999) used a novel combination of Rayleigh scattering and laser-induced incandescence (LII) to measure soot volume fractions, particle number densities, and mean particle radii in turbulent acetylene diffusion flames. Two-dimensional PDF's were calculated, as well as autocorrelation functions, from which turbulent length scales were calculated with the intention of model validation. Kheirkhah and Gülder (2013) examined a number of turbulent premixed V-shaped flames with Mie scattering and PIV. Flame front location, curvature, and angle were recorded, and PDF's and PSD's were calculated in order to further characterize the turbulent structure. The PSD's of flame front angle give two characteristic angles which are independent of flow conditions and cannot be calculated from the integral length scale, indicating that the flame dynamics are more complex than previously thought.

Power spectral densities are also useful for identifying sources of instability in turbulent flames, such as in the work of Janus *et al.* (2005), which utilized LDA and acetone and OH PLIF to

analyze the behavior of non-reacting and reacting non-premixed flows in a confined swirl burner. Time series of velocities were used to calculate the PSD and ACF at the locations of peak mean velocity and peak rms velocity (four locations total) and used to instabilities at several characteristic frequencies, as well as an additional frequency due to combustion.

In addition to high-speed laser diagnostics, a number of other techniques, both optical and not, have been used to obtain time series statistics in turbulent flames. One of the earliest examples is the work of Lewis and Moss (1979), which used a combination of laser Schlieren, a water-cooled Langmuir probe, and a thermocouple to measure density gradient, positive ion current, and temperature, respectively, in a confined, turbulent, premixed propane-air flame. From these time series, PDF's and PSD's were calculated, which displayed peaks at characteristic frequencies, typical of confined flows.

Much more recently, Rankin *et al.* (2014, 2013) made line-integrated infrared images of radiation from carbon dioxide and water in numerous canonical flames, from which they calculated mean radiation profiles, PDF's, ACF's, and integral length scales. Measurements in the DLR_A flame indicated that PSD's and ACF's, when normalized properly, are independent of spatial location in both upstream and downstream locations; additionally, the calculated PSD's all decay according to the -5/3 power law (Rankin *et al.*, 2013).

Giacomazzi *et al.*(2005, 2008) measured unfiltered, line-integrated chemiluminescence in turbulent, premixed and non-premixed methane flames using a photodiode. The calculated PSD's compared well with established spectra of turbulent kinetic energy and scaled similarly to temperature spectra, indicating that chemiluminescence might be a useful "natural" seeding to capture turbulent flame dynamics (Giacomazzi *et al.*, 2005). The spectra were also found to

display a -5/3 decay regardless of fuel, sensor position, or filtering (Giacomazzi *et al.*, 2008). These results indicate that chemiluminescence might be a useful, low-cost diagnostic for examining turbulent flame diagnostics; however, these results were line-integrated, and the calculated temporal statistics were limited, but the impact of this line integration on the temporal statistics was not examined.

Chemiluminescence of OH*, CH*, and C_2* can be powerful for studying flame structure and heat release (Lawn, 2000, Panoutsos *et al.*, 2009, Floyd *et al.*, 2011), and it requires optical access in only a single direction. However, it has been shown that spatial integration of chemiluminescence signals makes measurements inaccurate, such as in quantifying heat release rate (Röder *et al.*, 2012). Some attempts have been made to alleviate spatial integration by use of a narrow depth-of-field imaging system, which showed promise for spatially-resolved time series measurements of ion current in a turbulent Bunsen flame (Akamatsu *et al.*, 1999). However, these results were limited to point measurements.

Abel inversion, which calculates the single-plane contribution to a spatially-integrated signal from an axisymmetric object of interest has been used in a wide variety of applications to good accuracy (Lee and Na, 2000, Cho and Na, 2005, El Fagrich and Chehouani, 2012). Although a round turbulent jet (which many of the canonical burners are) is not instantaneously axisymmetric, its time-averaged flow variables are axisymmetric, as are many higher order statistics. Given an axisymmetric function $f(r)$ its line-of-sight projection obtained by integrating in a direction y orthogonal to the axis of symmetry is given by (Bracewell, 2004)

$$F(y) = 2\int_x^\infty \frac{f(r)rdr}{\sqrt{r^2 - y^2}} \tag{2.14}$$

If the projection $F(y)$ is measured, such as in an image of an axisymmetric, laminar flame, the radial function may be recovered by inversion of Eqn. (2.14).

$$f(r) = -\frac{1}{\pi}\int_r^\infty \frac{F(y)dy}{\sqrt{y^2 - r^2}} \tag{2.15}$$

Since imaging data is discrete, this analytical analysis cannot be applied directly; additionally, the denominator in Eqn. (2.15), $\sqrt{y^2 - r^2}$, leads to a singularity when $y = r$. Several approaches to discrete, numerical Abel inversion have been outlined and analyzed by Pretzler *et al.* (1992). The simplest and least computationally expensive method is called the matrix or area method, which discretizes the Abel inversion by representing the axisymmetric object as a series of *N* discrete rings, each with a thickness of one pixel, as shown in Fig. 2.3. The average value of the function $f(r)$ within the i^{th} ring is given by f_i. The total projection of f onto the j^{th} pixel of the imaging plane is then given by

$$F_j = \sum_{i=j}^{N} f_i a_{ij} \tag{2.16}$$

where a_{ij} is the area of the i^{th} ring that projects onto the j^{th} pixel. This method is also often referred to as Onion-Peeling (Dasch, 1992). The projection onto a flat plane can then be calculated by determining the area of each of the rings and constructing a series of linear equations that can easily be inverted to calculate the values f_j. However, Pretzler *et al.* (1992) found that this method is prone to significant noise near the centerline of the axisymmetric reconstruction, and is not recommended.

Many other numerical Abel inversion methods work from large to small radii, which has the effect of magnifying error near the center of the reconstruction. However, the Fourier method,

which is highly recommended by Pretzler *et al.* (1992) for all applications, minimizes error at all radii simultaneously by an iterative fitting method (Pretzler *et al.*, 1992). This approach assumes that the radial distribution $f(r)$ can be expanded into a series of equations, similar to a Fourier series. The theoretical Abel transform is applied to this series of equations, and a least-squares fit is used to determine the equation coefficients directly from the measured data (Pretzler, 1991). The Fourier method has been shown to be much more accurate than other discrete methods, but it is much more computationally intensive (Pretzler *et al.*, 1992). For this work, the matrix method has been compared to an open-source Fourier method algorithm (Killer, 2014).

Abel inversions have been applied to turbulent flows in several cases, such as the work of Davis (1987), which imaged a turbulent air jet using a shadowgraph method in order to relate signal to turbulent fluctuations. An Abel inversion was applied to calculate local fluctuations in signal. More recently, Doroshko *et al.* (2006) used Talbot interferometry to examine mixing in an axisymmetric, turbulent helium jet. Local average refractive index and helium concentration were determined via Abel inversion of the line-integrated and time-averaged signals, and the results showed that turbulence was inhomogeneous and anisotropic. However, these applications of the Abel inversion only examined time-averaged statistics.

Because a round turbulent jet is not instantaneously axisymmetric, local time series cannot be recovered directly via an Abel inversion in order to calculate temporal statistics. Mayrhofer and Woisetschläger (2001) attempted to subvert this limitation by performing Abel inversions on frequency spectra resulting from laser vibrometry measurements of local density fluctuations in a non-reacting free jet, with success. The inverted spectra were found to compare well to spectra resulting from local measurements of velocity via constant temperature anemometry (CTA) and pressure. Additionally, this work examined the effect of performing an Abel inversion on various

parts of the Fourier transformed data – that is, the magnitude of the Fourier spectra versus the real and imaginary parts separately – and determined that in the presence of strong acoustic waves, both real and imaginary parts must be Abel inverted. To date, no known attempts have been made to perform an Abel inversion on line-integrated temporal statistics of reacting flows, specifically to obtain ACF's and integral time scales. That application will be one focus of this dissertation in Chapter 4.

2.3 Negative Edge Flames

Turbulent flames are susceptible to wide variations in induced curvature, strain rate, and scalar dissipation rate due to velocity fluctuations. In regions of large concentration gradients, this can result in local extinction forming a hole in the flame sheet. This local extinction event can either progress to global extinction if the strain rate is sufficiently high over a large enough region of space for the hole to grow, or the hole can close, creating an unbroken flame sheet, as described by Plessing *et al.* (1998). The role of induced strain rate in both local (Rolon *et al.*, 1995, Watson *et al.*, 2000, Favier and Vervisch, 2001) and global (Shih, 2009) extinction has been shown by several investigators.

In order to better understand the behavior of a local extinction event, a flame hole may be represented as a stationary hole in a nonpremixed flame sheet with bulk in-plane flow, U_∞, as seen in Fig. 2.4. Along its perimeter, the flame hole edges interact with partially-premixed air and fuel, forming three distinct regimes. The first of these is the forwardly propagating flame edge, denoted by (A), in which the local gas velocity brings unburned, premixed air and fuel into

the flame edge. Forwardly propagating edges, which may be observed in lifted flames, represent a local flame propagation process, due to a local low scalar dissipation rate. Conversely, a negative edge flame, denoted by (B), receives burned products from the flame sheet due to the direction of the local velocity. It is subject to a high scalar dissipation rate, and is therefore a local extinction process. The stationary edge flame, denoted by (C), exists where there is no net advective flux through the flame edge. The three edge types were predicted by Buckmaster (Buckmaster, 1996), although this work did not allow for variations in strain rate or scalar dissipation rate, preventing detailed analysis of their influence.

A forwardly propagating flame edge manifests in a lifted flame, which can be easily studied in the laboratory (Kioni *et al.*, 1993, Kioni *et al.*, 1999, Puri *et al.*, 2001, Qin *et al.*, 2002, Lee *et al.*, 2003). Plessing *et al.* (1998) used a simple axisymmetric burner with coflow to stabilize a lifted laminar methane flame and studied various flow conditions using laser techniques. These measurements, in conjunction with numerical simulations, found that heat exchange among the branches of the triple flame as well as heat loss near the triple point were significant influences on flame stability.

The negative edge flame, however, does not lend itself well to evaluation in the laboratory, particularly in turbulent environments. Laser techniques have been used to observe local extinction behavior in turbulent jets (Watson *et al.*, 2000) and estimate the strain rates in these regions (Hult *et al.*, 2005). Similarly, both Pantano (2004) and Sripakagorn *et al.* (2004) used direct numerical simulation to examine the effect of scalar dissipation rate on local extinction events in turbulent jets. While these numerical simulations allow a more detailed study of flow conditions at the flame edge, the extinction events are limited to those stochastically produced by

flow fluctuations, and thus the timing and location of extinction must be captured using transient simulations.

Several attempts have been made to induce and capture negative edge flame behavior experimentally, including by Santoro *et al.* (2002) and Amantini *et al.* (2005), who induced extinction on the centerline of a counterflow burner and captured both positive and negative flame edges as the flame rapidly receded to the outer edge of the burner. Similarly, work by Cha *et al.* (2006) utilized a counterflow slot burner in an attempt to replicate the simulations of Daou *et al.* (2002). Both these experimental and numerical works were able to produce positive and negative flame edges. The latter was observed in cases of high volumetric heat loss at both high and low strain rates, suggesting heat loss as a contributing factor to this phenomenon. However, the transient nature of these experimental methods precluded detailed measurements of local conditions at the negative flame edge.

In an attempt to create a negative edge flame, Shay and Ronney (1998) intentionally misaligned a counterflow slot burner. The resultant stationary edge was found in a region of strain rate lower than that required to produce global extinction in a spatially uniform flow field. However, the geometry of the burner produced a gas flow that was predominantly parallel to the flame, making it experimentally equivalent to a stationary edge, as in Fig. 2.4. Carnell and Renfro (2005) demonstrated that a stable negative edge flame may be successfully created in a counterflow burner and outlined the conditions required for stabilization. Similarly, Yang *et al.* (2009) constructed a double-slot counterflow burner in which various fuel and oxidizer arrangements were used to create a variety of stable local extinction points. They further quantified the stable flow region and correlated propagation speed to the local Karlovitz number, which is the ratio between unstretched and stretched flame time scales (Kuo and Acharya, 2012).

As mentioned previously, scalar dissipation rate is an important value in the extinction process of non-premixed flames. Scalar dissipation rate arises from the mixture fraction formulation of combustion, wherein the reaction of fuel and oxidizer is represented by the mixture fraction, Z, rather than molar or mass fractions of all the individual species. The mixture fraction varies between 0 in the oxidizer stream and 1 in the fuel stream. This formulation has the effect of removing the reaction source term from the energy equation, which can simplify some calculations (Law, 2006). Various mixture fraction definitions have been proposed, but the one used in this work for hydrocarbons is derived from the work of (Bilger, 1988). For hydrocarbons, it is given as

$$Z = \frac{Y_C/mW_C + Y_H/nW_H + (Y_O^O - Y_O)/\nu'_{O_2}W_O}{Y_C^F/mW_C + Y_H^F/nW_H + Y_O^O/\nu'_{O_2}W_O} \tag{2.17}$$

In this general definition, Y defers to mass fractions and W refers to molecular weights. Subscripts refer to atomic carbon (C), hydrogen (H), and oxygen (O), respectively. Superscripts refer to the oxidizer (O) and fuel (F) streams. The coefficients of carbon and hydrogen are given by m and n, respectively, and ν'_{O_2} is the stoichiometric ratio of molecular oxygen. For methane, this equation reduces to

$$Z = \frac{2Y_C/W_C + Y_H/2W_H + (Y_O^O - Y_O)/W_O}{2\,Y_C^F/W_C + Y_H^F/2W_H + Y_O^O/W_O} \tag{2.18}$$

For ethane (used in Chapter 6), it is given by

$$Z = \frac{Y_C/2W_C + Y_H/6W_H + 2\,(Y_O^O - Y_O)/7W_O}{Y_C^F/2W_C + Y_H^F/6W_H + 2Y_O^O/7W_O} \tag{2.19}$$

The mixture fraction for hydrogen is given by

$$Z = \frac{Y_H/2W_H + (Y_O^O - Y_O)/W_O}{Y_H^F/2W_H + Y_O^O/W_O} \tag{2.20}$$

The scalar dissipation rate, which is a measure of the balance between reaction and diffusion in the flame front, has units of s^{-1} and is often expressed in terms of species diffusion and gradients of mixture fraction.

$$\chi = 2D\left[\left(\frac{\partial Z}{\partial a}\right)^2 + \left(\frac{\partial Z}{\partial r}\right)^2\right] \tag{2.21}$$

where D is the diffusion coefficient, and a is the axial spatial variable. However, this work will use the definition given by Boulanger and Vervisch (2002), which replaces the molecular diffusivity term with thermal diffusivity.

$$\chi = \frac{\lambda}{\rho c_p}\left[\left(\frac{\partial Z}{\partial a}\right)^2 + \left(\frac{\partial Z}{\partial r}\right)^2\right] \tag{2.22}$$

where λ is the thermal conductivity, ρ is the density, and c_p is the specific heat. Scalar dissipation rate has been shown to be an important indicator for extinction, such as in the work of Favier *et al.*, which calculated the scalar dissipation rate in a simulated diffusion flame during a quenching process and determined that scalar dissipation rises as the flame approaches extinction until it reaches a critical value, at which point the flame extinguishes (Favier and Vervisch, 2001). However, measuring scalar dissipation rate directly is difficult, as it requires measuring the concentrations of a number of major and minor species accurately, given that a gradient must be calculated, which has the effect of amplifying noise. Several groups have successfully measured scalar dissipation rate using a combination of various laser techniques, such as Long *et al.*(2006) and Karpetis *et al.*(2004). Recent work by Magnotti and Barlow (2014) demonstrated single-shot measurements of scalar dissipation rate that compared well to results from

CHEMKIN in bluff-body stabilized methane-air flames. These measurements require several simultaneous laser diagnostic techniques to be performed at high speeds, which is difficult in terms of experimental setup, complexity, and cost, and are thus unattainable for most laboratories.

Previous work (Bijjula and Kyritsis, 2005) examined fluorescence of several minor species in a counterflow diffusion flame in order to determine whether any might be a suitable marker for local scalar dissipation rate. This previous work operated on the assumption that scalar dissipation rate is directly proportional to strain rate, which in turn is inversely proportional to the square of the width of the mixing layer. Stated simply, this implies that $\chi \propto \delta^{-2}$. Thus, a species whose spatial distribution closely follows the mixing layer might be a good marker for scalar dissipation rate. This work determined that formaldehyde is a suitable marker for scalar dissipation rate in a stably burning counterflow diffusion flame. This is due to the leakage of oxygen past the flame front, leading to the production of formaldehyde on the fuel side of the flame. Furthermore, the Boltzmann fraction of the particular energy transitions grows at lower temperatures, emphasizing the mixing of oxygen. Additionally, they determined that fluorescence quenching, which is currently poorly understood for formaldehyde fluorescence (Brackmann *et al.*, 2003), has little effect on the width of the formaldehyde profile (Kyritsis *et al.*, 2004), making it a robust diagnostic for this purpose. Formaldehyde fluorescence has been used extensively in combustion studies due to its close tie to formyl radical production via $OH+CH_2O \rightarrow HCO+H_2O$, which correlates well with heat release (Ayoola *et al.*, 2006). Formaldehyde fluorescence is also an attractive diagnostic because it may be excited at 355 nm, the 3rd harmonic of an Nd:YAG laser (Fayoux *et al.*, 2005), which simplifies the experimental setup. The previous results linking formaldehyde fluorescence to scalar dissipation rate (Bijjula

and Kyritsis, 2005) have only been performed in stably burning flames. The effect of a local extinction event on formaldehyde fluorescence should be determined in order to assess the utility of this diagnostic for studying scalar dissipation rate in the extinction process. This analysis is the focus of Chapter 5

2.4 Heat Transfer in Edge Flame Stability

Previous work by Carnell and Renfro (2006) utilized simulations of a stationary negative edge flame to examine more closely the interaction between heat flux and scalar dissipation rate in the edge. Using methane as a fuel, they noted that the scalar dissipation rate at the point of extinction – defined either as the point of peak reaction rate or peak temperature gradient along the stoichiometric contour – exceeded the scalar dissipation rate for centerline extinction. In order to determine the reasons for this, they used Fluent simulations utilizing a one-step methane reaction mechanism (Carnell, Jr. and Renfro, 2006). Although these results do not quantitatively match temperatures or flame front locations from measurements, they do predict trends and general extinction behavior correctly. Carnell and Renfro (2006) were interested in the fact that simulated scalar dissipation rates at the off-axis extinction point exceeded those reached in centerline extinction simulations. In order to determine what allowed the flame to exist at higher scalar dissipation rates, they performed a detailed analysis of the steady energy equation, as in Eqn. (2.23) along the stoichiometric contour:

$$0 = -\rho c_p \left(V_r \frac{\partial T}{\partial r} + V_a \frac{\partial T}{\partial a} \right) + \lambda \left(\frac{\partial^2 T}{\partial r^2} + \frac{\partial^2 T}{\partial a^2} + \frac{1}{r} \frac{\partial T}{\partial r} \right) + \frac{\partial \lambda}{\partial r} \frac{dT}{dr} + \frac{\partial \lambda}{\partial a} \frac{\partial T}{\partial a} - \sum_i \nabla h_i \cdot \vec{J}_i + \dot{\omega}''' \Delta h \tag{2.23}$$

In equation (2.20), V_r and V_a are the radial and axial velocities, respectively, T is the temperature, ∇h_i is the enthalpy transported by the diffusion flux, $\vec{J_i}$, of the ith species, $\dot{\omega}'''$ is the reaction rate, and Δh is the enthalpy change due to reaction. First, they determined that terms arising from radial geometry, such as $\frac{\partial \lambda}{\partial r}\frac{dT}{dr}$ and $\lambda\frac{1}{r}\frac{\partial T}{\partial r}$ are negligible, indicating that the edge flame would behave similarly in a non-radial burner. Additionally, the effects of variable conductivity, $\frac{\partial \lambda}{\partial r}\frac{dT}{dr}$ and $\frac{\partial \lambda}{\partial a}\frac{\partial T}{\partial a}$, are negligible, and the rate of species diffusion, $\sum_i \nabla h_i \cdot \vec{J_i}$, is insignificant as compared to the velocities in the edge. In the presence of large local velocities, only three terms are important: radial advection ($-\rho c_p V_r \frac{\partial T}{\partial r}$), axial diffusion ($\lambda\frac{\partial^2 T}{\partial a^2}$), and volumetric heat production ($\dot{\omega}'''\Delta h$).

Based on these simplifications, the heat transfer through the edge reduces to the following for many flames:

$$0 = \lambda\frac{\partial^2 T}{\partial r^2} + \dot{\omega}'''\Delta h - V_r\frac{\partial T}{\partial r}\rho c_p \tag{2.24}$$

At the onset of extinction, the temperature decreases significantly, meaning that $\frac{\partial T}{\partial r}$ and $\frac{\partial^2 T}{\partial r^2}$ are both negative initially. However, the velocity is aligned with the negative temperature gradient in a negative edge flame, and therefore the advection term, $-V_r\frac{\partial T}{\partial r}\rho c_p$, is an energy gain in addition to volumetric heat production. Carnell and Renfro (2006) found that advection through the edge allowed the flame edge to exist at higher scalar dissipation rates than predicted by centerline extinction; however, they were unable to directly correlate or predict the advection and excess scalar dissipation rate. Additionally, these simulations were only performed with methane as a fuel, so the effects of varying thermal and molecular diffusivity could not be taken into account.

The goal of this work is to extend this work to other fuels, as well as to more clearly explain the impact of advection in these negative edges and predict the behavior of this burner.

One application of this analysis might be improving extinction criteria in the laminar flamelet model. This approach to turbulent modeling conceptualizes a turbulent flame as a series of thin, laminar flamelets embedded in a turbulent flow field. In this model, the individual flamelets are one-dimensional, and a coordinate transformation casts the flame in terms of mixture fraction. Flame stretch and strain due to turbulent processes increase the local scalar dissipation rate, χ, until it reaches a critical value, at which the flamelet will extinguish. As many individual flamelets undergo extinction, the overall reaction rate of the flame decreases, and the entire flame may extinguish (Peters, 1988). The laminar flamelet approach to nonpremixed flames was pioneered by Liñán (1974), whose asymptotic analysis of counterflow diffusion flames identified four distinct regimes: a nearly frozen regime (including ignition), a partially burning, unstable regime, a premixed flame regime, with reactant leakage, and a stable, near-equilibrium regime. This work cast the extinction process in terms of the Damköhler number, which is the ratio of diffusion or flow time to reaction time.

Chung and Law (1983) applied the same analysis to cases with varying Lewis numbers. Lewis number is a dimensionless quantity defined as the ratio of thermal to molecular diffusivity (Law, 2006). This work improved upon the extinction criterion by including the impact of reactant leakage, which can significantly influence the flame sheet temperature, and in turn, the Arrhenius reaction rate (Chung and Law, 1983). Kim and Williams (1997) recognized that non-unity Lewis numbers influence the excess or deficiency of total energy in the reaction regime due to reactant leakage. For Lewis numbers less than 1, reactant penetration increases energy in the reaction zone, and diffusive loss is diminished, making the flame less likely to extinguish.

Conversely, flames with fuels having a Lewis number greater than 1 will extinguish more easily. However, this effect was only studied in quasi-one-dimensional, stationary flames. It should be examined in the presence of a negative edge in order to assess its impact in a two-dimensional flow with advection through the extinction edge. This analysis is the focus of Chapter 6.

2.4 Tables

Table 2.1: Flow conditions of several canonical burners from the TNF Workshop. Source: (Experimental Data Archives, 2014)

Flame Name	**Fuel (% Volume)**				**Re**	D_{jet} **[mm]**	**Premixed?**	**Piloted?**
	CH_4	H_2	N_2	Air				
DLR_A	22.1	33.2	44.7	-	15,200	8	No	No
DLR_B	22.1	33.2	44.7	-	22,800	8	No	No
Sandia C	25	-	-	75	13,400	7.2	Yes	Yes
Sandia D	25	-	-	75	22,400	7.2	Yes	Yes
Sandia E	25	-	-	75	33,600	7.2	Yes	Yes

2.5 Figures

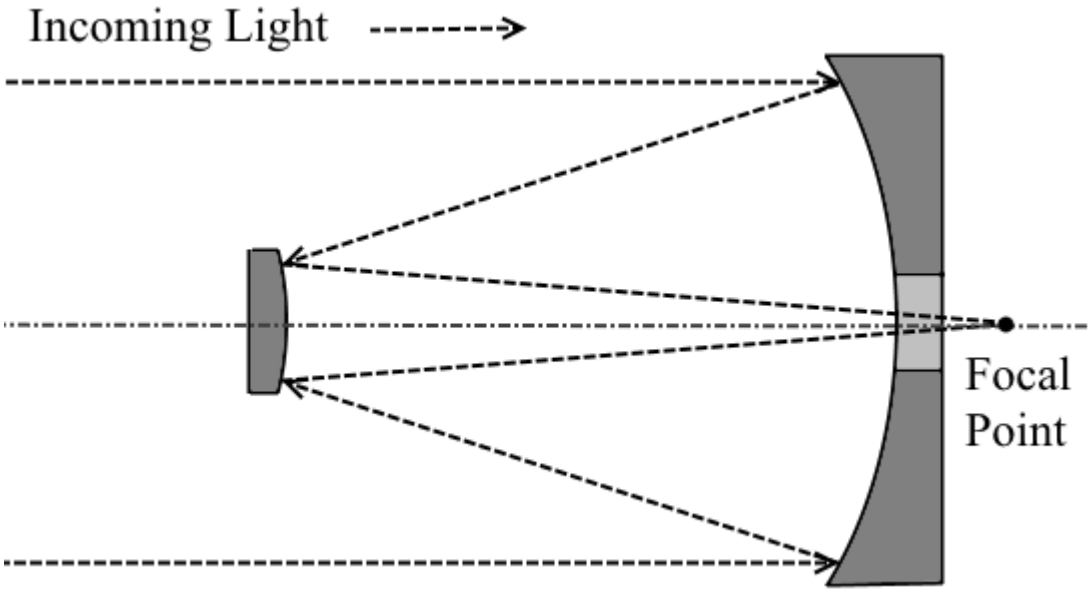

Figure 2.1: Basic Cassegrain optical system, including approximate light path.

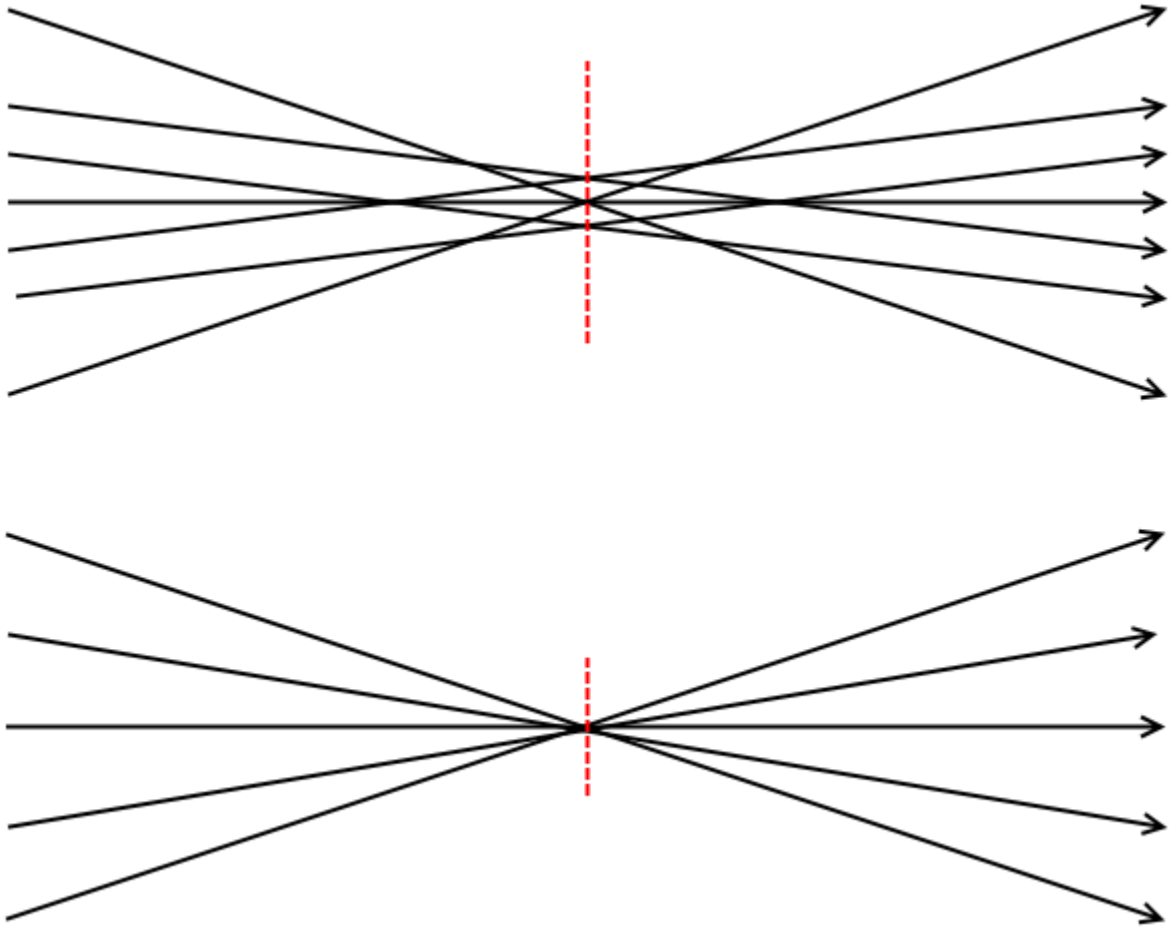

Figure 2.2: Focused rays with (top) and without (bottom) spherical aberration. The circle of least confusion is marked with a dotted vertical line.

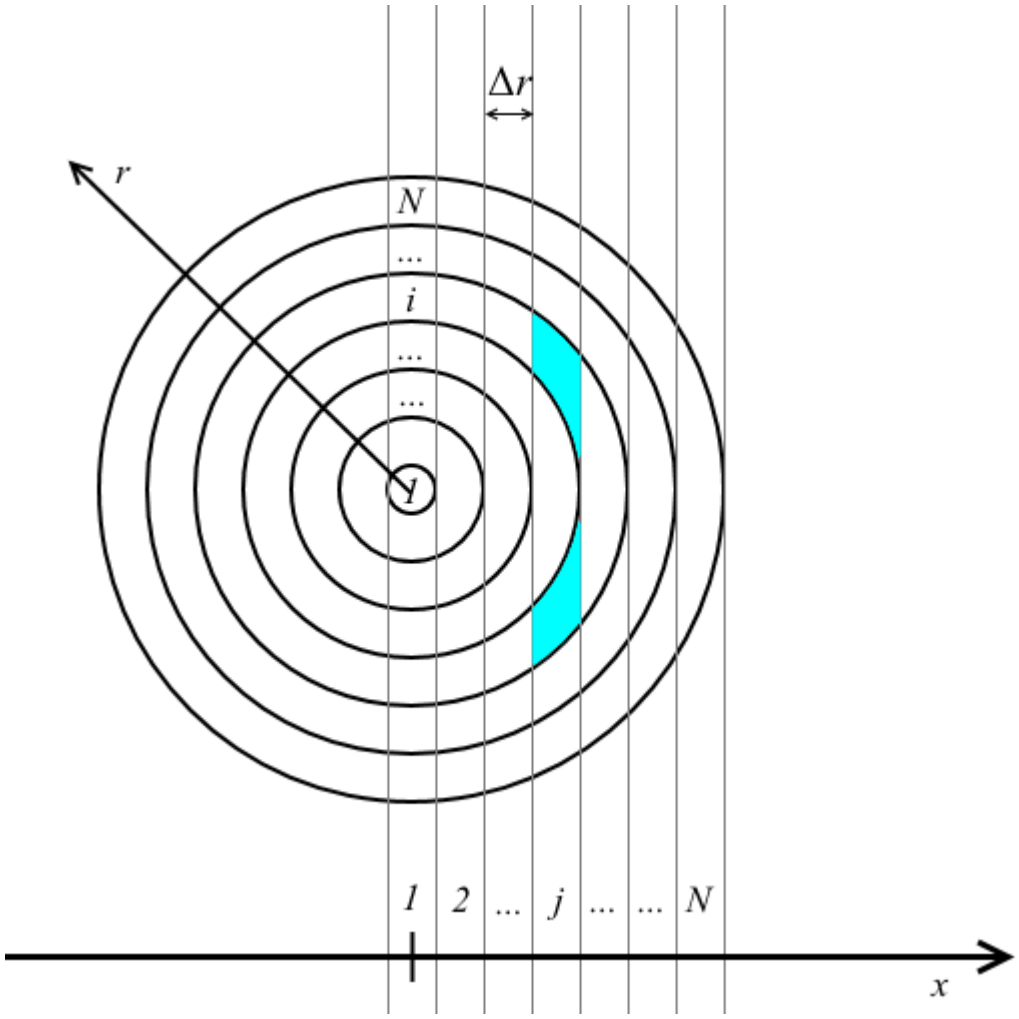

Figure 2.3: An illustration of the onion peeling method of Abel inversion. The area of the ith ring contributing to the jth pixel is highlighted.

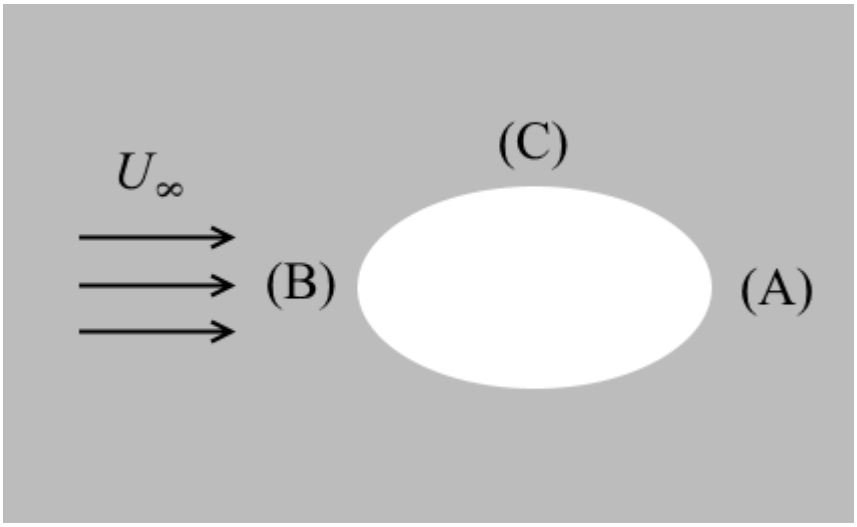

Figure 2.4: Illustration of a hole in a flame sheet, with (A) a forward edge, (B) a negative edge, and (C) a stationary edge marked.

3. Development of a Three-Dimensional, Narrow Depth-of-Field Optical Imaging System

3.1 Background and Motivation

Three-dimensional measurements of flame structure have been undertaken by various researchers, utilizing a variety of techniques. Some have extended planar laser-induced fluorescence (PLIF) measurements to three dimensions, resulting in high-resolution images of scalars, but at significant cost (Olofsson *et al.*, 2006). Others have placed networks of sensors or cameras around a flame field to capture and reconstruct three-dimensional flame structures (Veynante *et al.*, 1996, Bheemul *et al.*, 2002, Gut and Wolanski, 2010, Upton *et al.*, 2010); however, this approach requires optical access in multiple directions, which is not always feasible in practical burners. Another approach to chemiluminescence imaging is the Abel inversion (VanDerWege *et al.*, 1999), which requires optical access in only a single direction and can reconstruct local flame structure, but only for axisymmetric applications. Recently, researchers have used a light-field or plenoptic camera to simultaneously image flames at various depths, but this approach is limited by the depth of field of this system, which is on the order of 40 mm (Bolan *et al.*, 2014). Another group attempted to overcome the challenges associated with depth of field by scanning through a flame with a traditional camera and applying a maximum entropy deconvolution to remove out-of-plane interference (Zhou *et al.*, 2011). Although this approach is useful, it is still limited by the depth of field of the imaging system. Other investigators developed a narrow depth-of-field imaging system by adapting a Cassegrain optical system for use at short working distances. This system had a depth of field on the order of 1 mm, but it was limited to point measurements (Akamatsu *et al.*, 1999).

3.2 Specific Objectives

This chapter will document the development and validation of a novel narrow depth-of-field optical imaging system for imaging chemiluminescence of non-axisymmetric flame structures. The basic requirements of the technique are as follows:

1. The system should be capable of plane imaging with a standalone depth-of-field narrower than that of a traditional camera/lens system.
2. It should be capable of measuring three-dimensional structure of a steady flame without requiring that the flame be axisymmetric.
3. It should be capable of resolving flame structure to a depth of field of 1 mm, comparable to previous narrow depth-of-field chemiluminescence measurements (Akamatsu *et al.*, 1999).
4. It should be built from commercially available, inexpensive parts.
5. It should require optical access in a single direction, as to allow its application to practical burners.

First, a Cassegrain optical system was optimized using a ray-tracing algorithm to extend previous work that had been limited to point measurements to a system capable of full imaging with narrow depth of field and working distances sufficient for application in combustion. The designed system was then built and validated in a steady state flame. It was enhanced by the application of a three-dimensional maximum entropy deconvolution algorithm, which allowed the removal of out-of-plane interference. Finally, scanned slices of a non-axisymmetric flame

using this system were used to reconstruct three-dimensional flame structure with out of plane resolution of 1 mm. This work has also been described in (Gosselin and Renfro, 2011).

3.3 Cassegrain System Optimization

In order to choose appropriate optical components, the Cassegrain system was modeled using a ray-tracing algorithm written in Matlab. The ray-tracing process is mathematically simple: the various optical components are represented by geometric equations in space, and the progress of light rays, represented by vectors, through the system is calculated. For reference, a simplified Cassegrain system with pertinent dimensions and radii of curvature labeled is shown in Fig. 3.1. It should be noted that the longitudinal direction – that is, the line of sight – is defined in the z-direction.

The program is initialized by defining the geometry of the system. The object – that is, the source of the ray or rays to be traced – is defined in $\mathbb{R}^3$ by its Cartesian coordinates, (x_0, y_0, z_0) and initially set at the origin for simplicity. The concave mirror, called mirror 1, is defined as a sphere with radius of curvature, R_1, and a diameter, D_1. Its location with respect to the origin, z_1, is defined not by the center of the sphere, but the intersection of the mirror with the z-axis. The convex mirror, called mirror 2, is similarly defined by R_2, D_2, and z_2. The image plane is given by z_3.

First, the ray leaves the object location, (x_0, y_0, z_0), at an angle either chosen randomly or input by the user. It moves in the direction of mirror 1, but in the process, it can potentially be blocked by mirror 2, which is in the line of sight (note: the size of the camera, which may also block rays,

has been disregarded for the sake of optimizing the system, as its effects were shown to be small with respect to mirror 2). If it is not, its intersection with mirror 1 is calculated. If the ray successfully hits mirror 1 within its given diameter, the direction of the reflected ray is calculated. This ray moves toward mirror 2, where its intersection is calculated. If it intersects within the given diameter of mirror 2, the reflection is again calculated. This ray's intersection with the image plane is then calculated and recorded. This simplified method is outlined in a flow chart shown in Fig. 3.2, and the full code may be found in the Appendix.

The algorithm was used to optimize the system based on the following constraints:

1. All optical components must be commercially available.
2. The spherical aberration should be minimized.
3. The in-plane collection efficiency should be maximized.
4. The out-of-plane collection efficiency should be minimized.

Attempting to theoretically optimize these constraints would have been difficult, especially since the stringency of each of these requirements depends heavily on the application. Additionally, the magnification of the system affects the available configurations. Thus, an iterative scheme was used, in which 1000 rays were sent through the system at a given placement, and data about the resulting image were stored. This process was repeated for each possible configuration. The compiled data about the various arrangements were compared, and the best configurations were hand-selected based on the requirements of the given application.

The first requirement was fulfilled by compiling a list of commercially available optical components that might feasibly fulfill the needs of the system. Only the dimensions of these components were considered when optimizing. The second constraint was addressed by

calculating the radius of the spot size at the focal point resulting from the ray tracing algorithm. An example of this is seen in Fig. 3.3, which shows the results of the ray-tracing algorithm for point objects both (a) in focus and (b) 1 mm out of focus. It should be mentioned that the scale on the two images is different, and that the "hole" in Fig. 3.3(b) is a shadow of mirror 2 due to its placement in the line of sight. The size of the circle in Fig. 3.3(a), also called the circle of least confusion, should be minimized in order to minimize spherical aberration. In-plane collection efficiency was tracked by calculating the percentage of rays to reach the final source, in order to maximize the brightness of the resulting images. The final requirement was determined by calculating how quickly the "hole" in an out-of-plane image, such as in Fig. 3.3(b), grows. In order to quantify this, the ratio between the radius of the hole and the out-of-plane translation was calculated. The quick spread of this hole translates to a narrow depth of field. In the case of point measurements, a pinhole placed before the imaging plane would be used to eliminate out-of-plane rays, giving this system a standalone depth of field of less than 1 mm. In the case of planar imaging, the rays are spread over the background quickly and are progressively blocked by the second mirror. These effects all result in a narrower depth of field than a comparable single-lens system.

These constraints, as well as the magnification required for the given application, were considered holistically when choosing a configuration. The locations of the various optical components used to take the images shown in Section 3.5 are given in Table 3.1.

In addition to this optimization, the flame-scanning ability of the system was evaluated using the ray-tracing algorithm. In order to do this, the location of mirror 1 (z_1) was changed in small increments, and the location of the corresponding focal plane (z_3) was determined. An example of this procedure is shown in Fig. 3.4. Image (a) shows the focal point resulting from the ray-

tracing algorithm for a specific optical arrangement. Then, mirror 1 was translated by 1 mm, and the ray-tracing algorithm was run again. Image (b) shows the ray-tracing results at the original focal plane, and (c) shows the results at the new focal plane, 4 mm away from the new one. In this way, the relative movement of z_1 and z_3 was mapped and used to accurately define the relative movement of the mirror and the object plane relative to a fixed imaging plane. This relationship was used when performing flame-scanning, described later in this chapter. It should be noted that as mirror 1 moves, the in-plane magnification of the system may change. In the present work, this change was found to be less than 5% over the range studied; however, this change could be accounted for directly in the point spread function, as described in Section 3.3.

3.4 Experimental Setup

Based on the optimization described in Section 3.3, several optical configurations were chosen. A mirror with a diameter of 6 inches (152.4 mm) and a radius of curvature of 12 inches (304.8 mm) was chosen for mirror 1 and was purchased from Edmund Optics. This is an off-the-shelf component with an enhanced aluminum coating. For the second mirror, two mirrors were purchased to allow a range of magnifications for different applications. The first has a diameter of 1 inch (25.4 mm) and a radius of curvature of 100 mm, while the second has a diameter of 1 inch (25.4 mm) and a radius of curvature of 1000 mm. Both mirrors were purchased from CVI Melles Griot. These mirrors were made by choosing off-the-shelf BK7 substrates and applying a custom coating of enhanced aluminum.

In addition to the mirrors, a camera was selected. In some cases, the distance between mirror 2 and the imaging plane was great enough that a small, flat mirror could be used to take the imaging plane off-axis, making the size of the camera moot. However, in some configurations, such as the one used to take the images presented in Section 3.6, z_2 and z_3 were prohibitively close together, such that the camera must be placed in the line of sight. For that reason, a low-profile camera must be chosen. The first camera used was a board-level, USB-controlled, 1.3MP Monochrome 8-bit CMOS camera from Mightex Cameras. Its profile is 2 inches (50.8 mm) square, and its imaging chip is 6.66 mm by 5.32 mm, with a pixel count of 1280 by 1024. A monochrome camera was chosen in order to maximize its effective resolution, which in color cameras is reduced because the pixel count includes red, blue, and green pixels. Although this camera was useful in aligning the system and performing initial validation, it was replaced before taking final data due to issues with collection efficiency. A second camera was chosen, also from Mightex Cameras: a Compact USB2.0 Monochrome 8/12bit 1.3MP 1/3 in CCD Camera. Its profile is 39.9 mm square, and its chip is 6.26 by 5.01 mm with a pixel count of 1280 by 960. This camera was used to take the images shown in Section 3.6.

Of next concern was mounting the system. Mirror holders large and stable enough to hold mirror 1, which has a diameter of 6 inches, are expensive. Thus, a simple mirror holder was made out of a 1.5 inch (38.1 mm) thick piece of aluminum. A 1 inch (25.4 mm) deep circle with a diameter of just over 6 inches was milled into the surface, and ¼”-20 holes were drilled and tapped on each side of the mount, and set screws inserted into three of these holes were used to hold the mirror in place. The fourth ¼”-20 hole was used to attach a standard optical base to the mirror holder, in order to mount it. In order to allow for flame-scanning, the large mirror was mounted on a translation stage. The stage chosen was a linear stage from Newport Optics with a translation

range of 2 inches. It was driven by a micrometer, also from Newport Optics, with a travel range of 50 mm. The holder for mirror 2, on the other hand, was chosen to minimize its profile while still allowing for fine tuning of the mirror's orientation. A low-profile kinematic mount was purchased from Thorlabs (Compact Kinematic Mounts, 2015). This mirror allows adjustment in two axes and has a profile of approximately 1 inch (25.4 mm) square.

Imaging was done on a simple dual-flame diffusion burner, which had been constructed such that the relative locations of the two flames could be changed easily. The non-premixed fuel tubes each had an outer diameter of 0.125 in (3.18 mm) and an inner diameter of 0.095 in (2.41 mm), and with appropriate flow rates of nitrogen and methane, which were adjusted at each attempt for optimal stability and brightness, the flames themselves each had a diameter of approximately 7 mm at their widest, which was the region being imaged. The flames were arranged in a "stacked" configuration, where the flames were aligned in the plane of view of the imaging system but were separated in the depth of the image with the separation between the flames, as measured from flame center to flame center, being set to between 7 and 12 mm. Top and front views of the flames with a 9 mm separation may be seen in Fig. 3.5 taken with a conventional lens-camera system with broad depth-of-field. Note that in this conventional image, Fig. 3.5(b), it is not even apparent that there are two flames. The flames were too large to fit onto the CCD surface for the given magnification, so only a portion of the flames was imaged. The approximate three-dimensional region of interrogation is also shown by the boxes in Fig. 3.5. For each configuration, a set of images was taken by translating the larger concave mirror of the Cassegrain system 0.25 mm such that the focal plane was moved approximately 1 mm at a time. Together, the images spanned from directly in front of the flames to directly behind them as

shown in Fig. 3.5. At each location, 20 images were captured and averaged, in order to reduce the effects of any small flame movement and to reduce noise.

Prior to imaging, the three-dimensional point spread function of the optical system was determined in a method similar to that described by Shaevitz and Fletcher (2007), in which a small, fluorescent sphere is translated axially along the imaging path, and its appearance at various locations recorded. In this case, a backlit target with a diameter of approximately 750 μm was translated along the imaging path and images were collected as shown in Fig. 3.6. The PSF's were approximated by averaging radially in all directions from the center of the images since the optical system is ostensibly axisymmetric. These radial functions were measured for every combination of object and concave mirror location. A Gaussian function was fit to the measurements, and each PSF was identified by its mean, as measured from the center of the PSF, and standard deviation. The resulting fit is shown in Fig. 3.7 for an object 2 mm out of focus. The pixel counts, as measured radially from the center, are compared to the corresponding Gaussian fit. The fit shown has an R^2 value of 0.974, which was typical for all the PSF's used.

3.5 Maximum Entropy Deconvolution Algorithm

Although the Cassegrain system is capable of a narrower depth-of-field than a traditional imaging system, some out-of-plane contribution still occurs. In the previous work of Akamatsu *et al.* (1999) the authors were concerned only with point measurements, so a pinhole was used to capture only in-plane light, which made its effective depth of field even shorter than the current system. With the present imaging Cassegrain system, a larger degree of out-of-plane

contributions are necessary. In order to account for this interference in the current work and improve its spatial resolution, a maximum entropy deconvolution algorithm was used to process the three-dimensional images. The algorithm discussed here has been adopted from Cornwell and Evans (1985), whose work was limited to reconstruction of two-dimensional images. It has been extended to three dimensions for this work, and the notation has been changed to accommodate the three-dimensional approach. A measured set of images, **I**, results from the convolution of the true 3-dimensional object **O** with the imaging system's spatially dependent point spread function, **P**, and noise, **N**, as

$$\mathbf{I} = \mathbf{O} * \mathbf{P} + \mathbf{N} \tag{3.1}$$

where * is the convolution operation. The goal of the MEM algorithm is to determine **O** through iteration. At each step, a reconstructed object from the current guess for **O** is represented by

$$\mathbf{B} = \left(B_{ijk} \middle| i = 1, X; j = 1, Y; k = 1, Z\right) \tag{3.2}$$

where each of Z image planes are X by Y pixels. The original algorithm (Cornwell and Evans, 1985) was only applied to 2-D images, i.e. $Z = 1$, thus the dimensionality of **B** has been extended in the current work for three-dimensional applications.

Cornwell and Evans (1985) defined relative entropy in the object as

$$H(\mathbf{B}|\mathbf{I}) = -\Sigma_i \Sigma_j \Sigma_k B_{ijk} \ln\left(\frac{B_{ijk}}{I_{jk}}\right) \tag{3.3}$$

and use this entropy to constrain the computed object; however, following the derivation of Shore and Johnson (1980), an alternate definition has been used:

$$H(\mathbf{B}|\mathbf{I}) = -\Sigma_i \Sigma_j \Sigma_k B_{ijk} \ln\left(B_{ijk}\right) \tag{3.4}$$

This definition leads to more stable solutions and is used more frequently in similar applications. The reconstruction **B** represents the object, and thus a corresponding image reconstruction can be produced by

$$\mathbf{I}' = \mathbf{B} * \mathbf{P} \tag{3.5}$$

For the reconstruction to be valid, $\mathbf{I}'$ should resemble **I** as closely as possible. To achieve this, Cornwell and Evans compute the least squares error over the image set and use this as one constraint on the converged solution

$$\chi^2 = \Sigma_i \Sigma_j \Sigma_k \left(I_{ijk} - I'_{ijk}\right)^2 \tag{3.6}$$

The final constraint to be considered is conservation of energy, as

$$\Sigma_i \Sigma_j \Sigma_k B_{ijk} = \Sigma_i \Sigma_j \Sigma_k I_{ijk} = F \tag{3.7}$$

From this, the objective function for the fit can be expressed as

$$J = H - \alpha \cdot \chi^2 - \beta \cdot F \tag{3.8}$$

where α and β are constant Lagrange multipliers for the total least squares error and the image set intensity. The algorithm iterates on **B** to minimize J. Cornwell and Evans found that a second order Newton-Raphson method was effective in diminishing extreme gradients of J resulting from the drastic change in the relative entropy near zero brightness. Thus, the increment to the next reconstruction is given by

$$\Delta\mathbf{B} = (-\nabla\nabla J)^{-1} \cdot \nabla J \tag{3.9}$$

where

$$\nabla J = \nabla H - \alpha \nabla \chi^2 - \beta \mathbf{1} \tag{3.10}$$

$$(-\nabla \nabla J)^{-1}_{ijk} \sim \frac{1}{\frac{1}{B_{ijk}} + 2\alpha}, i = j \tag{3.11}$$

and

$$(-\nabla \nabla J)^{-1}_{ijk} \sim 0, i \neq j \tag{3.12}$$

Further explanation of how these terms have been derived and simplified is described by Cornell and Evans (1985). The previous work was applied to 2-D images and 2-D image reconstruction. In the present paper, we extend this algorithm to a set of *Z* layered images by recognizing that each m^{th} focal depth within the object has an effect on all n focused images. For each m^{th} location in the object and n^{th} image, there is a corresponding point spread function P_{mn}, such that the n^{th} resulting image layer is given by

$$\mathbf{I}_n = \Sigma_m (\mathbf{P}_{mn} \cdot \mathbf{O}_m) + \mathbf{N} \tag{3.13}$$

Other changes made in our formulation were minor and consisted primarily of different methods for determining the Lagrange multipliers, α and β. In this work, α is kept constant throughout the calculations and β is changed at each iteration by using the assumption that the overall pixel count must stay constant, such that

$$\Sigma_i \Sigma_j \Sigma_k \Delta \mathbf{B}_{ijk} = 0 \tag{3.14}$$

Additionally, one can see from Eqn. (3.11) that a negative or zero pixel value will induce a division by zero. Therefore, at each iteration, nonpositive values were replaced by small positive

values, relative to total pixel counts. The reconstruction's total power was then renormalized after these replacements.

The main limitation on this algorithm is computational: for every iteration, each layer of the reconstruction must be convoluted with its corresponding PSF for the given image plane, for a total of N^2 FFT's and N^2 IFFT's, where $N$is the number of images. Additionally, the Fourier transforms scale with the number of pixels in each image. However, one strength of this particular algorithm is its fast convergence. Each image set included in this work converged in fewer than 15 iterations with <1% error per pixel.

3.6 Results and Discussion

A sample set of images from the 10 mm flame separation case is shown in Fig. 3.8. Their colors have been inverted for easier viewing, such that the flame fronts are dark. They are ordered from (a) to (p), with (a) being the side of the flame field close to the imaging system, and (p) being the far side of the flame field. Figure 3.9 shows the approximate locations of the various images. A flame front can be seen in many of the images, where line-of-sight integration is least significant due to the system's narrow depth of field, as in images (e) and (k). The approximate geometry of the flames can be discerned, and it is apparent that there are two flames, though the boundary between the two is somewhat unclear; in images (i) – (j), the flame fronts are indiscernible. On the near side of the flame, the flame fronts are noticeably less clear, such so that they cannot be reasonably seen in images (a) – (c) due to out-of-plane interference. These images represent an

improvement over traditional chemiluminescence imaging due to the Cassegrain system depth of field but line-of-sight interference is still limiting.

Figure 3.10 shows the reconstructed object, **B**, ordered in the same fashion. It is easy to see that the flame fronts are more well-defined throughout the depth of the image, due to a reduction in background interference from out-of-plane contributions. This improvement comes from the correct modeling of each object plane's contribution to each imaging plane such that the resulting converged object is resolved. In this reconstructed object, the transition between the flames is now much clearer; flame fronts are now visible in images (i) and (j). The near images show mild improvement, and flame fronts are now visible in images (a) - (c). The far field images (m) – (p) show drastic improvement over the original images, and with signal noticeably decreased outside of the flame fronts. The projection of these images, $\mathbf{I}'$, matches the original images, **I**, with an average error of 0.3% per pixel, and the reconstructions are consistent with the expected images based on the known flame structure.

To further test the spatial resolution abilities of this imaging technique, the sets of reconstructed objects for each configuration were used to create top-down views of the flame structure, as shown in Fig. 3.11. These views were created by assuming that the flame fronts were approximately vertical in the region of interrogation. The pixel values were averaged in the y-direction, in order to extract the flame profile in the x-direction. The flame front location was determined by the maximum second derivative of this profile. In each case, it is obvious that there are two flames rather than one, which is a clear improvement over traditional large depth-of-field chemiluminescence imaging, such as in Fig. 3.5(b), where there appears to only be a single flame. Additionally, the boundary between the two is sharp – not only do the flames not overlap, but there is a clear space between them in cases (e) and (f), the 11 and 12 mm

separations. The relative locations of the flames in each case are properly represented in the top-down images. In the smaller flame separations, such as Fig. 3.11(a), with a separation of 8 mm, the flames do not overlap, suggesting that this system can resolve structures in the depth of field less than 1 mm. Note that although the flames examined here were symmetric, no symmetry was assumed in the analysis to determine flame contours. Non-symmetric flames would not complicate the analysis of out-of-plane contributions.

In its present form the system is sufficient for resolving out of plane contributions of ~1 mm for application where average 3-D structure is sufficient. In order to be adapted to imaging of a turbulent flame field, several alterations need to be considered. First, one of the mirrors would need to be either placed on a high-speed translation stage (High-Performance Long-Travel Linear Motor Stages IMS-LM Series, 2015) or replaced with a deformable mirror, such as the kind described by Freeman and Garcia (1982). The fastest translation stages available are capable of speeds of up to 1000 mm/s (High-Performance Long-Travel Linear Motor Stages IMS-LM Series, 2015). Assuming a flame field 1 cm deep, this stage could transverse the entire flame field in approximately 10 ms, which is too slow for some time scales of interest. Deformable mirrors (MEMS-Based Deformable Mirrors, 2015) are currently capable of a mechanical response time of <20 μs, which could be sufficient for studying some turbulent phenomena. However, caution should be taken with this approach, as changing the curvature of the convex mirror can induce spherical aberration. Both of these options also come at a cost, although they would still be significantly less expensive than a three-dimensional laser system or similar. Nevertheless, the current system is sufficient when time-averaged results are useful.

3.8 Tables

Table 3.1: Pertinent dimensions of optical system for data collection.

Dimension	**Description**	**Value [mm]**
z_1	Distance from object to concave mirror	416.9
z_2	Distance from object to convex mirror	93.9 mm
z_3	Distance from object to camera	218.9 mm
R_1	Radius of concave mirror	304.9 mm
R_2	Radius of convex mirror	100 mm

3.9 Figures

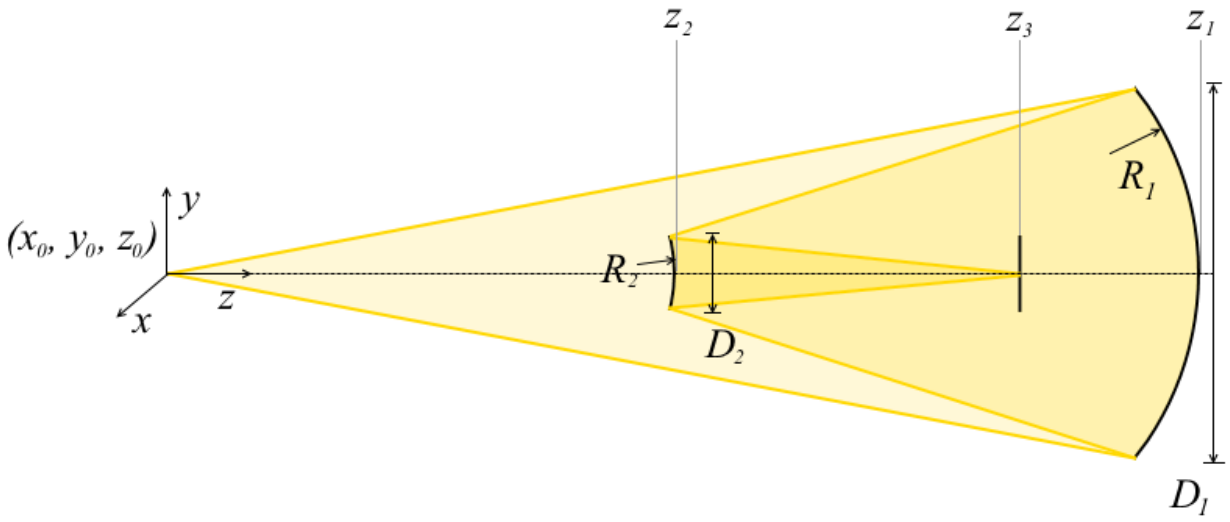

Figure 3.1: Simplified Cassegrain system with pertinent dimensions labeled.

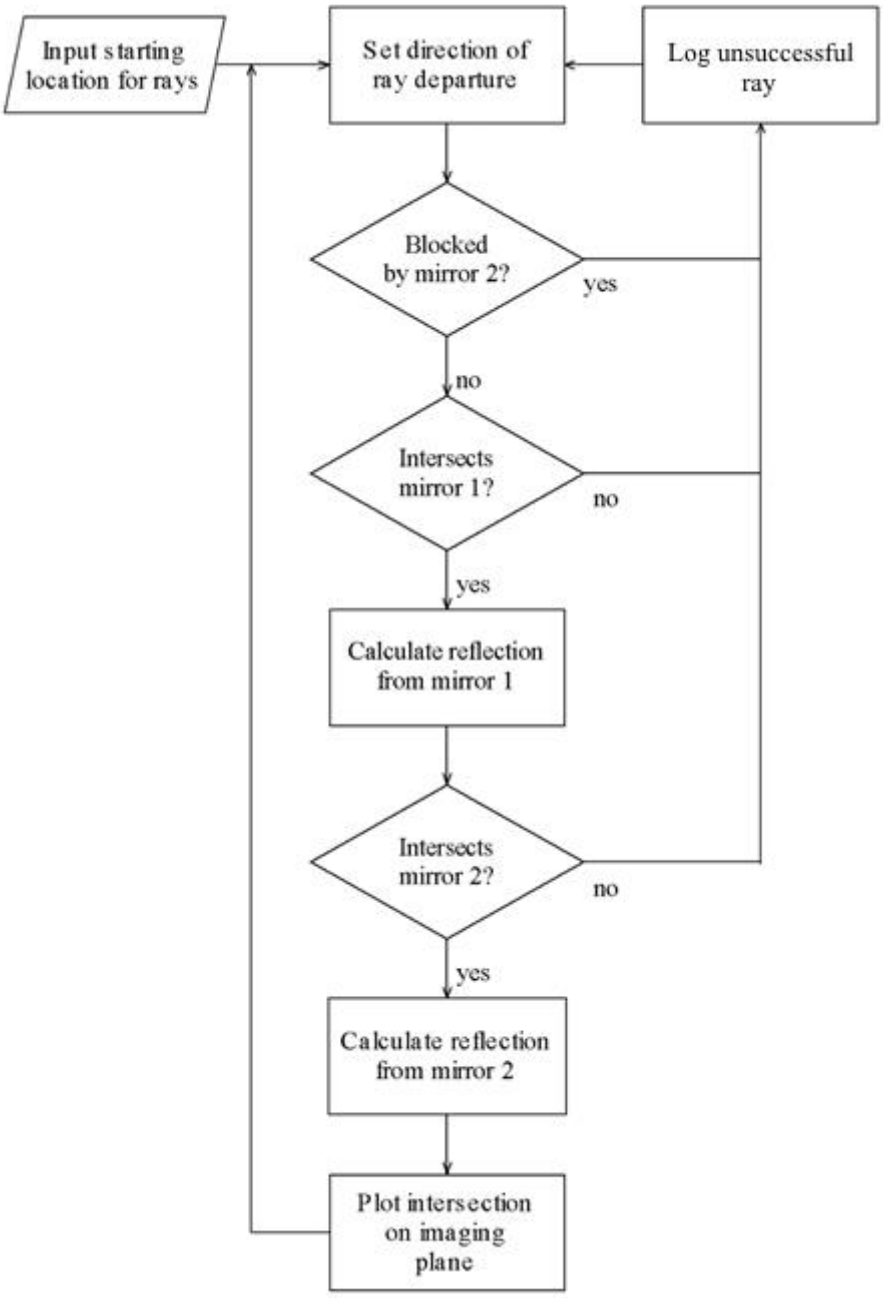

Figure 3.2: Flow chart of ray-tracing algorithm.

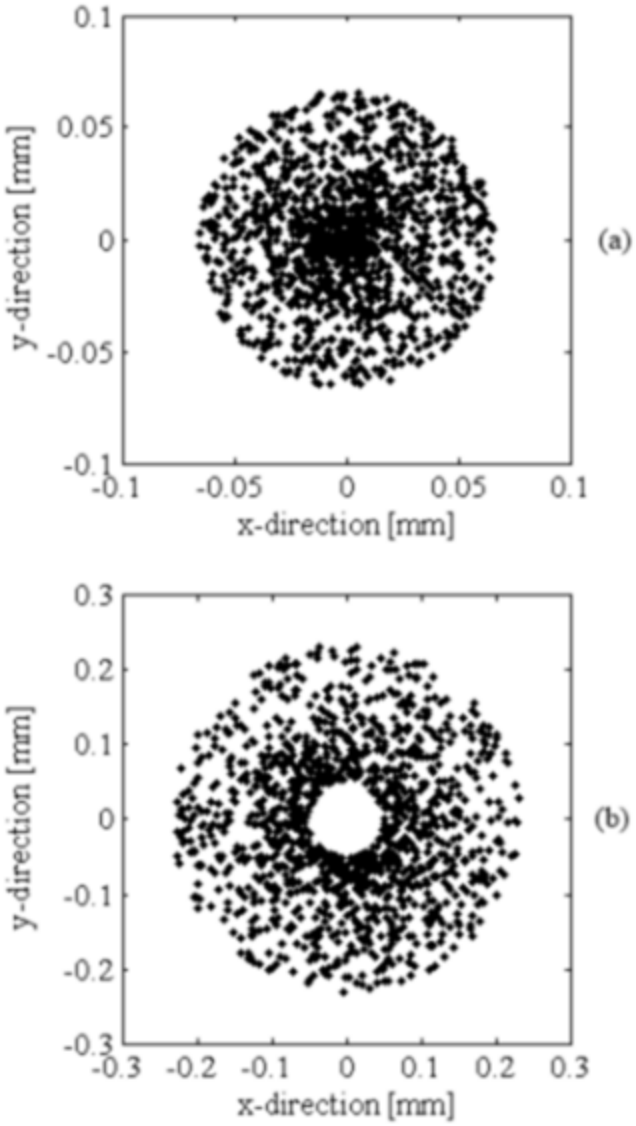

Figure 3.3: Ray-tracing results for a point source at two locations: (a) in focus, and (b) 1 mm out of focus. Note that the two plots have different scales.

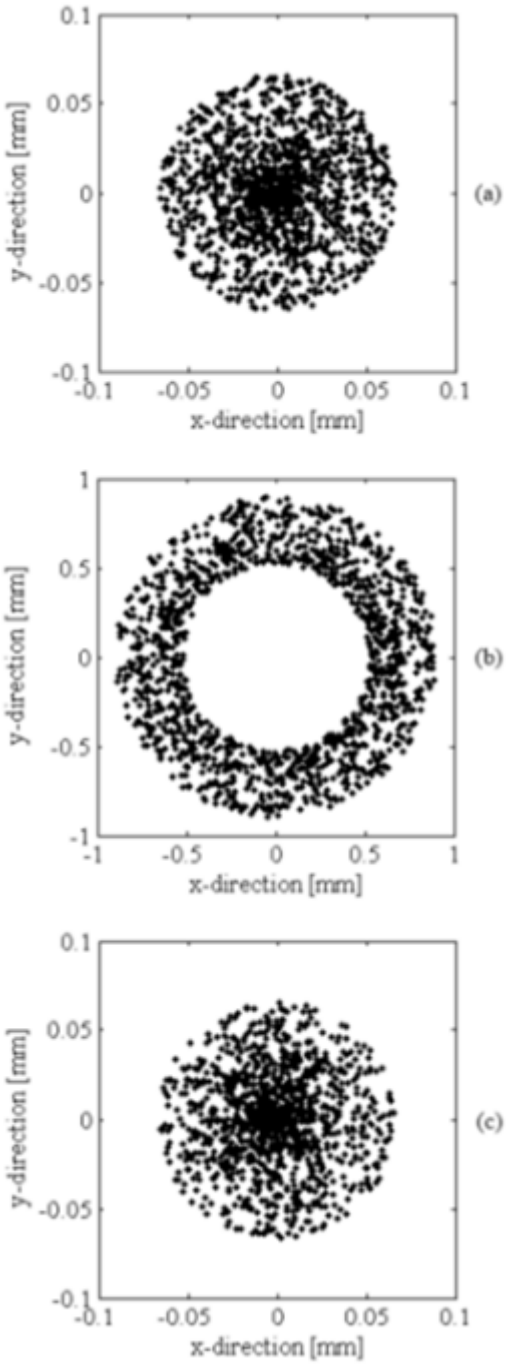

Figure 3.4: Ray-tracing results for a point source at three configurations: (a) in focus, object and concave mirror at original locations, (b) concave mirror moved 1 mm out of focus, and (c) mirror in same location as (b) but object moved 4 mm to refocus.

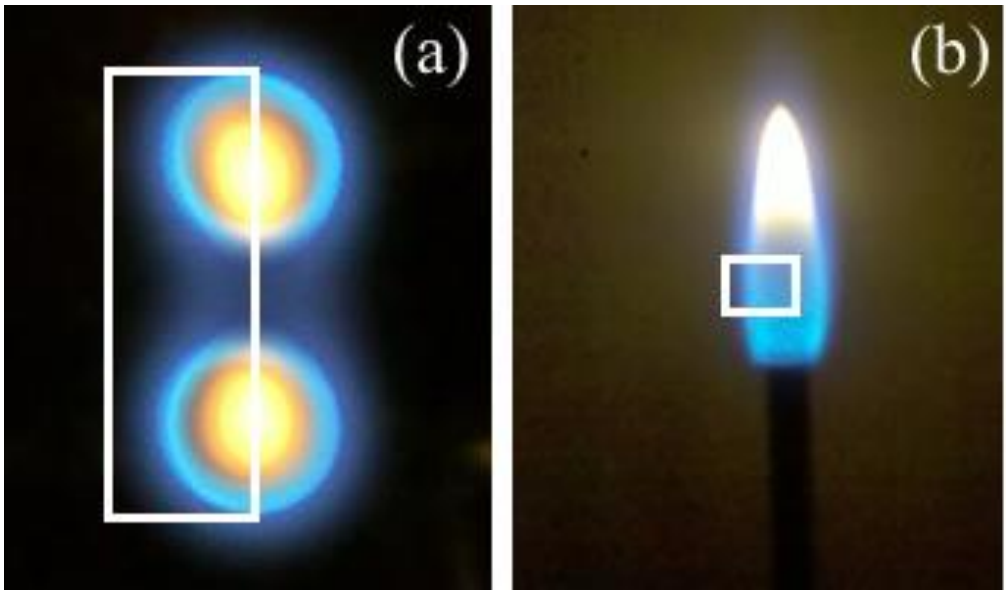

Figure 3.5: Dual flames with 9 mm separation, as viewed from top (a) and perspective of imaging system (b). Approximate region of interrogation is defined by the box.

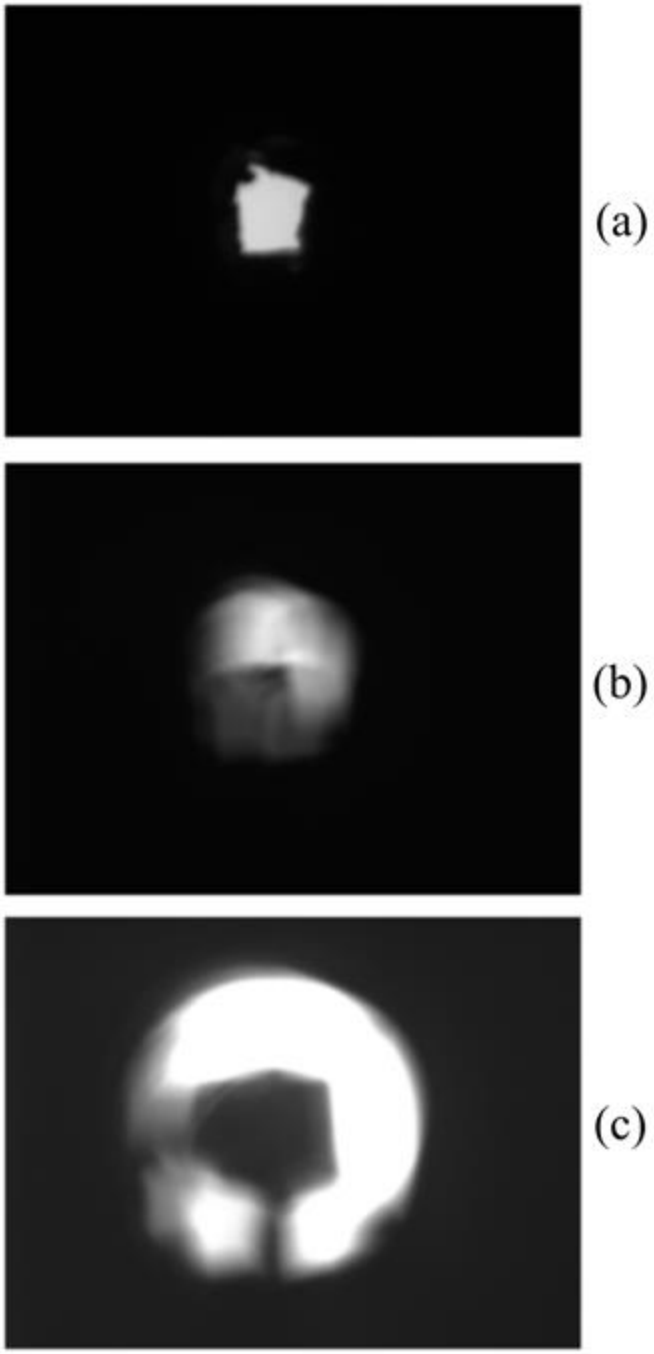

Figure 3.6: Image created from a backlit target placed at three locations: (a) in focus, (b) 1 mm out of focus, (c) 2 mm out of focus.

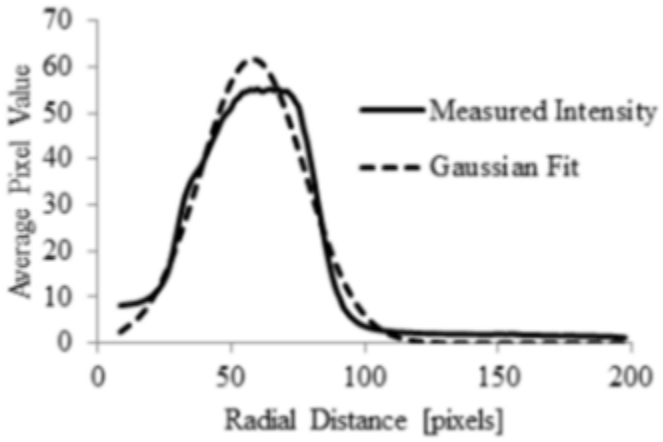

Figure 3.7: Pixel counts, averaged radially from the center, for the focused image from Fig. 5a. The measured pixel counts are overlaid with a corresponding Gaussian fit (R^2=0.974).

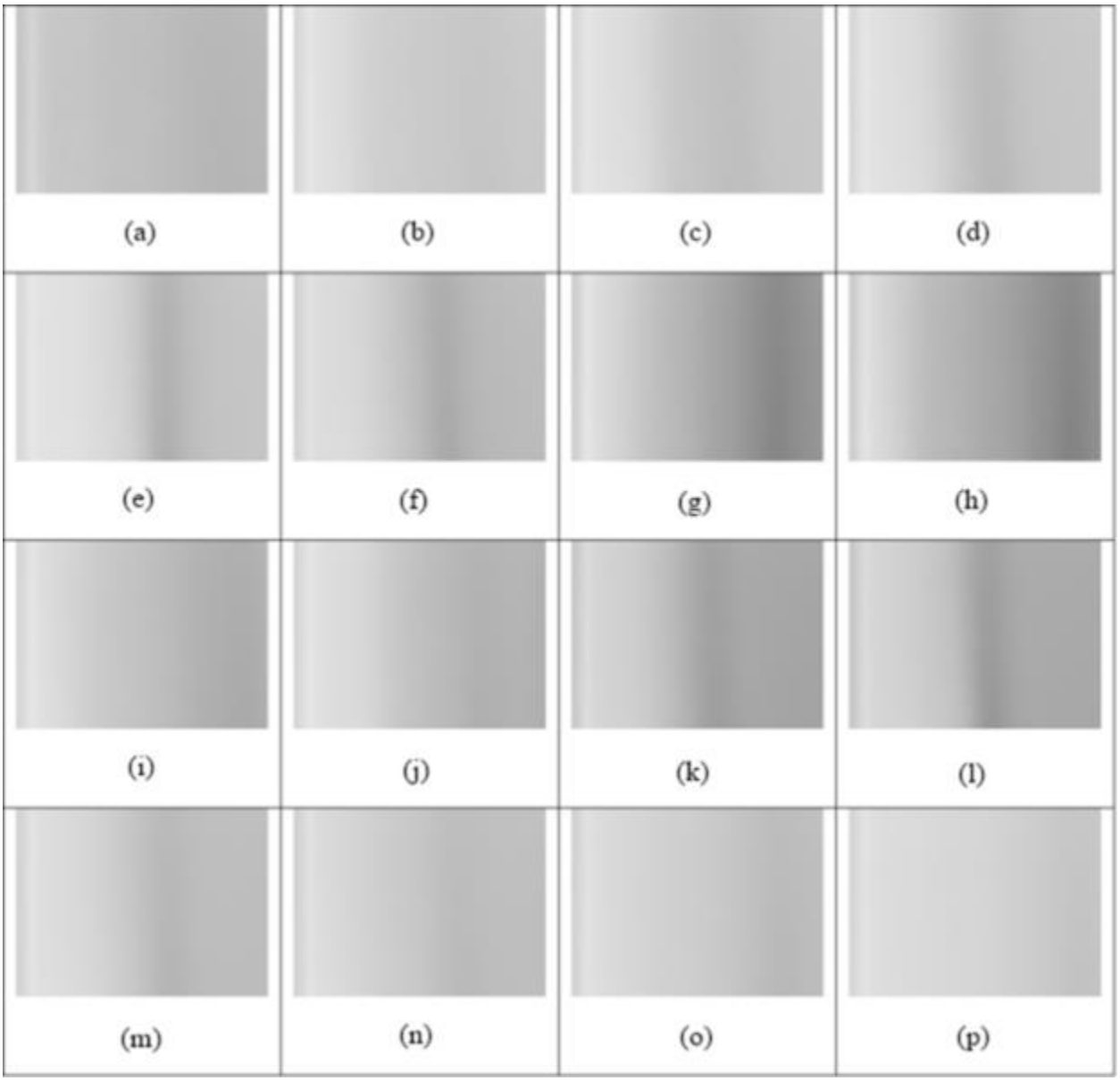

Figure 3.8: Images of dual-flame structure at 10 mm separation, taken with Cassegrain system. Images are ordered from the near side to the far side of the flame. Intensities have been inverted for easier viewing (dark = higher pixel count).

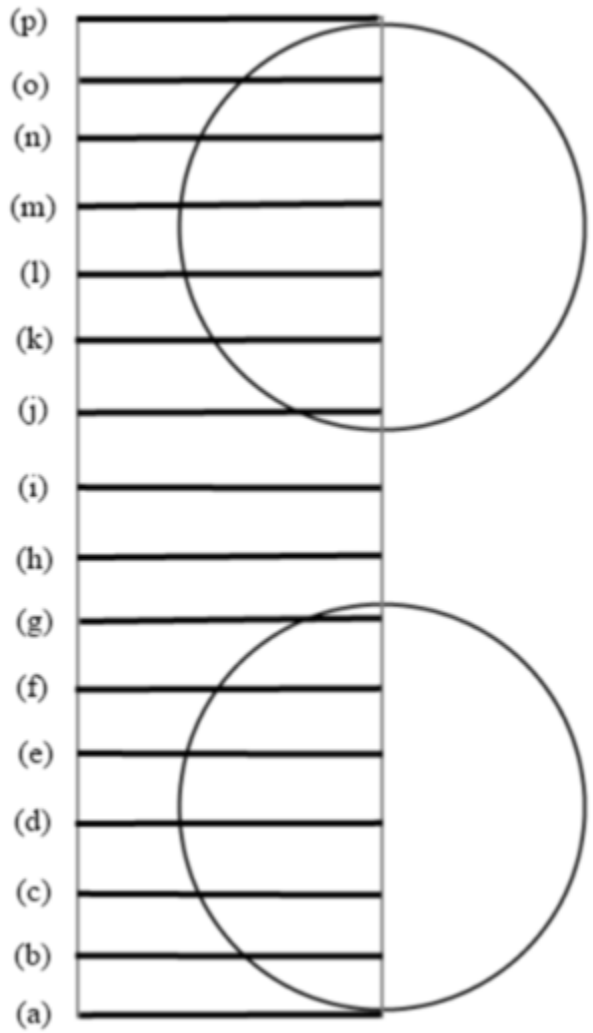

Figure 3.9: Approximate image locations with respect to flames with 10 mm separation.

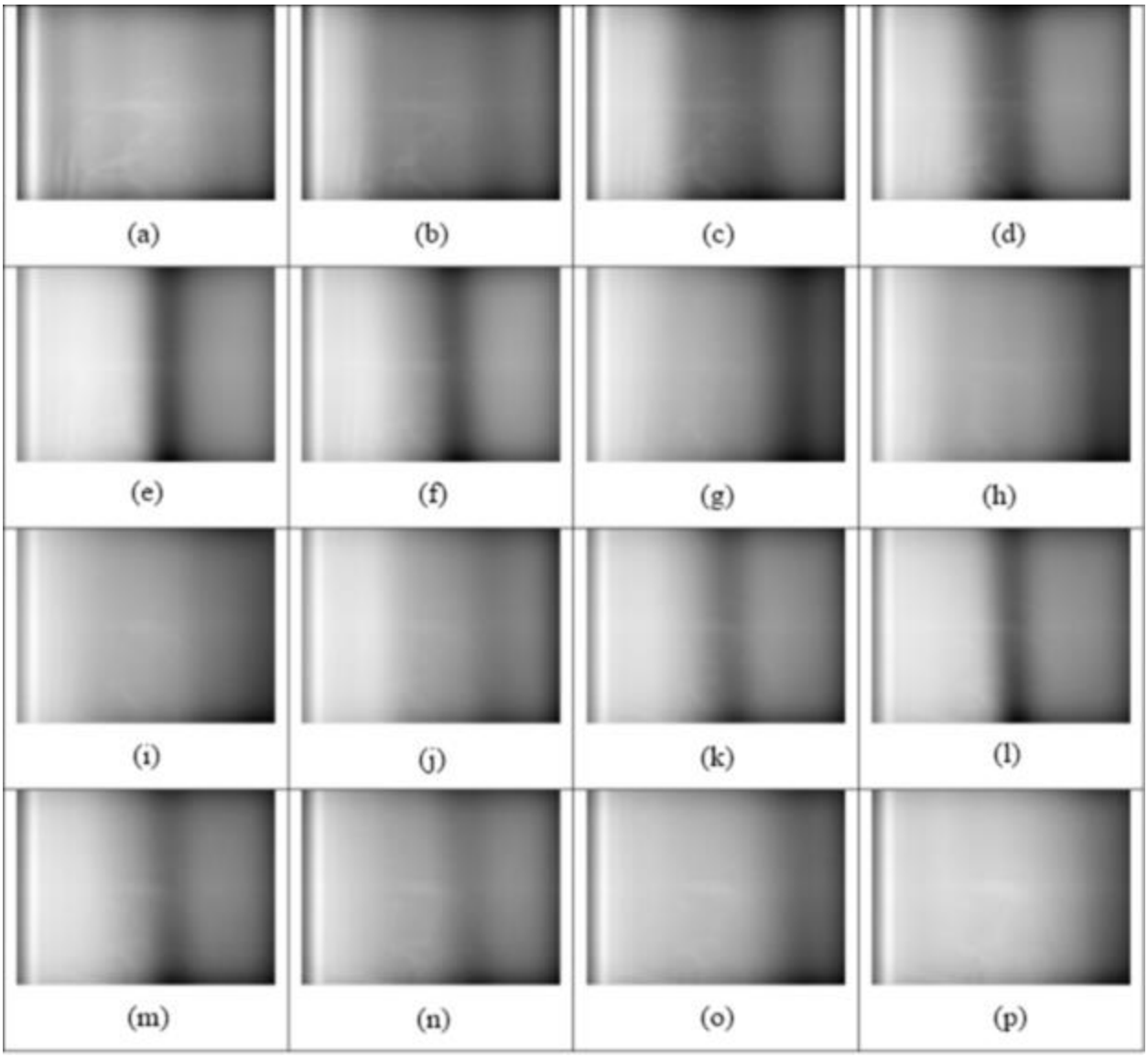

Figure 3.10: Images of dual-flame structure at 10 mm separation, after MEM processing. Images are ordered from the near side to the far side of the flame. Colors have been inverted for easier viewing (dark = higher pixel count).

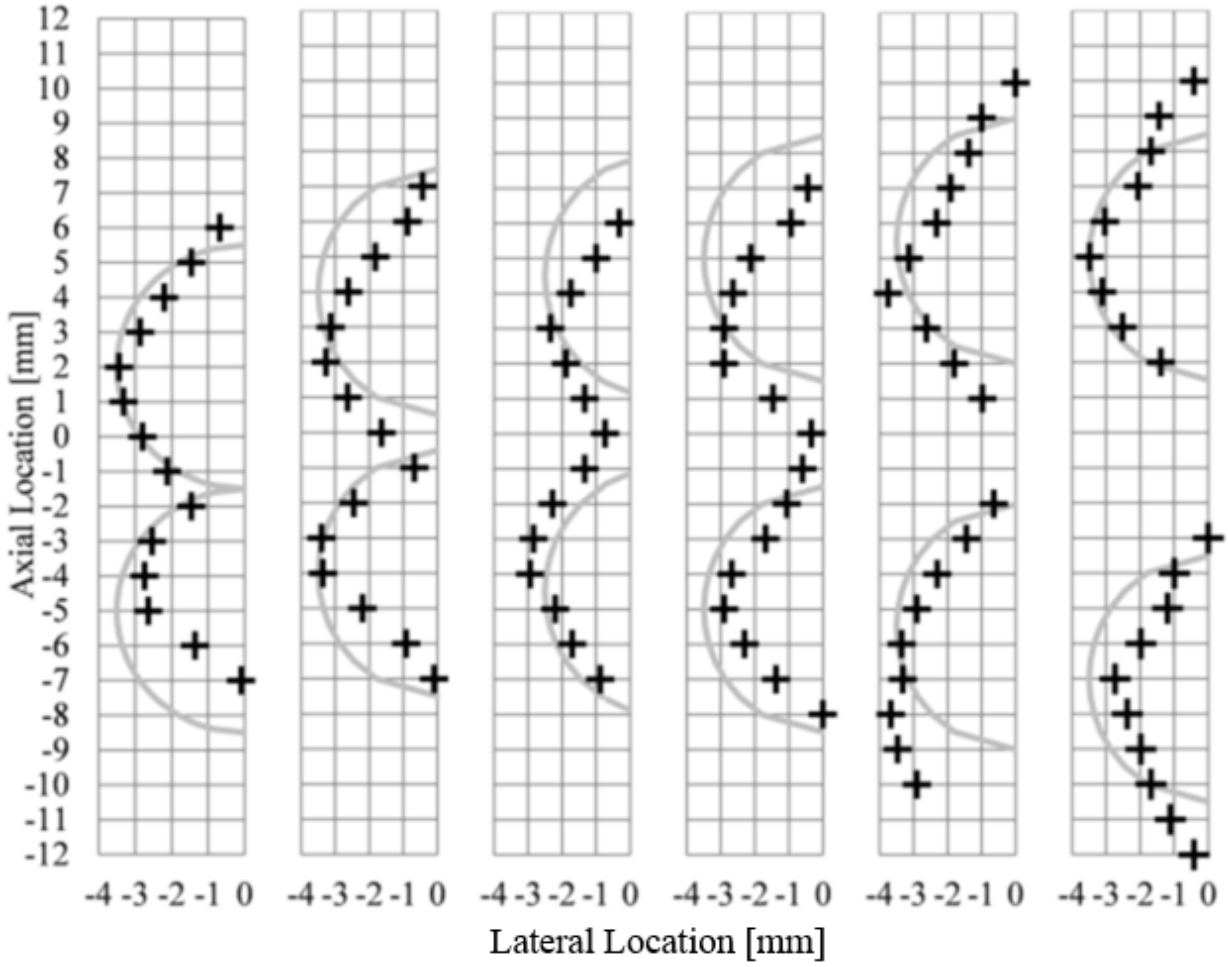

Figure 3.11: Location of flame fronts determined from MEM processed images. Flame separation from left to right: 7, 8, 9, 10, 11, and 12 mm. +'s represent the location of the flame front. The gray lines represent the nominal flame front locations.

4. Measurement of Time-Series Statistics in an Axisymmetric, Turbulent Jet

4.1 Background and Motivation

Temporal statistics such as the power spectral density (PSD) and autocorrelation function (ACF) from turbulent time series are of interest to improve numerical models, particularly various Large Eddy Simulation (LES) sub-models (Renfro *et al.*, 2004, Ihme and Pitsch, 2008). However, recovering such statistics accurately requires measurements with a high degree of temporal resolution, as well as spatial resolution. This generally calls for the use of high repetition rate laser systems, such as in the work of Renfro *et al.* (2000c, 2000b) or Wang *et al.* (2008), which used laser-induced fluorescence (LIF) to recover local time series of scalars and Rayleigh scattering for temperature in a series of canonical flames. These statistics collapsed when normalized properly, which indicates that the spatially dependent integral time scale may be used as a single time scale to characterize fluctuations in a given burner. These results are illuminating, but they require expensive equipment, expert users, and optical access in multiple directions. Some attempts have been made to extract temporal statistics from chemiluminescence images, such as the work of Giacomazzi *et al.* (2008), who calculated PSD's from line-integrated photodiode measurements of chemiluminescence in a turbulent jet flame and found that they compared well to expected trends of temperature and turbulent kinetic energy, indicating that chemiluminescence may be a useful natural marker for turbulence-chemistry interactions. However, these results were line-integrated, which limits their application to model improvement since the time scales vary with position. Previously, attempts have been made to apply an Abel inversion to line-integrated temporal statistics in a non-reacting jet (Mayrhofer and

Woisetschläger, 2001). The local, spatially-resolved statistics compared well with locally measured values, indicating that this method may be useful in recovering temporal statistics from axisymmetric flames.

4.2 Specific Objectives

In this work, line-integrated chemiluminescence measurements were made with a high-speed camera. Temporal statistics such as PSD's, ACF's, and integral time scales were calculated, and an Abel inversion was applied to the PSD's in an attempt to recover local integral time scales. These results were compared to previous measurements of CH LIF (Renfro *et al.*, 2000c) in the same burner in order to assess the following

1. The usefulness of chemiluminescence as an inexpensive, simple alternative to CH LIF for estimating turbulent time scales.
2. The effect of line integration on various temporal statistics.
3. The accuracy of temporal statistics obtained by applying an Abel inversion to measured, line-integrated statistics.

4.3 Experimental Setup

A burner with a diameter of 3.4 mm issued a mixture of 22.1% CH_4, 33.2% H_2, and 44.7% N_2 at a range of turbulent flow rates, listed in Table 4.1 and designated flames A1-A5. In addition to average exit velocity, $\bar{V}$, the cold flow Reynolds number is listed. This is defined as

$$Re = \frac{\bar{V}D}{\nu} \tag{4.1}$$

where D is the pipe diameter and ν is the molecular viscosity. These flames are based on the TNF workshop $CH_4/H_2/N_2$ flames (Bergmann *et al.*, 1998) listed in Table 2.1 with a smaller jet diameter to stay below a heat release rate of 18.5 kW limited by a previous experimental setup (Renfro, 2000). They are identical to the A1-A5 flames in the work of Renfro *et al.* (2000b, 2000c) for comparison to previous CH high-speed LIF results. These previous results were collected using an ultra-fast, high repetition-rate Ti:Sapphire laser system, allowing for a spatial resolution of 140x140x250 μm^3. A photon-counting technique was used to obtain sampling rates ranging from 10 kHz to 40 kHz. Averaged profile measurements were also collected by averaging over 3 seconds at a sampling rate of 10 Hz (Renfro *et al.*, 2000c).

In the current work, high speed videos were collected using a Photron Fastcam SA5 at a variety of sampling rates, listed in Table 4.1. All images were binned 2x2 on-chip, and a 50 mm lens was used with a +4 macro filter, allowing for nominal pixel resolution of approximately 130 μm/binned pixel. Each video captured an area from the jet exit to a downstream location greater than $x/D = 10$, allowing for data analysis at $x/D = 1$, 2, 5, and 10, for comparison to previous work (Renfro *et al.*, 2000c). Forty videos of 4096 frames each were collected of each flame to reduce noise by averaging temporal statistics. Sampling rates were chosen to maximize the

signal-to-noise ratio while still guaranteeing that the power spectra captured the noise floor for accurate noise subtraction, as described subsequently. Additional videos were taken at lower sampling rates, also listed in Table 4.1, in order to obtain average chemiluminescence profiles.

4.4 Time Series Analysis and Noise Considerations

The various temporal statistics were calculated via the method outlined by Renfro (2000). First, the power spectral density with respect to frequency is calculated from the fast Fourier transform (FFT) of each mean-subtracted time series, $C(t)$. For this work, the power spectral density has been normalized by the sampling rate, S, the number of samples, N, and the variance, σ^2. Normalizing by the signal variance allows for comparison among time series in various flames and axial locations.

$$PSD(f) = \frac{1}{N \cdot S} \frac{\left|\mathcal{F}\left(C(t)\right)\right|^2}{\sigma^2} \tag{4.2}$$

For each flame and axial location, the PSD's are averaged over 40 videos in order to obtain clean statistics. PSD's resulting from a single video as compared to 40 videos can be seen in Fig. 4.1(a), which is calculated from the A3 flame at x/D = 10. The next step is to subtract noise, which affects the shape of the PSD as well as the ACF and the integral time scale. Gaskey *et al.* (1990) showed that in a LIF experiment the measured (total) time series is a linear combination of the PSD's of contributions from concentration fluctuations and from shot noise, weighted by their respective standard deviations.

$$\sigma_{total}^2 PSD_{total} = \sigma_S^2 PSD_S + \sigma_N^2 PSD_N \tag{4.3}$$

PSD_S and PSD_N are the PSD's of true signal and noise, respectively. This same assumption will be used for chemiluminescence measurements. The relative standard deviations of each of these time series are also related by

$$\sigma_{total}^2 = \sigma_S^2 + \sigma_N^2 \tag{4.4}$$

The equation used by Gaskey *et al.* (1990) is slightly different due to their inclusion of a DC component, which is zero in this case because only the fluctuating component is considered (Renfro, 2000).

Shot noise is assumed to be uncorrelated and is spread evenly over all frequencies. For proper normalization

$$PSD_N = \frac{1}{f_c} \tag{4.5}$$

where f_c is the cutoff frequency of the PSD measurement, equal to half the sampling rate. Given that turbulent spectra decay at high frequencies, we can assume that at sufficiently high frequencies, the PSD of true signal will be small as compared to that of shot noise. This effect can be seen in a flat region at high frequencies in Fig. 4.1(a). In this flat region, it can be assumed that

$$\sigma_N^2 PSD_N \approx \sigma_{total}^2 PSD_{total} \tag{4.6}$$

Combining Eqns. (4.5) and (4.6) gives

$$PSD_{total} = \left(\frac{\sigma_N}{\sigma_{total}}\right)^2 \frac{1}{f_c} \tag{4.7}$$

By averaging over high frequencies (the top 250 frequencies), σ_N can be calculated directly, and the noise floor can be subtracted from PSD_{total}. The rms of true signal, σ_S, can then be

calculated via Eqn. (4.4), and PSD_S can be re-normalized by rearranging Eqn. (4.3). The noise-subtracted, re-normalized PSD is shown in Fig. 4.1(b) as compared to the same PSD without noise subtraction. The effect of noise subtraction can be seen mainly in the inertial subrange, where the log-log slope nearly doubles, from approximately -1.77 to -3.52.

Noise subtraction allows for measurements to be compared among systems with different noise characteristics, such as in the work of Renfro (2000), in which measurements taken using a lock-in amplifier were compared to those from a photon-counting technique. After noise subtraction, the measurements were virtually identical, despite having been taken a year apart, which indicates that the temporal statistics from this work can be meaningfully compared to those of other measurement systems.

In addition to PSD's, ACF's and integral time scales have been calculated. Autocorrelation functions were calculated by taking the inverse fast Fourier transform (IFFT) of each PSD. From this, the integral time scale was calculated in two different ways. One approach, used by Renfro (2000) and others, is to numerically integrate the autocorrelation function from $\Delta t = 0$ until the first negative ACF value. This can produce uncertainty because noise causes the function to cross the x-axis at an arbitrary point. The other approach takes advantage of the fact that exponential decays have previously been shown to be a useful approximation for time series in these and other turbulent flames (Renfro *et al.*, 2000b, Renfro *et al.*, 2000c), and an exponential fit was performed from $\Delta t = 0$ to $\rho(\Delta t) = 1/e$.

The previously described noise correction also affects the calculated autocorrelation functions, as shown in Fig. 4.1(d), which shows an ACF calculated at x/D = 10 in the A3 flame both before and after noise subtraction. Uncorrelated noise causes a lower ACF at small Δt, which reduces

the integral time scale considerably. Correcting for shot noise remedies this, as seen in Fig. 4.1(d) and described by Renfro (Renfro, 2000). Although the difference may appear small in this case, neglecting to subtract noise results in an integral time scale – calculated by numerically integrating to the first x-axis cross – that is approximately 20% smaller than when noise is subtracted.

4.5 Abel Inversion

Although turbulent flames are instantaneously non-axisymmetric, as shown schematically in Fig. 4.2, their time-averaged profiles are axisymmetric, as are their temporal statistics such as integral time scales. Therefore, it stands to reason that if one collects time-averaged, line-integrated profiles, it should be possible to extract the mean local profile via an Abel inversion. However, the approach for temporal statistics is slightly more complex.

In order to understand this, let us consider a simplified system. Given two time series, $c_A = c_A(t)$ and $c_B = c_B(t)$, let us assume that c_A and c_B cannot be measured directly, but that their sum, $c_A + c_B$, can be. Linearity dictates that the Fourier transform of their sum is as follows

$$\mathcal{F}(c_A + c_B) = \mathcal{F}(c_A) + \mathcal{F}(c_B) = C_A(f) + C_B(f) \tag{4.8}$$

In order to calculate the power spectral density, F_{A+B}, of $\mathrm{c_A} + \mathrm{c_B}$, one must multiply by the complex conjugate

$$F_{A+B} = (C_A + C_B)(C_A + C_B)^* = C_A C_A^* + C_B C_B^* + C_A C_B^* + C_B C_A^* \tag{4.9}$$

Taking the inverse Fourier transform of this and normalizing properly gives the autocorrelation function of $c_A + c_B$. Due to linearity of the inverse Fourier transform, this can be expressed as a

sum of the autocorrelation functions of c_A and c_B, as well as the cross-correlation functions of c_A with c_B, and vice versa.

$$\rho_{A+B} = \rho_{AA} + \rho_{BB} + \rho_{AB} + \rho_{BA} \tag{4.10}$$

If only $c_A + c_B$ is directly measurable, it is impossible to recover temporal information about c_A or c_B independently without additional information.

However, let us assume there is another time series $c_A'$with identical or nearly identical frequency content to c_A – that is, their integral time scales are equal. If c_A' is directly measurable, then its temporal information can be used to estimate information about c_B. For example, in Fig. 2.3, c_a' would refer to the time series measured in pixel N, while $c_A + c_B$ is measured at pixel $N - 1$. Although it is tempting to simply subtract c_A' from $c_A + c_B$, this leads to errors due to phase mismatch, as well as the presence of noise, which amplifies when inverted directly. Noise is present in the frequency domain as a constant magnitude spread evenly over all frequencies, which is easier to account for. Instead, one possible approach is to assume that $\mathcal{F}(c_A) \approx \mathcal{F}(c_A')$. Returning to our axisymmetric system and recalling Eqn. (2.15) for an Abel inversion, this means that the Fourier transform of the spatially-resolved time series, $c(r,t)$ can theoretically recovered from the line-integrated time series $c(y,t)$ via

$$\mathcal{F}\big(c(r,t)\big) = -\frac{1}{\pi}\int_r^\infty \frac{\mathcal{F}\big(c(y,t)\big)dy}{\sqrt{y^2 - r^2}} \tag{4.11}$$

This inversion must be computed numerically, as described in Section 2.2. However, it is important to note that applying a Fourier transform to a time series produces a complex array, which includes phase information as well as magnitude. This can be expressed for a given time series $c_A(t)$ as

$$\mathcal{F}\big(c(t)\big) = A(f)e^{\phi_A(f)} \tag{4.12}$$

where, the magnitude is given by $A = |C_A| = \sqrt{\mathrm{Re}\big(C_A(f)\big)^2 + \mathrm{Im}\big(C_A(f)\big)^2}$ and the phase is given by $\phi_A(f) = \tan^{-1}\frac{\mathrm{Im}(c_A)}{\mathrm{Re}(c_A)}$. Referring to Eqn. (4.8), this means that the Fourier transform of $c_A + c_B$ contains the combined phase information of both c_A and c_B. Since the phases of c_A' are different from those of c_A due to being measured in different locations, attempting to extract c_B via $\mathcal{F}(c_A + c_B) - \mathcal{F}(c_A')$ may produce errors due to phase mismatch. Another approach, recommended by Mayrhofer and Woisetschläger (2001), is to perform an Abel inversion on the magnitude only. That is, the magnitude of the Fourier transform of the spatially-resolved time series, $c(r,t)$ can theoretically recovered from the line-integrated time series $c(y,t)$ via

$$\big|\mathcal{F}\big(c(r,t)\big)\big| = -\frac{1}{\pi}\int_r^\infty \frac{\big|\mathcal{F}\big(c(y,t)\big)\big|dy}{\sqrt{y^2 - r^2}} \tag{4.13}$$

However, Eqn. (4.13) assumes that taking the magnitude of the Fourier transform conserves linearity, which it does not. The magnitude, which can also be expressed as the square root of Eqn. (4.9), contains terms based on the cross-correlation of c_A and c_B. Eqn. (4.13) assumes that there is no cross-correlation between c_A and c_B; in cases where the correlation between the two time series is small or minimal, this method should be accurate. When the two time series are strongly correlated, then inverting the magnitude will be less accurate. The approaches given in Eqns. (4.11) and (4.13) will each be applied to the line-integrated time series in order to assess their relative success in the given flames.

Additionally, the various approaches to the Abel inversion must be evaluated. According to Pretzler *et al.* (1992), the Fourier method of Abel inversion is the most successful method, as it minimizes reconstruction error due to noise at all radial locations simultaneously. Unfortunately,

the Fourier method is also computationally expensive. The area method, on the other hand, magnifies error at small radii, but it is mathematically simple. In order to compare these two methods in the current application, they have been applied to average flame profiles taken at lower frame rates listed in Table 4.1. The location of the peak signal normalized by x location (r/x) and the full width half maximum (FWHM) of the signal profile after Abel inversion by each method were compared to previous LIF results (Renfro *et al.*, 2000c). In addition, the relative success of these methods was assessed by assuming that the spatially-resolved profile has an approximately Gaussian shape, as was the case in previous LIF work. This profile was treated with a forward discrete Abel transform, as in Eqn. (2.16), and its peak location and FWHM were determined via a least squares fit. This approach will retain minimal noise in the reconstruction. It cannot be used for later inversions of time series spectra, but was used as a baseline for a comparison of the various Abel inversion methods.

The results of these inversions may be found in Tables 4.2 and 4.3, which show the original and various reconstructed values of peak location r/x and profile FWHM. Perhaps the most interesting result of these Abel inversions is that there is virtually no difference among the three inversion methods. One set of reconstructed profiles is shown in Fig. 4.3 and compared to a nominal profile based on the previous LIF results. Interestingly, error from both Abel inversion methods increases at small radial locations; this is expected for the area method, but not the Fourier method. This occurs largely because the Fourier reconstruction is not particularly well-suited to the chemiluminescence profile, particularly the flat region at small radii, which cannot be well approximated by this fitting method. Given that the features and temporal spectra of interest occur at relatively large radii (r/x or larger) and that the area and Fourier methods give

virtually identical results in this region, the area method has been used in subsequent results for computational efficiency.

Returning to Tables 4.2 and 4.3, there are several trends of note. The first is that the errors in peak location are relatively low, on the order of 3-5% in most cases as compared to LIF results (Renfro *et al.*, 2000c), although two cases at x/D = 10 exhibit error on the order of 10%. This is likely due to the increased flame circumference at higher x/D values, which introduces errors in the Abel inversion due to the flame being larger than the depth of field. Reducing the aperture of the camera – which has the effect of increasing depth of field – improved this error slightly, but at the expense of sampling rate or spatial resolution (if additional binning is used to increase the sampling rate). Given this tradeoff, 10% was deemed to be acceptable reconstruction error. On the other hand, the profile FWHM shows much larger error at low x/D locations, on the order of 100-200%. This is likely due to the mismatch in spatial resolution between this work and the previous LIF results (Renfro *et al.*, 2000c). The CH layer is very thin in this region, and it sits outside the shear layer, so it is questionable whether it was spatially resolved by either the LIF or binned chemiluminescence measurements. Clemens and Paul (1995) previously showed that the reaction zone of turbulent hydrogen flames often sits outside the shear layer and exhibits laminar behavior at low x/D locations in turbulent jets. For these reasons, the best location to calculate frequency spectra is at x/D = 10, where the flame does not exhibit these re-laminarization effects; this location has been used for all subsequent comparisons to previous LIF results.

4.6 Results and Discussion

The power spectral densities resulting from the line-integrated chemiluminescence time series at x/D = 10 in all five flames are shown in Fig. 4.4. These PSD's have been calculated at the peak locations as determined by Abel inverting the mean intensity profiles via the area method, as described previously and listed in Table 4.2. Noise subtraction has been performed as described in Section 4.4, and each PSD has been filtered with a five-point moving average for clarity. All five PSD's are nearly flat at low frequencies, followed by a decay in the inertial subrange. This turndown occurs at higher frequencies with higher Reynolds numbers. This is expected, as increased turbulent kinetic energy at higher velocities requires smaller structures to dissipate energy. However, the PSD slopes in the inertial subrange are larger than found in previous LIF cases (Renfro *et al.*, 2000c). This indicates that the line-integrated chemiluminescence results contain a greater contribution from low frequencies, implying longer integral time scales, as will be discussed shortly. The A1 case also displays a unique feature in the region of 10-20 Hz, likely due to buoyancy effects, which are significant in the low velocity case.

The autocorrelation functions calculated from the PSD's shown in Fig. 4.4 are shown in the top panel of Fig. 4.5. Their general shapes, which appear to be exponential, compare well with previous work, and their decay rates increase generally with Reynolds number. The integral time scales calculated from these ACF's are listed in Table 4.4, as compared to previous LIF results (Renfro *et al.*, 2000c). In each case, the integral time scales have been calculated via two methods: by fitting an exponential function from $\Delta t = 0$ to $\rho(\Delta t) = 1/e$, and by integrating from $\Delta t = 0$ to the first time the ACF crosses the x-axis. The integral time scales calculated from the line-integrated chemiluminescence are universally larger than those calculated from the previous LIF results. This is expected due to out-of-plane contributions from regions with larger integral time scales. Previously, Renfro *et al.* (2000b) showed that the integral time scales of OH

increase with radial location; the same has been shown here, and will be discussed subsequently. For this reason, treating these measurements with an Abel inversion is necessary in order to recover useful local temporal information.

It should also be noted that the integral time scale calculated by integrating the ACF is generally larger than calculated by the exponential fit. The reasons for this may be seen in the bottom panel of Fig. 4.5, which shows the same ACF's as the top panel, but normalized by the integral time scales calculated via exponential fit. An exponential decay has been added for comparison, as exponential decays have previously been shown to be a useful approximation for time series in these and other turbulent flames (Renfro *et al.*, 2000a, Renfro *et al.*, 2000b, Renfro *et al.*, 2000c). The ACF's collapse well at small time intervals, but some deviate from the exponential decay at larger time intervals, particularly the A5 flame. In this case, the integral time scale calculated via integration is more than twice as large as that calculated via exponential fit. This deviation in the current work is likely due to out of plane contributions since contributions from large radii have longer integral time scales. Similar long tails in the ACF were also seen in some cases in previous work (Renfro *et al.*, 2000c); that is, an initial rapid decay was followed by a much slower asymptote toward zero correlation. Although this seemed to indicate that some cases could not be characterized by a single time scale, the specific reasons for this in the previous work were not discovered. All of these tails occurred at low axial heights where the flame can be intermittently laminar. The comparison between the current results, which explicitly include contributions from multiple time scale fluctuations in a path-integrated measurement may be a useful method for identifying and quantifying the impact of intermittency and its inherent multiple time scales on non-exponentiality in the ACF.

Figures 4.6 and 4.7 show the autocorrelation functions resulting from Abel inversion of the frequency spectra at x/D = 10 in flames A1-A5. The inversions have been performed on the Fourier transform of the time series and the amplitude of the Fourier transform of the time series, respectively, as previously discussed. Overall, these ACF's display significantly more noise than those in Fig. 4.5, which is to be expected due to error from large radii propagating to the inversion from smaller radii. However, they also exhibit shorter integral time scales as compared to the raw autocorrelation functions, which is also expected due to the Abel inversion reconstructing the spatially-resolved time scales that are shorter at small radii. This is reflected in the calculated integral time scales, shown in Table 4.4. The integral time scales arising from the Abel inversion of the magnitude of the Fourier transform are smaller than those arising from the Abel inversion of the entire Fourier transform. This compares well with previous work of Mayrhofer and Woisetschäger (2001), who exhibited success in Abel inversion of the magnitude in the absence of strong acoustic waves. In the most successful case, flame A5, the error is reduced by more than 80% by Abel inversion of the amplitude of the Fourier transform, to only 25% for the exponential fit. The calculated integral timescale is within the range of integral time scales calculated from the previous LIF data.

The necessity for Abel inversion of these temporal spectra is illustrated in Fig. 4.8, which shows the calculated integral time scales at x/D = 10 in the A5 flame as a function of radial location. These are the time scales resulting from Abel inversion of the magnitude of the temporal spectra, and the time scales have been calculated via exponential fit of the ACF's. The location of the peak Abel-inverted signal has been marked with a dotted line. As shown for previous OH LIF results (Renfro *et al.*, 2000c), the integral time scale increases with radial location. This trend is typical of all cases studied here, and indicates that line-integrated chemiluminescence

measurements in this axisymmetric flame will always include contributions from regions of the flame with longer time scales. This increases the measured time scale and calls for Abel inversion.

Figure 4.8 also illustrates a possible reason for remaining error in the calculated integral time scales: noise. Within 2 pixels of the peak signal location, the calculated integral time scale varies by as much as 60%. This noise is due to remaining noise in the frequency spectra, which is amplified in the Abel inversion process. Using the Fourier method rather than the area method for spectra inversion did not improve this; it appears noise in the original measurements is the limiting factor. This is an inherent problem with collecting high-speed measurements in which a relatively low signal to noise ratio occurs. Additionally, the camera used in this work is susceptible to spatial artifacts in conditions with low signal-to-noise, which is problematic when performing an Abel inversion. This is illustrated in Fig. 4.9, which shows the mean chemiluminescence profiles at x/D = 10 in the A5 flame at two sampling rates: 1.5 kHz and 31 kHz. The latter frame rate, which was used for collecting temporal statistics, is significantly less smooth, and this is not improved by collecting additional videos. The profile shape is due to consistent spatial artifacts that are amplified significantly at high frame rates, when signal is lower. These artifacts cannot be avoided with this particular camera without sacrificing spatial or temporal resolution, both of which are necessary for inverting frequency spectra and calculating integral time scales. Additionally, reducing the sampling frequency or spatial resolution increases the signal-to-noise ratio and prevents the PSD from reaching the noise floor, which is necessary for accurate noise subtraction.

Noise issues aside, the Abel inversion of frequency spectra magnitude shows promise for recovering local temporal statistics in axisymmetric flames. In order to better quantify the

effectiveness of Abel inversion without measurement error, it was applied to simulated time series. These time series were generated via the method described in (Renfro, 2000). First, a generalized PSD form, normalized by integral time scale, was generated from previous CH LIF results (Renfro *et al.*, 2000c). From this, a PSD was generated for a given integral time scale, and the magnitudes of the Fourier-transformed time series were calculated via

$$A(f) = \sqrt{\sigma^2 \cdot PSD(f)} \tag{4.14}$$

The phases of the frequency spectrum were assumed to be uncorrelated with themselves and were calculated via random number generation. This result was then treated with an inverse Fourier transform to produce a time series. Because the phase information is generated randomly – with one exception, which will be detailed – this method is capable of producing all possible time series for a given integral time scale, given infinite attempts (Renfro, 2000).

In order to assess error in the two Abel inversion techniques, time series c_A, c_A', and c_B were generated such that $\tau_A = \tau_A' = 0.5$ ms, and $\tau_B = 0.1$. Two approaches were taken: in one case, the phases of all three time series were generated randomly and independently. This is referred to as the uncorrelated case. In the correlated case, the phases of c_A and c_A' were generated randomly, but the phases of c_B were chosen such that they were correlated with those of c_A' ($R \approx 0.5$). One thousand time series were generated for each case, to remove noise effects. From each of these sets of time series, the sum of $c_A + c_B$ was calculated, which simulates the effects of line integration. The goal was to recover the temporal information of c_B by recalling that $\tau_A = \tau_A'$ and thus that the frequency content of c_A is theoretically equivalent to that of c_A'. The frequency content of c_B was estimated from the Fourier transform, as

$$\mathcal{F}(c_B) \approx \mathcal{F}(c_A + c_B) - \mathcal{F}(c_A') \tag{4.15}$$

and also from the magnitude of the Fourier transform, as

$$|\mathcal{F}(c_B)| \approx |\mathcal{F}(c_A + c_B)| - |\mathcal{F}(c_A')| \tag{4.16}$$

The former approach is expected to be negatively impacted by phase mismatch between c_A and c_A', while the latter is expected to be negatively impacted by cross-correlation between c_A and c_B.

These two approaches were applied to the uncorrelated and correlated cases, and the results are shown in Figs. 4.10 and 4.11, respectively, which show the autocorrelation functions of c_B, $c_A + c_B$, and c_B as estimated from each of the two methods described above. In each case, it can be seen that $c_A + c_B$ has a significantly longer integral time scale than c_B, due to the effects of line-of-sight integration. In both correlated and uncorrelated cases, recovering frequency content of c_B from the Fourier transform of $c_A + c_B$ is less successful than inverting the magnitude of Fourier transform only. This seems to indicate that phase mismatch between c_A and c_A' has a greater impact on error than cross-correlation between c_A and c_B. However, the recovered autocorrelation functions still exhibit error.

The reasons for this can be understood by examining the cross-correlation between c_A and c_B. The sum of $\rho_{AB} + \rho_{BA}$ is shown for the correlated and uncorrelated cases in Fig. 4.12. These have both been normalized by the cross-correlation of the correlated cases at $\Delta t = 0$ for better comparison. The correlated case has a strong cross-correlation between c_A and c_B which decays nearly exponentially. The effect of this is that the recovered ACF of c_B is larger over all time delays. On the other hand, the correlation between c_A and c_B in the uncorrelated case is approximately zero over all time delays. This causes the error of the recovered ACF of c_B to be small at small time intervals, where the cross-correlation terms are small with respect to the autocorrelations of c_A and c_B. The error in the recovered ACF appears as a long "tail." This may

offer a possible explanation for the "tails" seen in the previous work of Renfro *et al.* (2000). This behavior occurred at low x/D locations, where the flame sits outside the turbulent shear layer and displays intermittent turbulent as well as laminar behavior. Thus, the measured integral time scales in these regions may actually contain two types of behavior: high-frequency turbulent fluctuations, which would contribute a rapid initial decay in the ACF, and low-frequency laminar behavior, which would contribute the long tail.

With respect to the integral time scales recovered via Abel inversion, it seems that cross-correlation among the constituent measured time series is a source of error in addition to measurement error. This effect cannot be directly quantified or eliminated in the current work; despite this, Abel inversion shows promise for recovering integral time scales from chemiluminescence of axisymmetric turbulent flames. In non-axisymmetric cases, an Abel inversion cannot be used, and the results shown here have demonstrated that line integration can have complex effects on the measured integral time scales. In quasi-two-dimensional flows, a path-integrated measurement taken along the uniform dimension could yield a relatively accurate integral time scale, as an ensemble average of time series with identical frequency content theoretically has the effect of decreasing the ratio of signal rms to average, but not of changing the measured integral time scale. However, a more complex flow with significant variation in time scales along the line of sight would require more study. In some cases, a narrow depth-of-field imaging system such as the one described in Chapter 3 could be applied to reduce the impact of out-of-plane frequency content.

4.7 Tables

Table 4.1: Flow and experimental parameters for the five flames measured in the time series study.

Flame	$\bar{V}$ [m/s]	Re	Time Series Sampling Rate [Hz]	Average Profile Sampling Rate [Hz]
A1	16.3	2800	6000	1500
A2	29.0	5000	10,000	1500
A3	52.3	9000	25.000	1500
A4	75.5	13,000	28,000	1500
A5	88.3	15,200	31,000	1500

Table 4.2: Location of peak signal (r/x) obtained via three different inversion methods, as compared to previous LIF data.

Flame	**x/D**	**LIF** (Renfro *et al.*, 2000c)	**Chemiluminescence** Area Method	Fourier Method	Assumed Gaussian	**Area Method % Error**
A1	1	0.96	0.96	1.04	1.05	5.74
A1	2	0.53	0.56	0.58	0.57	7.21
A1	5	0.24	0.25	0.26	0.25	5.79
A1	10	-	0.12	0.13	0.13	n/a
A2	1	0.86	0.88	0.92	0.91	5.14
A2	2	0.48	0.46	0.50	0.50	1.16
A2	5	0.21	0.21	0.22	0.22	3.32
A2	10	0.13	0.13	0.13	0.13	1.18
A3	1	0.77	0.77	0.80	0.80	2.45
A3	2	0.42	0.40	0.42	0.42	1.15
A3	5	0.20	0.20	0.20	0.20	0.10
A3	10	0.14	0.13	0.13	0.13	9.76
A4	1	0.70	0.73	0.73	0.76	5.43
A4	2	0.40	0.40	0.40	0.41	1.31
A4	5	0.20	0.19	0.20	0.20	1.50
A4	10	0.13	0.14	0.13	0.13	1.44
A5	1	0.70	0.70	0.74	0.73	2.95
A5	2	0.39	0.39	0.41	0.40	1.64
A5	5	0.19	0.20	0.20	0.20	5.32
A5	10	0.12	0.14	0.13	0.13	10.64

Table 4.3: Signal profile FWHM obtained via three different inversion methods, as compared to previous LIF data.

Flame	x/D	LIF (Renfro *et al.*, 2000c)	Chemiluminescence Area Method	Chemiluminescence Fourier Method	Chemiluminescence Assumed Gaussian	Area Method % Error
A1	1	0.39	1.19	1.42	1.28	205.13
A1	2	0.53	1.49	2.00	1.50	181.13
A1	5	0.87	1.86	1.98	1.76	113.79
A1	10	-	2.41	2.03	1.90	n/a
A2	1	0.39	0.97	1.30	1.05	148.12
A2	2	0.43	1.29	1.38	1.23	200
A2	5	0.64	1.39	1.50	1.28	117.19
A2	10	1.75	1.52	1.73	1.58	13.14
A3	1	0.29	0.59	1.01	0.74	103.44
A3	2	0.38	0.57	1.09	0.77	50
A3	5	0.53	0.86	1.25	0.99	62.26
A3	10	1.54	1.58	1.79	1.51	2.59
A4	1	0.31	0.30	1.05	0.40	3.23
A4	2	0.37	0.40	0.88	0.45	8.11
A4	5	0.62	0.65	1.18	0.76	4.83
A4	10	1.69	1.59	2.08	1.74	5.92
A5	1	0.31	0.33	0.96	0.60	6.45
A5	2	0.41	0.48	1.23	0.64	17.07
A5	5	0.71	0.93	1.21	0.90	30.99
A5	10	2.11	1.41	2.07	1.64	33.17

Table 4.4: Comparison of calculated integral time scales at x/D = 10 from exponential fit (Exp. Fit) and integration (Int.) from LIF (Renfro *et al.*, 2000c), line-integrated chemiluminescence, and two Abel inversion approaches.

Flame	**LIF**		**Line Integrated**			**Abel-Inverted Fourier Transform**			**Abel-Inverted Fourier Magnitude**		
	Exp. Fit	Int.	Exp. Fit	Int.	Exp. Fit % Error	Exp. Fit	Int.	Exp. Fit % Error	Exp. Fit	Int.	Exp. Fit % Error
A2	0.20	0.23	0.31	0.42	59.31	0.30	0.75	55.08	0.28	0.78	45.08
A3	0.10	0.11	0.16	0.23	53.08	0.16	0.26	54.21	0.13	0.30	30.40
A4	0.07	0.10	0.23	0.28	231.28	0.18	0.23	161.76	0.13	0.18	86.59
A5	0.08	0.12	0.19	0.39	125.75	0.14	0.21	68.32	0.10	0.11	24.21

Flame	**LIF**		**Line Integrated**			**Abel-Inverted Fourier Transform**			**Abel-Inverted Fourier Magnitude**		
	Exp. Fit	Int.	Exp. Fit	Int.	Exp. Fit % Error	Exp. Fit	Int.	Exp. Fit % Error	Exp. Fit	Int.	Exp. Fit % Error
A2	0.20	0.23	0.31	0.42	59.31	0.30	0.75	55.08	0.28	0.78	45.08
A3	0.10	0.11	0.16	0.23	53.08	0.16	0.26	54.21	0.13	0.30	30.40
A4	0.07	0.10	0.23	0.28	231.28	0.18	0.23	161.76	0.13	0.18	86.59
A5	0.08	0.12	0.19	0.39	125.75	0.14	0.21	68.32	0.10	0.11	24.21

4.8 Figures

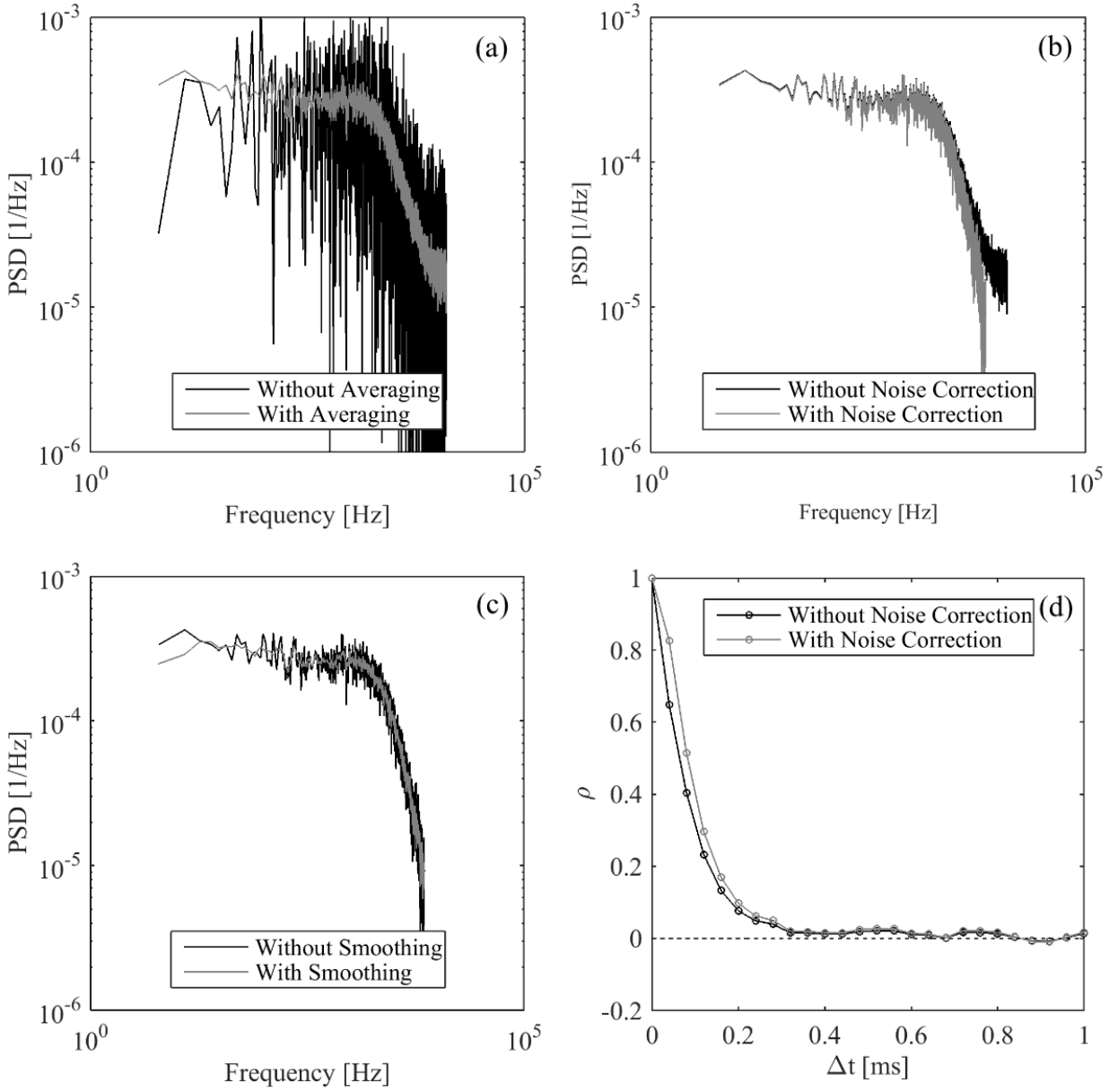

Figure 4.1: Power spectral density processing. The effects of (a) averaging, (b) noise correction, and (c) smoothing on the PSD are shown, as well as the effect of (d) noise correction on the autocorrelation function, as defined in Eqn. (2.12).

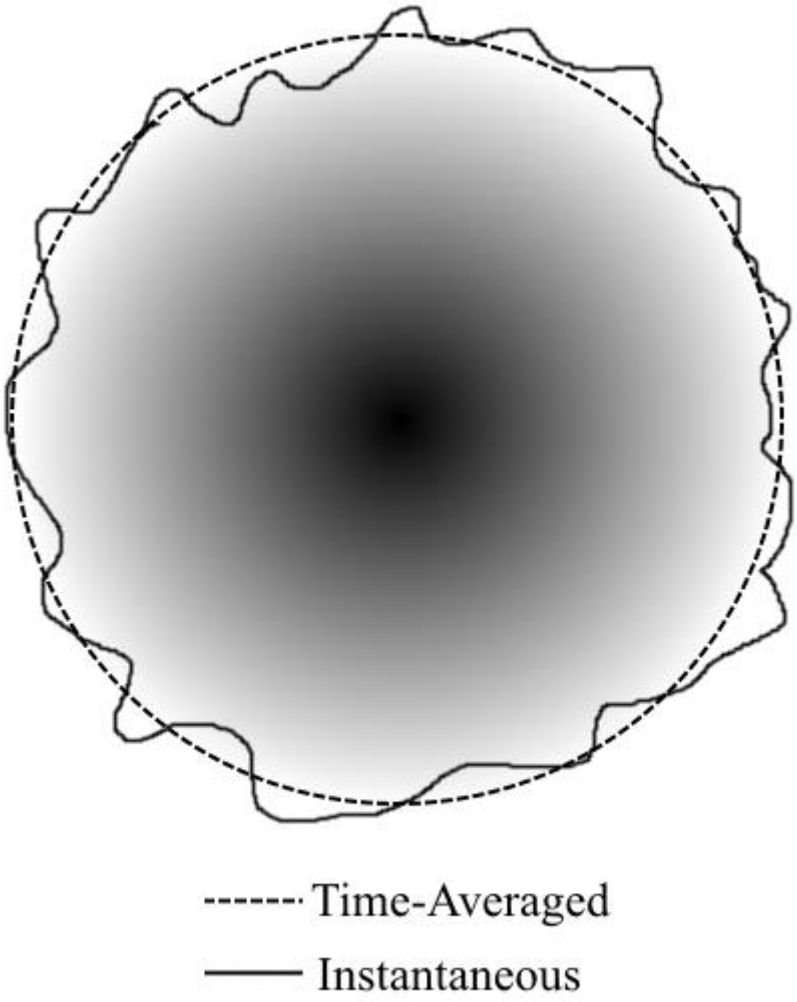

Figure 4.2: A top-down representation of a turbulent flame issuing from a circular jet. The instantaneous flame is not axisymmetric, but the time-averaged flame is.

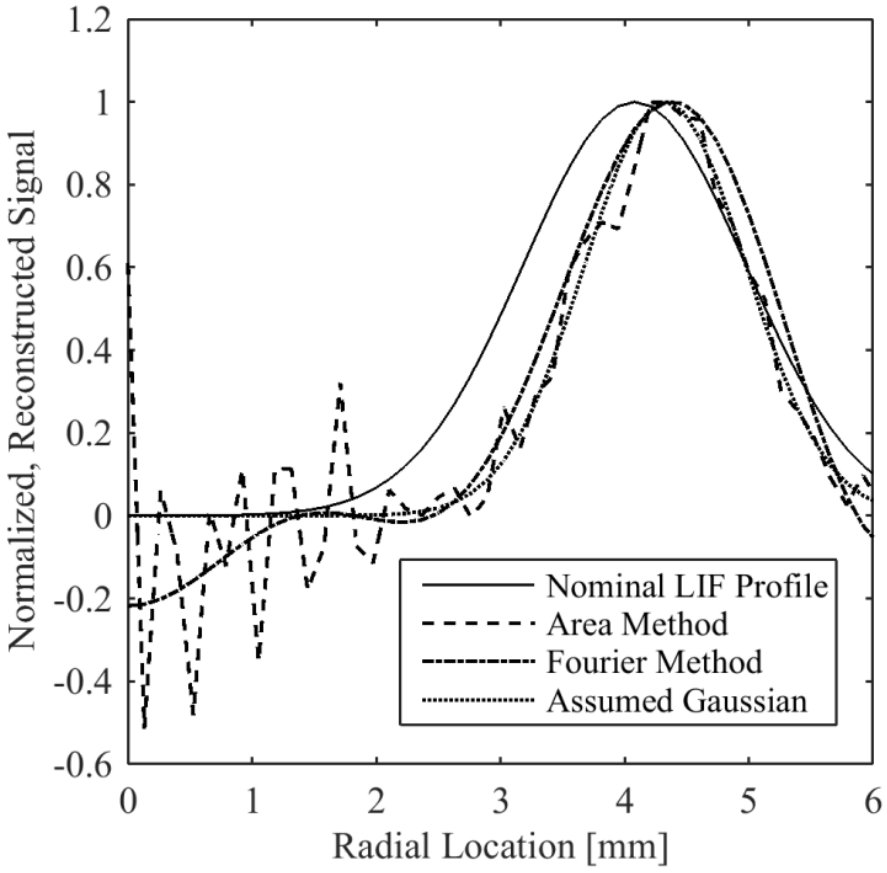

Figure 4.3: Comparison of nominal LIF profile at x/D = 10 (Renfro *et al.*, 2000c) in the A5 flame with reconstructed profiles via area method Abel inversion, Fourier method inversion, and a presumed Gaussian least squares fit.

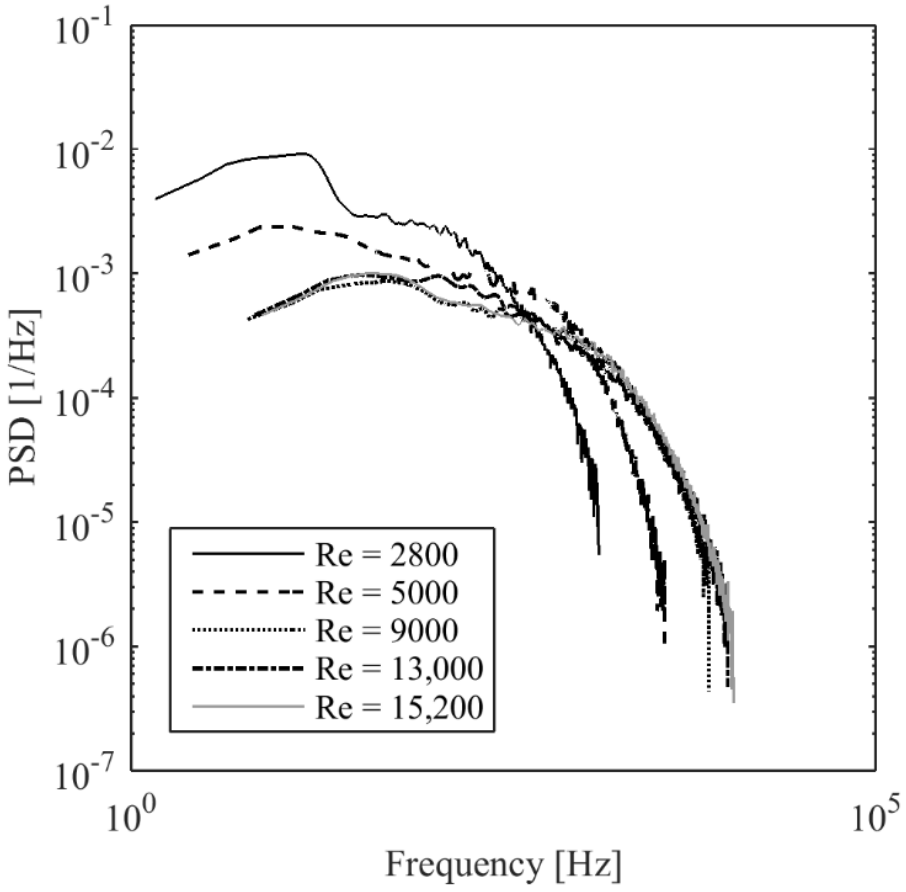

Figure 4.4: Power spectral densities from the location of peak Abel-inverted signal at x/D = 10 in flames A1-A5. Noise has been subtracted, and all PSD's have been filtered with a five-point moving average.

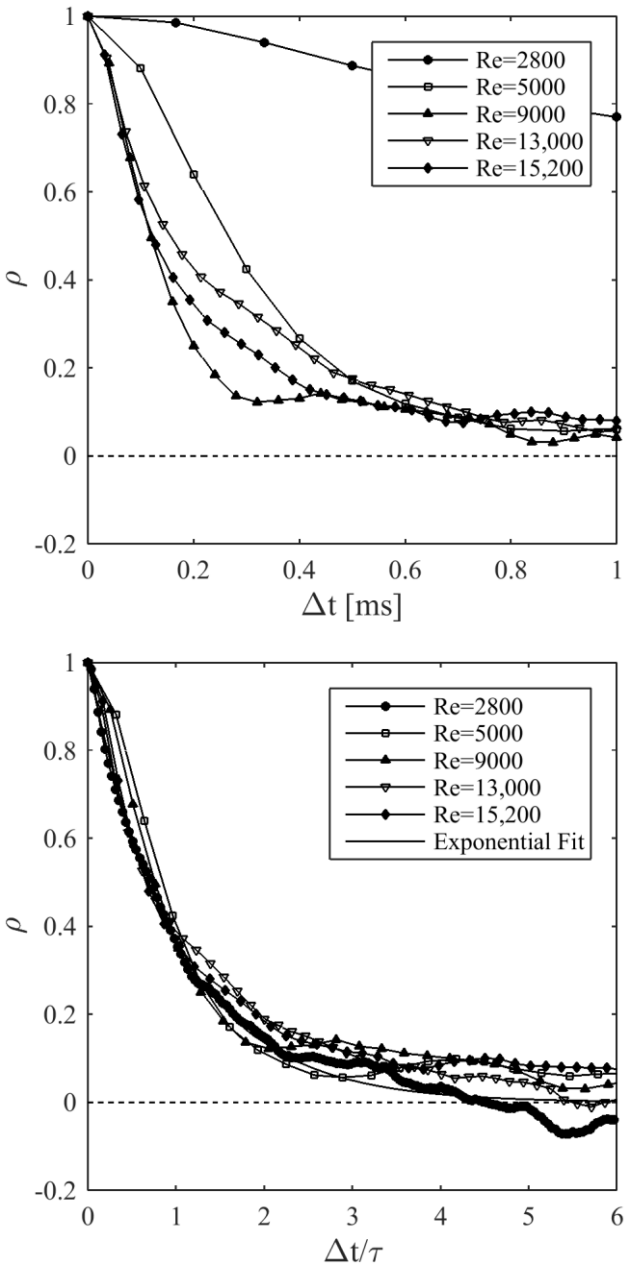

Figure 4.5: Autocorrelation functions from the location of peak Abel-inverted signal at x/D = 10 in flames A1-A5. Top: original. Bottom: normalized by integral time scale.

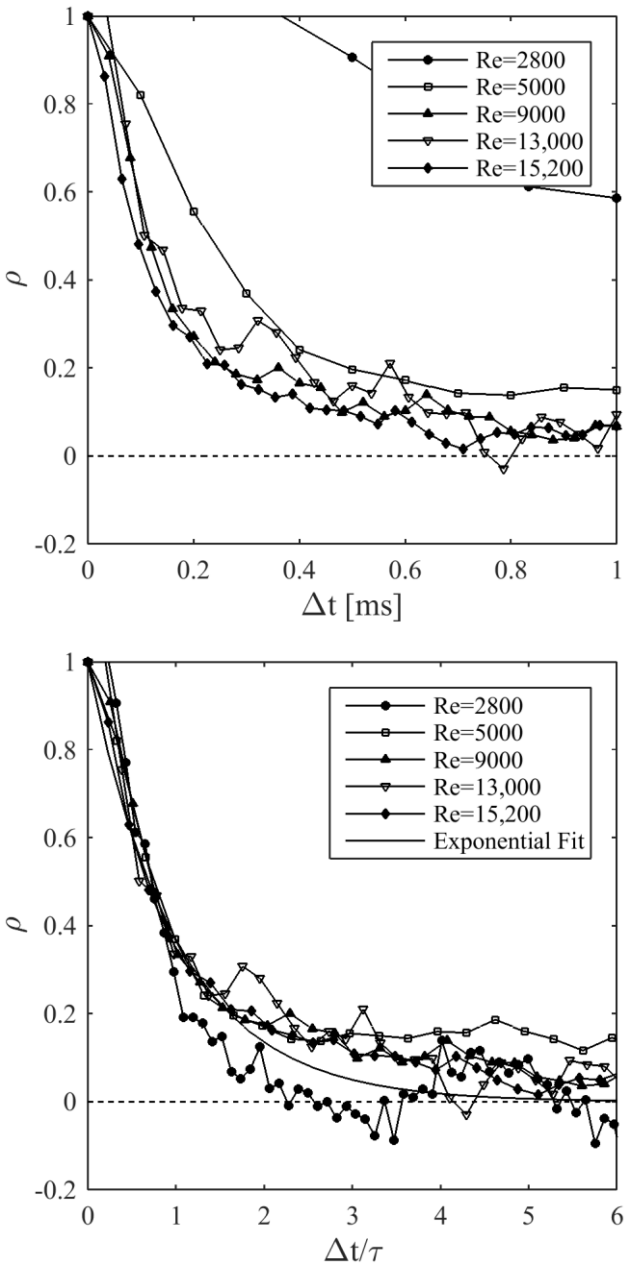

Figure 4.6: Autocorrelation functions from the location of peak Abel-inverted signal at $x/D = 10$ in flames A1-A5 resulting from the Abel inversion of the Fourier transform of the time series. Top: original. Bottom: normalized by integral time scale.

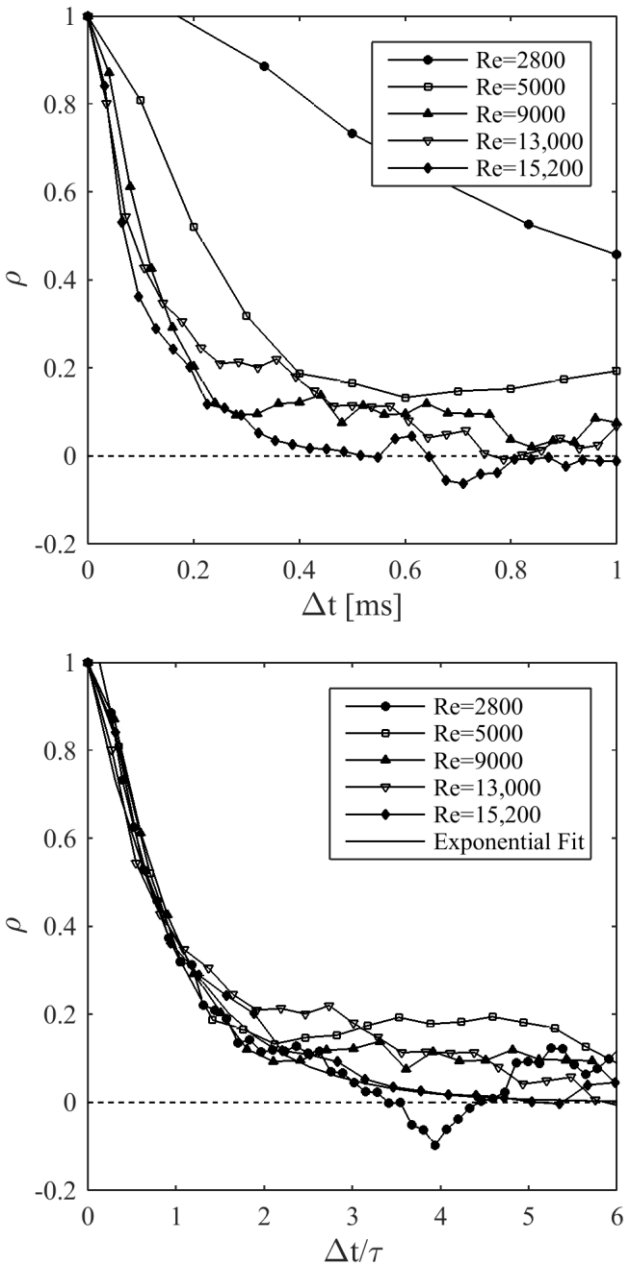

Figure 4.7: Autocorrelation functions from the location of peak Abel-inverted signal at $x/D = 10$ in flames A1-A5 resulting from the Abel inversion of the Fourier transform magnitude of the time series. Top: original. Bottom: normalized by integral time scale.

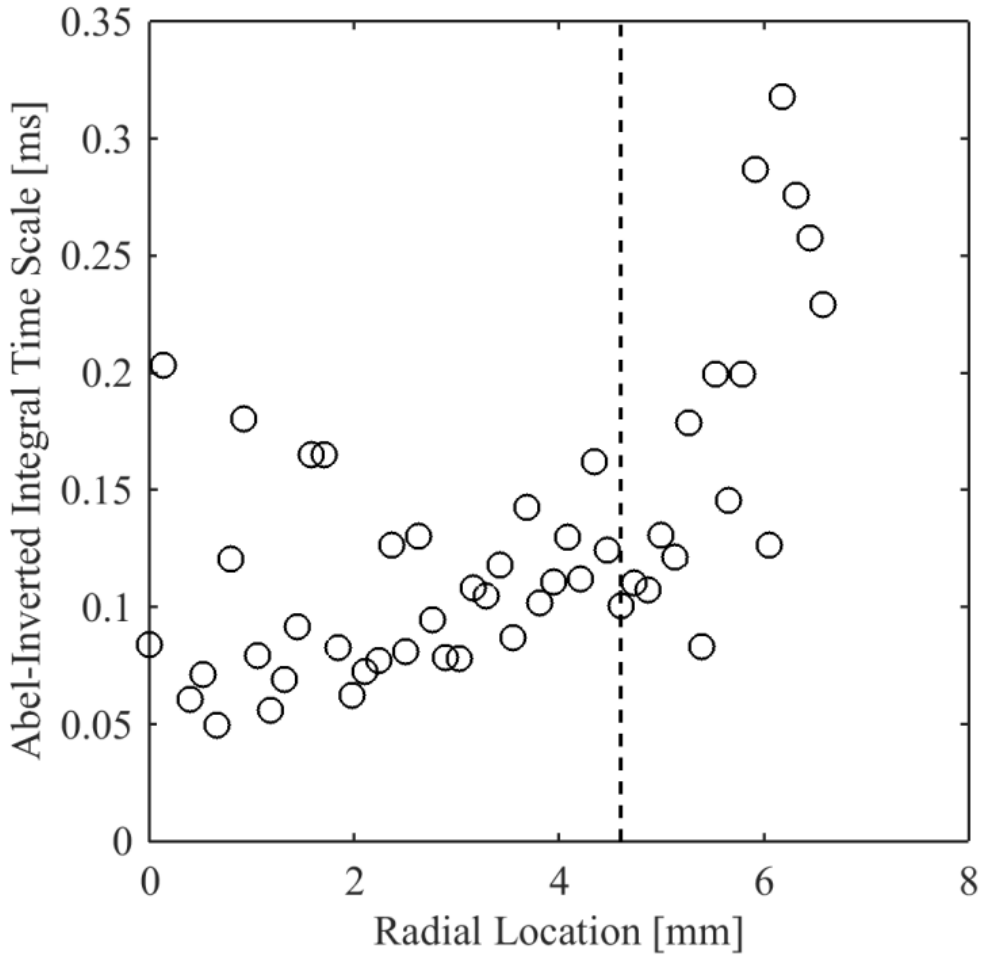

Figure 4.8: Radial dependence of integral time series resulting from Abel inversion at x/D = 10 in the A5 flame. The location of peak Abel-inverted signal is indicated with a dotted line.

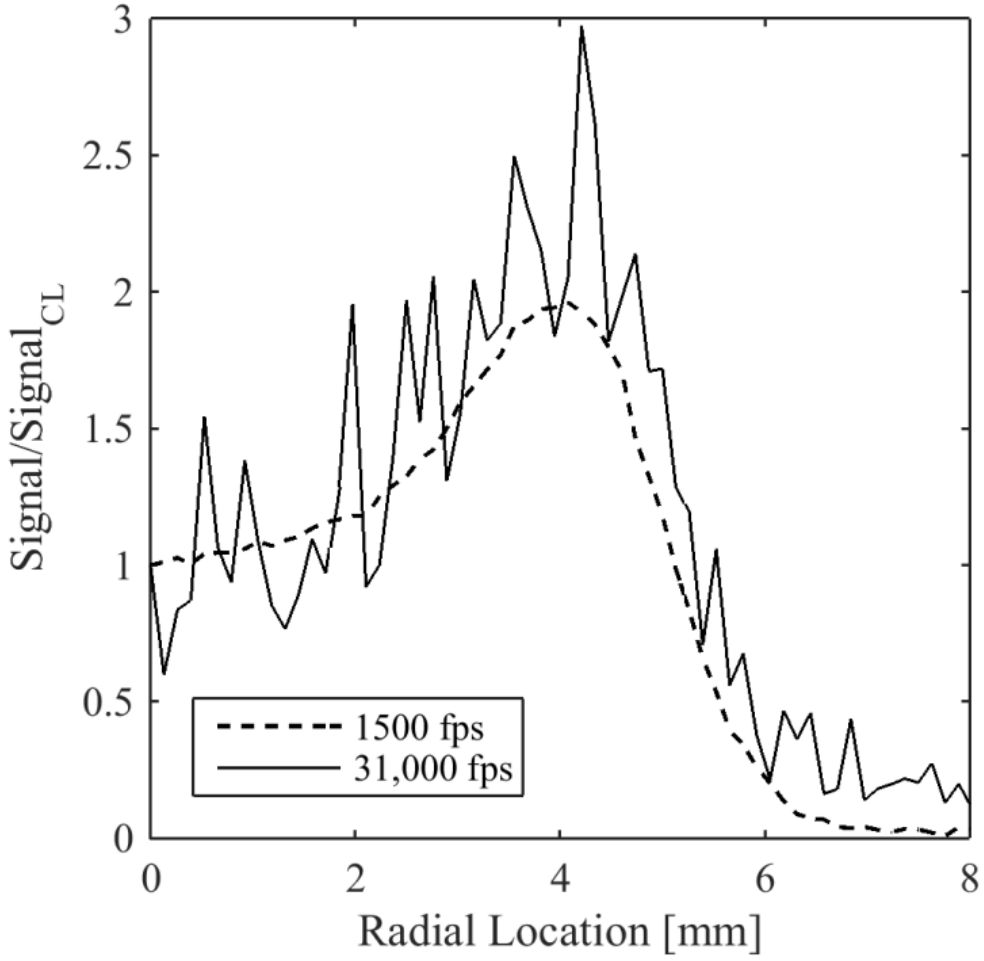

Figure 4.9: Mean signal profiles taken at 1500 and 31,000 fps at x/D = 10 in the A5 flame. Profiles have been normalized by their centerline values.

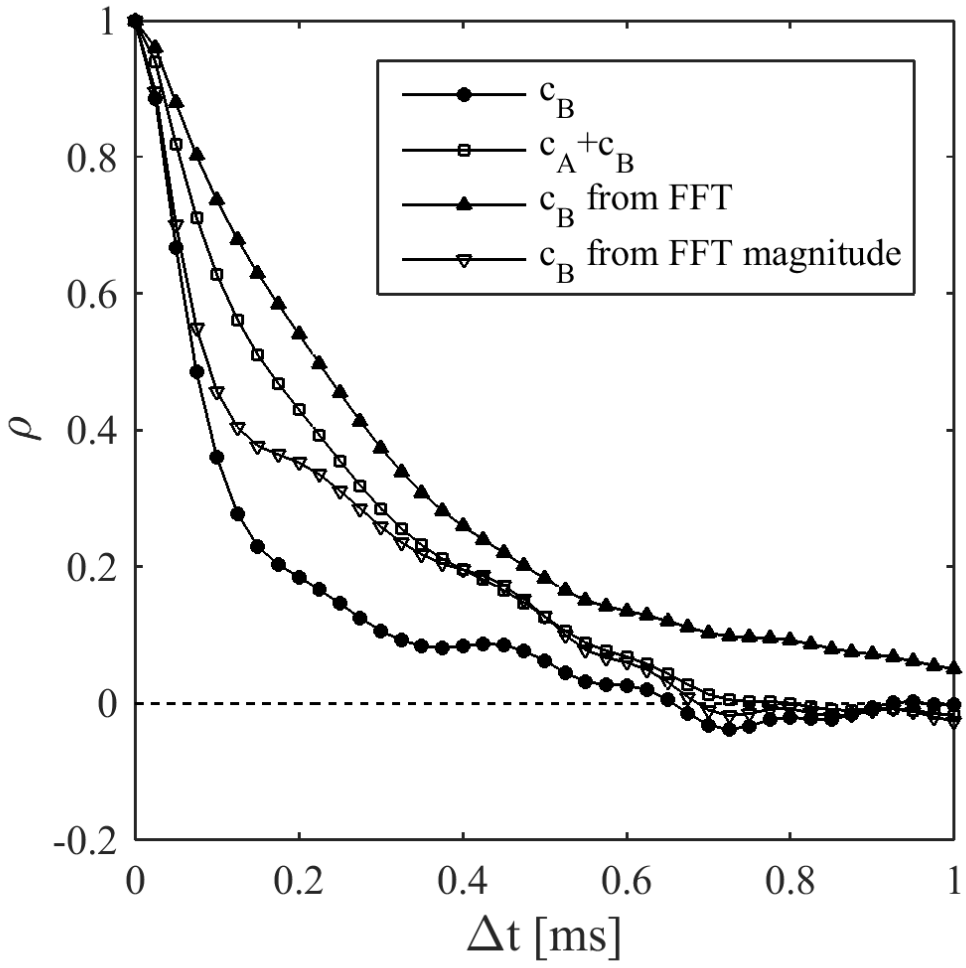

Figure 4.10: Comparison of autocorrelation techniques resulting from FFT and FFT magnitude inversion techniques, as applied to simulated, uncorrelated time series.

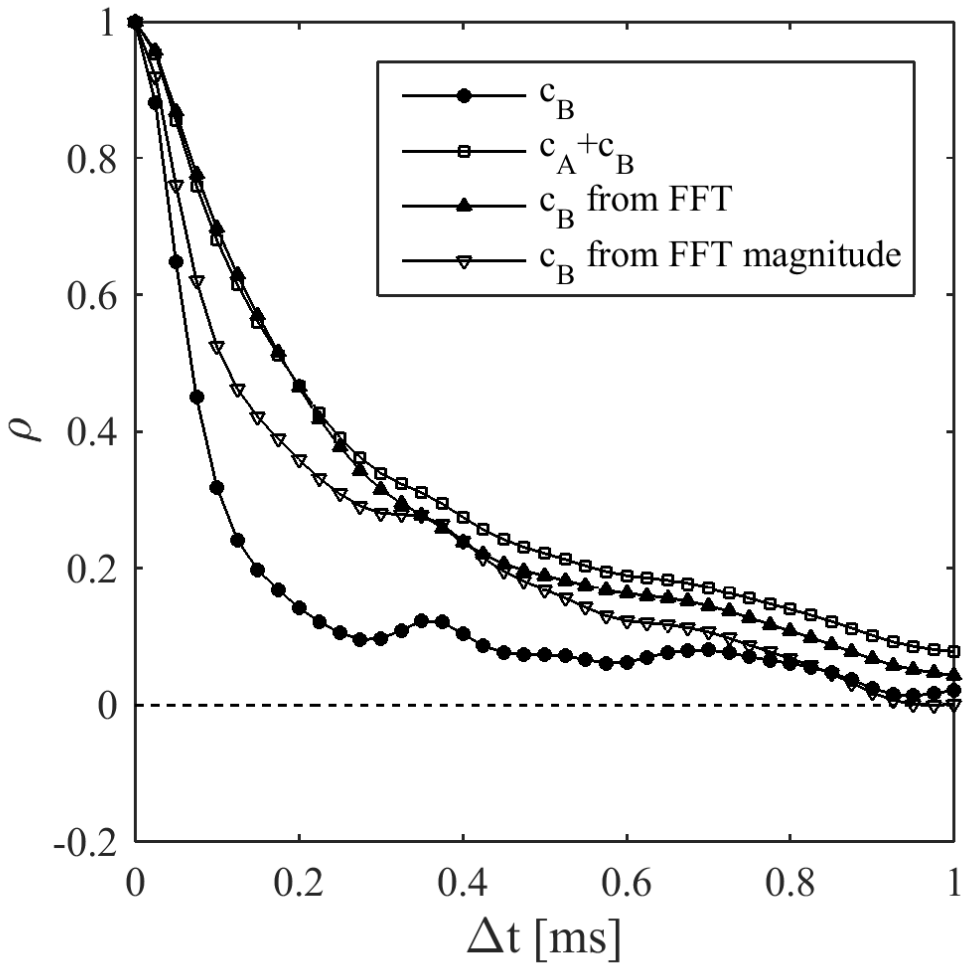

Figure 4.11: Comparison of autocorrelation techniques resulting from FFT and FFT magnitude inversion techniques, as applied to simulated, correlated time series.

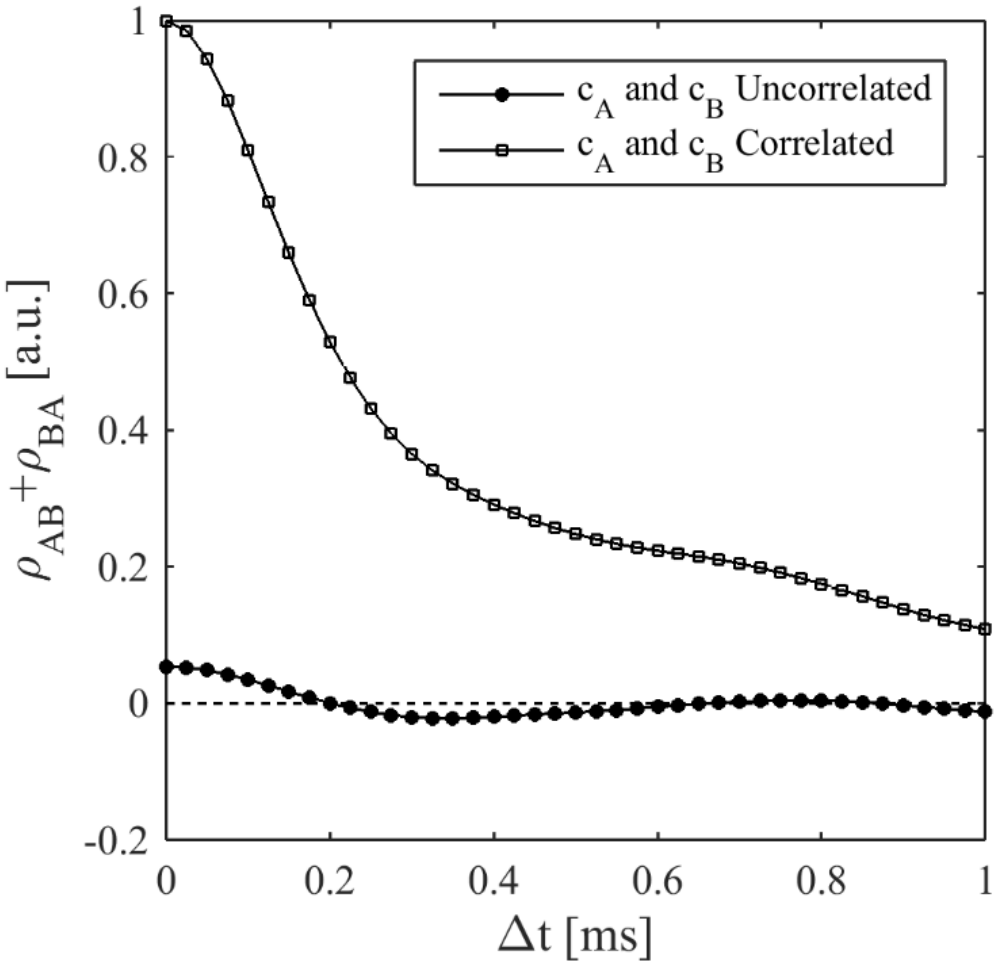

Figure 4.12: Sum of cross-correlation terms resulting from uncorrelated and correlated simulated time series.

5. Measurement of Scalar Dissipation Rate in a Negative Edge Flame

5.1 Background and Motivation

Formaldehyde fluorescence has been used extensively in combustion studies due to its close tie for formyl radical production via the reaction $OH+CH_2O \rightarrow HCO+H_2O$, which correlates well with heat release. The multiplication of CH_2O and OH fluorescence signals is useful for heat release and flame front measurements (Paul and Najm, 1998). Formaldehyde is also an attractive diagnostic because it may be excited at 355 nm, the third harmonic of an Nd:YAG laser (Fayoux *et al.*, 2005). Additionally, simulations utilizing detailed kinetics have shown that a decrease in CH_2O alone can be an excellent marker of peak heat release zones (Santoro *et al.*, 2000). Recent work (Kyritsis *et al.*, 2004, Bijjula and Kyritsis, 2005) has suggested that the thickness of the formaldehyde layer can serve as a marker for scalar dissipation rate because of its persistence in cooler regions outside the heat release region. The ability to estimate local scalar dissipation rates via a single diagnostic is desirable because measuring scalar dissipation rate directly is complex and expensive. It requires measuring a number of major and minor species with good accuracy, such that a gradient might be taken. Only a handful of laboratories are currently capable of making this measurement, which requires multiple lasers and cameras, including optical access in many directions. This approach is also unachievable in many practical burners.

Unfortunately, CH_2O excitation at 355 nm exhibits strong temperature dependence and unknown fluorescence quenching rates (Brackmann *et al.*, 2003). Kyritsis *et al*. (2004) showed that the Boltzmann fraction dependence has little influence on formaldehyde layer width, and Metz *et al.*

(2004) have made suggestions for fluorescence quenching corrections. In flames with local extinction, characterization of the local scalar dissipation rate is necessary to understand the conditions at the extinction point, which can differ significantly from those of 1-D counterflow diffusion flame studies due to the impact of additional heat transfer processes (Carnell and Renfro, 2006). If formaldehyde fluorescence can provide a sufficient measure of scalar dissipation rate even in the presence of local extinction, then a relatively simple diagnostic for extinction studies can be developed.

5.2 Specific Objectives

This chapter presents a series of measurements and simulations of formaldehyde fluorescence in a unique counterflow burner containing a stationary, off-axis extinction point. The relationship between scalar dissipation rate and formaldehyde fluorescence profile through the extinction region is examined. The feasibility of using formaldehyde fluorescence as a marker for scalar dissipation rate in the presence of a local extinction event is examined, and specific suggestions about the application of this technique to turbulent flames are made.

5.3 Experimental Setup

This study was carried out in a similar geometry to previous work in which an off axis extinction point was formed in a counterflow burner (Carnell, Jr. and Renfro, 2005). The burner in the current study, shown in Fig. 5.1, consists of a central converging nozzle of 20-mm diameter

surrounded by an outer coannular nozzle of 48-mm diameter. Honeycomb flow straighteners are placed at the exit of the outer nozzle to assure a uniform axial exit velocity. A detailed description of the burner apparatus and flow system is discussed in (Carnell, Jr. and Renfro, 2007). Low velocity (10 cm/s or 20 cm/s) fuel (20% CH_4, 80% N_2) versus air in the inner nozzle was used to establish a stable non-sooting counterflow diffusion flame. The outer nozzle issued the same fuel versus air at an increased velocity (40 cm/s or 60 cm/s) causing a radial increase in scalar dissipation and steady off-centerline extinction of the stable counterflow diffusion flame. Three flames were investigated; 10:40, 20:40, and 20:60 (V_i:V_o, inner nozzle velocity:outer nozzle velocity). The flames appear similar to those formed in a standard counterflow study where guard flow causes extinction of the flame through dilution; however, the extinction point in the current flame occurs in a burnable mixture and is caused only by increasing scalar dissipation. The steady off-centerline extinction point happens in a region where differential diffusion effects are significant (Carnell, Jr. and Renfro, 2006).

OH and CH_2O species concentrations in the flame were examined using PLIF imaging. The multiplication of their concentrations can be used for investigation of the forward reaction rate for $CH_2O+OH \rightarrow HCO+H_2O$ as demonstrated by (Paul and Najm, 1998). For OH measurements, the doubled output from a Spectra Physics Pro-230-10 Nd:YAG laser was used to pump a Sirah Precision Scan dye laser, as shown in Fig. 5.2. Rhodamine 590 dye was used and the fundamental beam was frequency doubled to generate a ~7-ns laser pulse at ~285 nm exciting the $P_1(7)$ transition in the (1,0) X-A vibronic band. Measurements reported here were taken with pulse energies of approximately 1.67 mJ, which produced a linear signal. Excitation of the $P_1(7)$ transition is selected to minimize temperature sensitivity, as simulations performed indicate OH and CH_2O exist together in a very narrow temperature band and are not expected to require

significant corrections for reaction rate calculations, although this is discussed further. The tripled output of the Spectra Physics laser was utilized for the CH_2O PLIF measurements with pulse energies of approximately 90 mJ as in the work of Fayoux *et al.* (2005). As shown in Fig. 5.2, both beams are aligned with one another by passing through apertures situated on either side of the counterflow burner and focused into a plane using a 500 mm focal length cylindrical lens.

All fluorescence was collected at 90º from the laser plane. A UV-Nikkor 105-mm f/4.5 lens was utilized to image the fluorescence signals onto a DEP-GenII image intensifier. CH_2O and OH images were not recorded simultaneously allowing the same collection optics, intensifier, and camera to be used for both species. The flame was continuously run during the collection of both fluorescence signals. A filter centered around 308±5 nm was placed between the Nikkor lens and the image intensifier and the 355 beam was blocked during the collection of OH signal. This filter was replaced with an Omega Optical Inc. (450DF70D) filter which blocked signal associated with scattering from the burner surface while passing visible florescence signal during the CH_2O PLIF measurements. This filter has greater than 60% transmission at wavelengths between 425 and 485 nm and near zero transmission below 410 nm and above 490 nm. The last OH mirror was removed for CH_2O imaging. This procedure ensured that the pixel by pixel multiplication of the two fluorescence signals for reaction rate imaging was not affected by image alignment.

The small collection angle of the imaging system eliminated vignetting effects for the range of axial locations examined. The phosphor image from the intensifier was collected using a 150-mm focal length lens coupled to a Nikkor 50-mm lens and a 1317×1035 Photometrics series 300 liquid-cooled camera. The intensifier was gated open for approximately 1 μs for each laser pulse and was masked in order to avoid saturation from laser scatter from the burner surface.

Prior to the OH measurements,a cuvette filled with fluorescing material was placed in the laser path and used for flat field corrections5000 shots were integrated on-chip forming a beam distribution image utilized for correcting the subsequent OH image. The flame was then lit, the appropriate filter was placed in front of the intensifier, and 2000 shots were integrated on-chip for the OH image. The last mirror of the 285 nm beam was removed, the 355nm beam was unblocked, the filter for the CH_2O measurements was interchanged with the OH measurement filter, and 5000 shots were integrated on-chip forming the CH_2O image. No appreciable flame variability is evident when comparing the individual images, consistent with the stability of these extinction flames (Carnell, Jr. and Renfro, 2005). Finally, the filter was removed, the burner was translated out of the beam path, and a methane jet (42 mm by 26 mm) was placed below the imaging plane. A methane jet was used in flat field corrections for formaldehyde fluorescence due to scattering off the coutnerflow burner in the absence of the filter. 600 shots were integrated on-chip for the CH_2O beam distribution correction.

5.4 Numerical Methods

Two-dimensional simulations of the local extinction flame were computed on the numerical mesh over half the counterflow burner, shown with respect to the physical geometry of the burner in Fig. 5.1. The boundary conditions are also included in Fig. 5.1. The mesh consists of 60,000 square cells of variable size with a maximum resolution of 50 μm centered on the extinction region. UNICORN (Unsteady Ignition and Combustion with ReactioNs), a time-dependent axisymmetric model which solves the Navier-Stokes and species- and energy-conservation equations in cylindrical coordinates, was used (Katta *et al.*, 2004). The current

simulations utilized GRI-Mech 1.2 chemistry (Frenklach *et al.*, 1995) plus nitrogen, with 32 total species and 350 reactions among the constitutive species.

The QUICKEST scheme (Spalding, 1972) was implemented to obtain finite-difference forms of the momentum equations. Species and energy equations were found using a combination of upwind and central differencing. The pressure field is calculated by using LU (lower and upper diagonal) decomposition to solve all Poisson equations simultaneously at each time step (Leonard, 1979).

The nozzles were modeled as uniform velocity inlets. This is expected to be more accurate for the outer nozzles, in which honeycomb was used in the experiments. Previous modeling of the inner converging nozzle by Carnell (Carnell, Jr., 2006) showed that the velocity profile is non-uniform by up to approximately 10%. However, this is expected to have minimal effect on the simulated fluorescence profiles, and the simulation was limited to uniform profiles.

5.5 Results and Discussion

Figures 5.3 and 5.4 show the PLIF signals for OH and CH_2O over half of the burner for the 10:40 and 20:40 flames, respectively as well as the forward reaction rate determined by multiplication of the signals. Corrected OH signal for the 10:40 flame, top panel Fig. 5.3, remains constant in axial peak intensity throughout the inner nozzle region up to 10 mm from the centerline. Within this region, the OH contours display a slight curvature, the peak OH signal is closer to the fuel nozzle on the burner centerline than at the outer region of the inner nozzle. At approximately 11 mm from the centerline, the OH signal thins considerably due to the higher

velocity issuing from the outer nozzles. The peak OH signal decreases ~12.5 mm from the burner centerline, falling below 10% of the centerline value at 16.4 mm from the centerline. This decrease in OH signal occurs due to local extinction of the flame. Beyond this point, combustion products mix with unburned fuel and air in a high strain region of the flow and the temperature decreases rapidly (Carnell and Renfro, 2006, 2007). Peak axial corrected OH signal for the 20:40 flame, top panel Fig. 5.4, remains constant within the inner nozzle region, but displays none of the curvature evident in the 10:40 flame case. At a radial position of 9.8 mm the peak axial OH signal begins to fall rapidly, dropping to below 10% of the centerline value by 15.2 mm. This earlier extinction is expected due to the higher strain within the inner nozzle in the 20:40 case.

The peak axial corrected CH_2O signal for the 10:40 flame, shown in the middle panel of Fig. 5.3, remains constant for only the first 3 mm from the burner centerline. It then increases, reaching 200% of the centerline value by 12.5 mm from the centerline. At this point, the peak intensity rapidly increases, reaching a value of seven times the centerline signal at a radial location of 22 mm from the centerline, due to incomplete combustion occurring in the hot combustion product stream. The turbulent flame measurements of Ayoola *et al*. (2006) exhibited the same increase in formaldehyde signal following extinction. The formaldehyde profile is very wide within the inner nozzle, due to the persistence of formaldehyde in lower temperature regions outside of the reaction zone. Therefore, capturing the entire axial expanse over all radial positions is not possible due to limitations of the laser beam width. PLIF signal above 4.6 mm is disregarded as the laser energy distribution has fallen to below 50% of the peak intensity. Due to the limitation involving the laser beam width, the onset of thinning of the CH_2O signal is difficult to quantify for the 10:40 flame, but thinning is evident starting at a radial location of 10 mm. Significant differences in the CH_2O signal of the 20:40 flame, middle panel of Fig. 5.4, as compared to the

10:40 flame are evident. Peak axial CH_2O signal increases radially until it reaches a value of 125% of the centerline value 12.5 mm from the burner centerline. At this point a rapid increase is seen with peak axial CH_2O signal reaching a maximum, approximately 2.5 times the centerline value, at a radial position of 20.5 mm after which it gradually decreases.

Figures 5.5 and 5.6 show the simulated OH and CH_2O signals, as well as the multiplication of the signals. Velocity streamlines have been overlaid to better understand the flow behavior. Both images represent simulated fluorescence signal including Boltzmann fraction distribution, as opposed to concentrations such that the simulations can be directly compared to the measurements. OH fluorescence quenching has been included as per (1998). The overall trends compare well to the measured signals, although several differences may be seen. First, all profiles (OH, CH_2O, and heat release) are thinner in the simulated signals. Despite that, the simulations correctly predict earlier extinction in the 20:40 flame as compared to the 10:40 flame, and the formaldehyde signals peak in the outer nozzles due to increased production in the hot products streams. Fuel diluted in nitrogen issues from the top of the burner, while air issues from the bottom of the burner. In both cases, formaldehyde production occurs due to the leakage of oxygen past the flame via convection and diffusion. The streamlines in Figs. 5.5 and 5.6 show that the simulated heat production region sits slightly to the air side of the dividing streamline. The flame edge is fed with hot products from the flame itself. Increased formaldehyde signal after extinction is due to the mixing of these hot products with cool air from the outer nozzles, which cools the mixture slightly and allows diffusion of intermediate species such as formaldehyde toward the air side of the flame.

Figure 5.7 shows the centerline axial OH and CH_2O signal profiles for the 10:40 flame compared to the simulations. The simulation output has been shifted such that the peak OH

signal aligns with the peak measured signal. Additionally, the OH profile predicted by UNICORN has been corrected for Boltzmann distribution and fluorescence quenching (Tamura *et al.*, 1998) to simulate fluorescence signal. The measured OH signal profile has a full width half maximum (FWHM) value of 1.37 mm, as compared to 0.85 mm for the measurements. This is attributed to the spatial resolution of the intensifier used in the measurements. In the 20:40 case, seen in Fig. 5.8, the OH data FWHM is 1.20 mm while the simulations predict 0.6 mm. This equates to approximately a 12% reduction in width caused by a higher strain field as compared to the 10:40 flame case, less than the predicted 29% reduction seen in the simulations indicating that the strain on the centerline has not increased proportionally to the average nozzle velocity. This is expected as simulations of the burner geometry indicated that flow non-uniformities leaving the burner increase with higher velocity (Carnell, Jr., 2006). Both simulated and measured CH_2O signal profiles for the 10:40 case, Fig. 5.7, exhibit a double peaked structure due to the persistence of formaldehyde at low temperatures outside of the reaction zone coupled with a strong increase in the Boltzmann fraction at lower temperatures. The concentration itself is unimodal, and the peak closest to the burner axial midpoint corresponds to the region of heat release and the actual peak associated with CH_2O production within the flame. As the CH_2O diffuses into the cooler fuel stream (upper nozzles), the temperature dependence of the formaldehyde signal and the higher overall density cause a secondary peak in LIF signal. In the 20:40 case, however, the peak due to the temperature correction is significantly larger than the true signal and overlaps it due to the higher strain, which increases the temperature gradient immediately outside of the reaction zone, as seen in Fig. 5.8.

It is evident that the predicted formaldehyde signal profiles are thinner than the measured signals in both the 10:40 and 20:40 cases. One reason for this may be seen in Fig. 5.9, which shows the

centerline simulated formaldehyde concentration, simulated formaldehyde LIF signal, and calculated Boltzmann fraction as a function of axial location for the 10:40 case. The peak in the Boltzmann fraction correction corresponds with the region in which formaldehyde diffuses into the fuel stream. Although temperature measurements via Raman scattering (Carnell and Renfro, 2007) on the same burner indicated that the simulated temperature profile and peak temperature location are correctly predicted, slight underprediction in the rate of formaldehyde production or its transport properties would be emphasized by the Boltzmann fraction, resulting in an incorrect formaldehyde signal width. The Boltzmann correction itself may also contain errors. The measured formaldehyde profile is also affected by the same spatial resolution issue as the OH profile due to the intensifier used.

The multiplication of the corrected OH and CH_2O signals for the 10:40 and 20:40 cases may be seen in the bottom panels of Figs. 5.3 and 5.4, respectively. This signal overlap approximates CHO formation, which is strongly correlated to heat release rate. Figure 5.10 shows the peak axial reaction rate, normalized by the centerline value, in the radial direction for the 10:40 and 20:40 flames as compared to 2D simulation results. In the 10:40 flame, it increases through the inner nozzle, reaching 130% of the centerline value at a radial location of 10 mm from the centerline. It then increases more rapidly due to the higher strain in the outer nozzle, reaching a peak value of 2.6 times that of the centerline value at a radial location of 15.5 mm from the centerline. At this point, it drops precipitously, falling below 10% of the peak value by approximately 17 mm from the centerline, corresponding to extinction. The 20:40 reaction rate increases more uniformly to a value of 150% of the centerline value by the end of the inner nozzle and a peak of approximately 210% of the centerline value at 14 mm from the centerline, 3

mm earlier than the 10:40 case. It, too, drops precipitously, falling below 10% of the centerline value at a location of approximately 15.5 mm from the centerline.

Due to the issues mentioned, the overlap of the simulated OH and CH_2O signals, seen in the bottom panels of Figs. 5.5 and 5.6, is thinner than that shown in the measurements, although they exhibit similar behavior. The simulated heat release in the 10:40 flame reaches a peak of 165% of the centerline value at a location of 14 mm from the centerline, and falls below 10% of the centerline value by a radial location of 15 mm from the centerline, as seen in Fig. 5.10. In the 20:40 case, the simulated heat release reaches a maximum of 120% of the centerline at a radial location of 13 mm from the centerline, and falls off by a radial location of 14 mm from the centerline.

In order to assess the usefulness of formaldehyde profile as a marker for scalar dissipation, the full width quarter maximum (FWQM) of the measured and simulated formaldehyde signals was calculated, as shown in the top panel of Fig. 5.11. The FWQM was chosen rather than the FWHM due to the half maximum of the 20:40 measured formaldehyde profile width being strongly affected by the double peak nature of the signal. The maximum axial temperatures have been overlaid to better illustrate the location of the edge in each case. The measured formaldehyde width for the 10:40 flame could not be calculated at radial locations less than 11.6 mm due to laser beam width limitations. However, past this point, it drops to a local minimum of 3.0 mm at $r = 14.6$ mm as the formaldehyde profile thins due to the increased strain in the outer nozzle. After this point, it rises due to increased production of formaldehyde in the hot combustion products, reaching a local maxima of 3.5 mm before again decreasing. The 20:40 measured formaldehyde profile is thinner than that of the 10:40 flame due to the higher strain of the inner nozzle, with a width of 3.9 mm at the centerline. Moving radially, the profile width

decreases through the inner nozzle to a value of 3.38 mm at $r = 10$ mm. This is likely due to slight nonuniform velocity profile in the inner nozzle; this decrease closely tracks the velocity profile as predicted from numerical simulations of the burner geometry (Carnell, 2006). It then decreases more rapidly due to the higher strain in the outer nozzle, reaching a local minimum of 3.0 mm at 13.75 mm from the centerline. Post-extinction production of formaldehyde induces a local maximum of 3.65 mm, followed by a decrease.

The bottom panel of Fig. 5.11 shows the simulated scalar dissipation rate along the stoichiometric contour for the 10:40 and 20:40 flames. The scalar dissipation rate is higher in the 20:40 flame, as expected, with a centerline value of 11.6 s^{-1}, as opposed to 5.7 s^{-1} in the 10:40 flame. Both flames exhibit a relatively uniform scalar dissipation rate within the inner nozzle. After approximately 11 mm, where the outer nozzle begins, the scalar dissipation rate rises rapidly in each case, peaking at a radial location of approximately 20 mm from the centerline. The 20:40 case shows an interesting dual-peaked structure with a local minima at approximately 14 mm from the centerline, and the 10:40 case shows a small irregularity as well. This is due to the fact that the thermal diffusivity decreases rapidly through the extinction zone.

Kyritsis *et al.* (2004) showed that in standard counterflow flames with various strain rates, the scalar dissipation rate and the formaldehyde profile width display a relationship of approximately $w \propto \chi^{-0.5}$. In Fig. 5.12, the FWHM formaldehyde width, chosen to match the previous work, has been plotted against the natural logarithm of the scalar dissipation rate for the 10:40 and 20:40 flames. Near the centerline, at low scalar dissipation rates, a relationship between the formaldehyde widths and scalar dissipation rates is clear for all three cases. However, as the scalar dissipation rate continues to increase, both cases depart abruptly from this relationship as the formaldehyde width increases due to secondary production in the hot products following

extinction. The point at which the relationship diverges corresponds to a temperature of approximately 1400 K in both flames, at which point the peak simulated heat release rate has dropped to less than 10% of its centerline value. CO oxidation via CO+OH→CO_2+H, identified as an important reaction in methane oxidation, is negligible at a temperature of 1200 K in these flames, past the point where the formaldehyde-scalar dissipation rate relationship diverges; nonetheless, this relationship is valid through the early stages of extinction and still would provide useful information about the local strain field. Confining the analysis to the region prior to the deviation reveals a strong relationship with a fit of approximately $w \propto \chi^{-0.45}$, also shown in Fig. 5.12. This matches the predicted relationship of $w \propto \chi^{-0.5}$ well, with only 10% error. Formaldehyde fluorescence profile width appears to be a suitable marker of the local scalar dissipation rate in regions where formaldehyde is produced within a vigorously burning flame and within the initial stages of extinction. After extinction, the temperature rapidly decreases and formaldehyde production increases due to incomplete combustion in the hot product stream. Simultaneously, the Boltzmann fraction increases, causing a significant increase in the fluorescence signal, as seen in Fig. 5.12, where the normalized maximum axial formaldehyde signal in the 10:40 case is shown as a function of the local scalar dissipation rate. The formaldehyde signal shows a gradual increase through the flame region, followed by a marked upturn past the point of extinction, as determined by T_{ext} and marked by a vertical line. Thus, the formaldehyde fluorescence intensity can be used in the presence of a local extinction to identify the location of the extinction event and the profile width can be used in the low fluorescence signal region to identify scalar dissipation rate immediately preceding extinction.

These results show that measurements of formaldehyde can be used to identify points of local extinction based on large increases in signal and that the width normal to the flame upstream of

this signal increase can be used to assess the local scalar dissipation rate. The measurements could be applied in turbulent flames to examine the statistical relationships between local extinction and scalar dissipation. Some challenges exist in applying this technique to turbulent flames where the extinction point will be transient. However, formaldehyde fluorescence is still an attractive approach for assessing the conditions near extinction since it produces a strong signal in the presence of a local extinction point, as demonstrated here, and is considerably simpler than other approaches for estimating the scalar dissipation rate. Although this work utilized long on-chip averages since the flame was stable, single-shot, spatially- and temporally-resolved formaldehyde PLIF is straight-forward, as demonstrated by Li *et al*. (2010). High-speed formaldehyde fluorescence could also be used, such as in (Fujita *et al.*, 1995, Olofsson *et al.*, 2005), although this is not necessary to assess the formaldehyde width and gradient at the point of extinction for extracting statistical relationships. Additional diagnostic techniques such as PIV or OH formaldehyde could be used to better quantify the location of the flame edge, as well as determine the surface normal direction. As with any planar diagnostic, out-of-plane contributions to the formaldehyde width in a turbulent flame could impact the interpretation of the results. In addition to turbulent flames, this diagnostic could be applied easily to any number of canonical laminar burners with a local extinction event, such as those of Amantini *et al*. (2005), Lee *et al.* (2010), and Yang *et al.* (2009). Future work will apply the current formaldehyde fluorescence technique to study local extinction in turbulent flames in a burner presented in (Schneider, 2014).

5.6 Figures

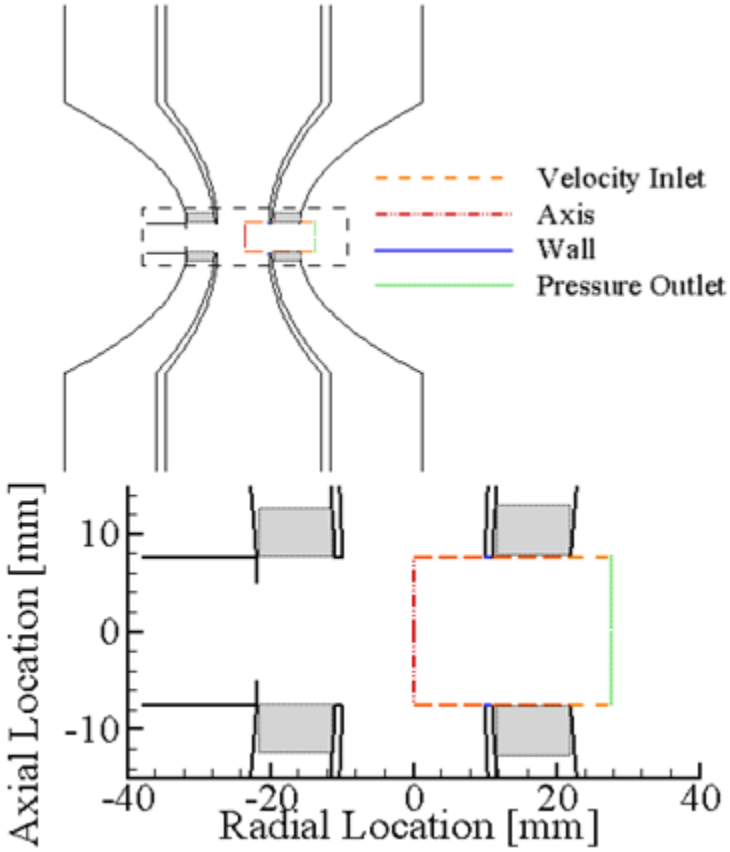

Figure 5.1: Burner geometry for experiments (top) and numerical simulations (bottom).

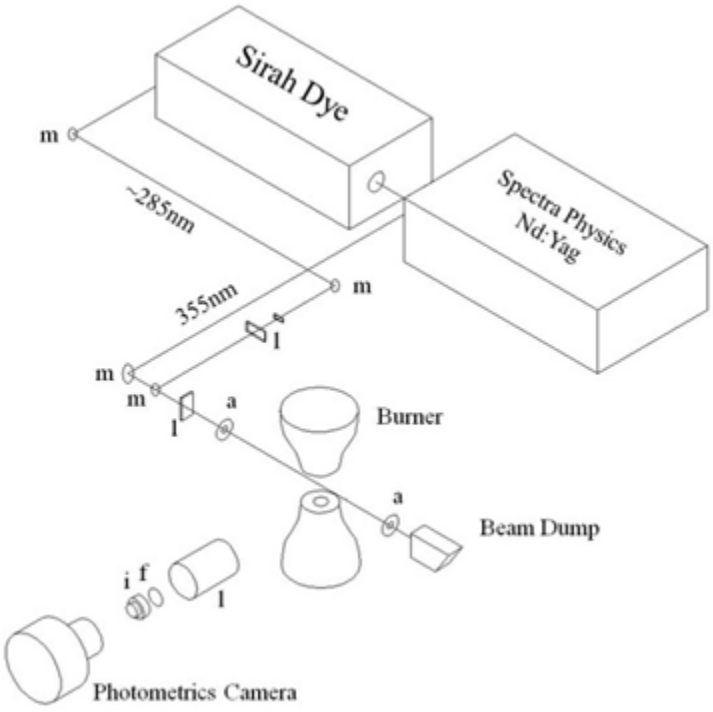

Figure 5.2: Experimental setup, including mirrors (m), lenses (l), apertures (a), filter (f), and image intensifier (i).

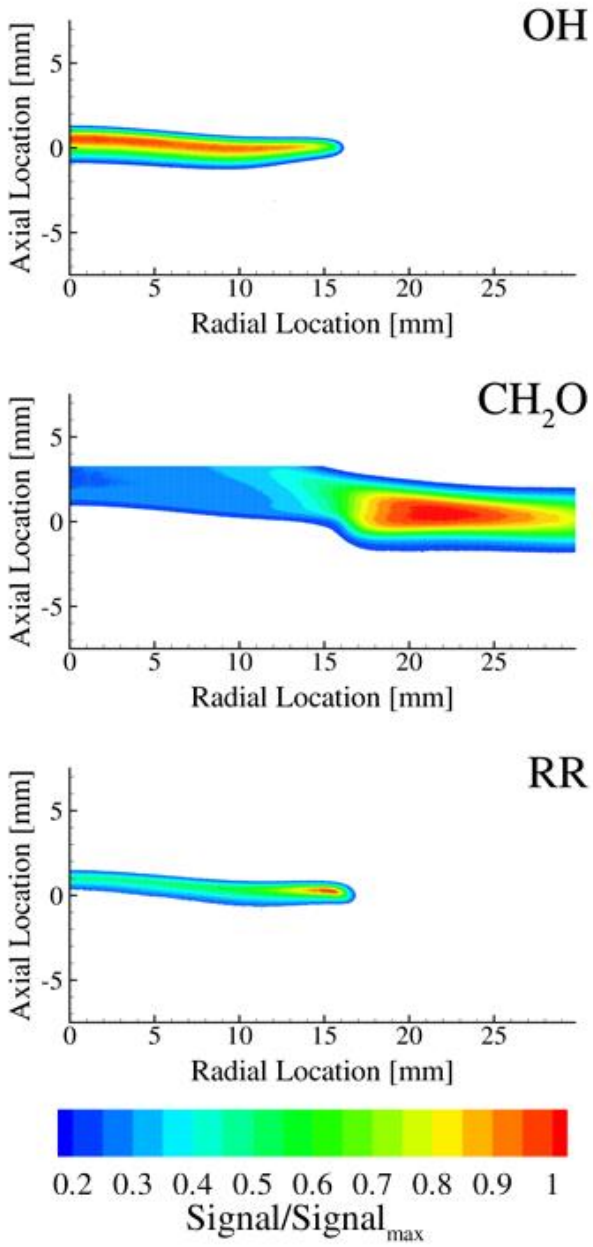

Figure 5.3: Measured, normalized OH fluorescence, CH_2O fluorescence, and reaction rate signals for the 10:40 case. The measurements were corrected for beam profile distribution and the forward reaction rate is estimated from the multiplication of the fluorescence signals.

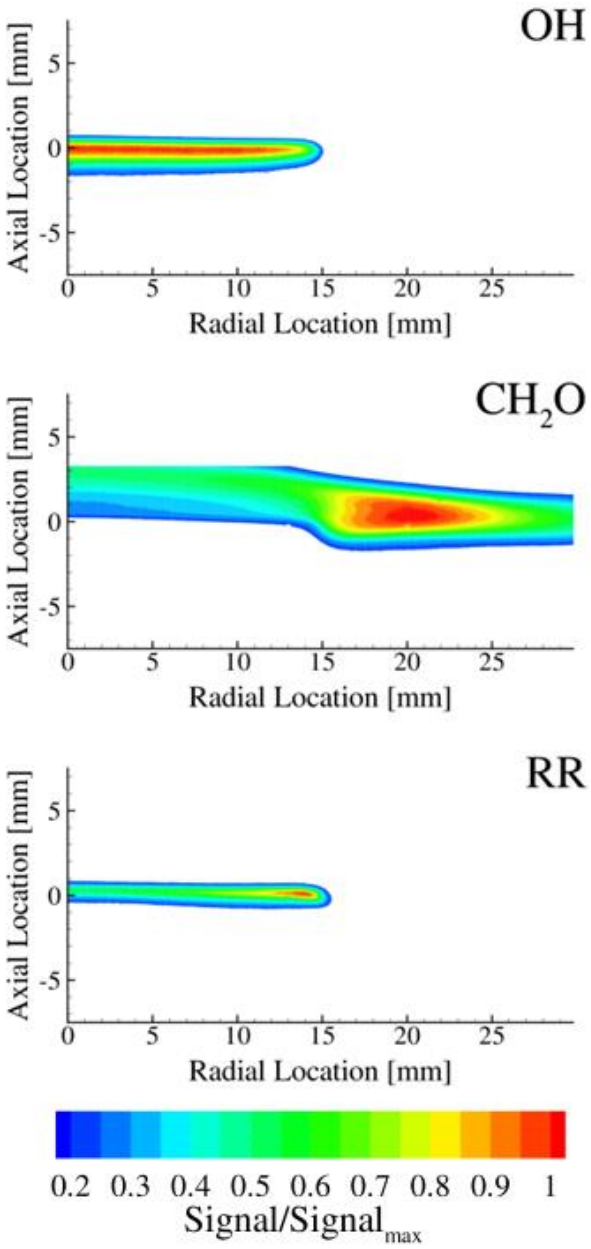

Figure 5.4: Measured, normalized OH fluorescence, CH_2O fluorescence, and reaction rate signals for the 20:40 case. The measurements were corrected for beam profile distribution and the forward reaction rate is estimated from the multiplication of the fluorescence signals.

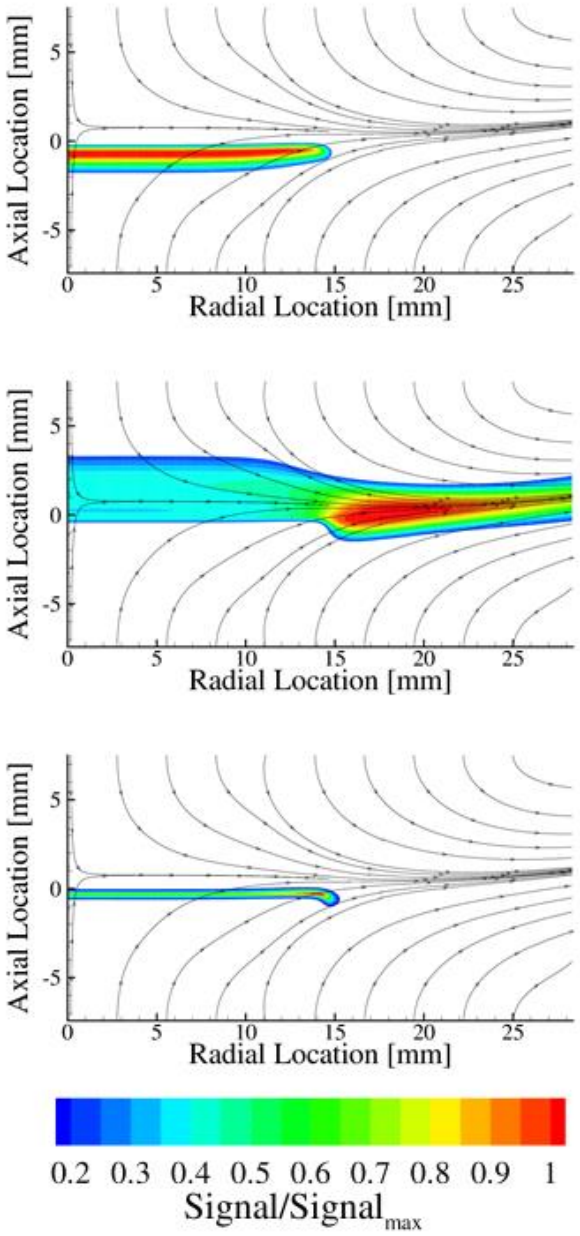

Figure 5.5: Simulated, normalized OH fluorescence, CH_2O fluorescence, and reaction rate signals for the 10:40 case with velocity streamlines. The effects of Boltzmann fraction variations were included, and the OH field includes predicted quenching rates.

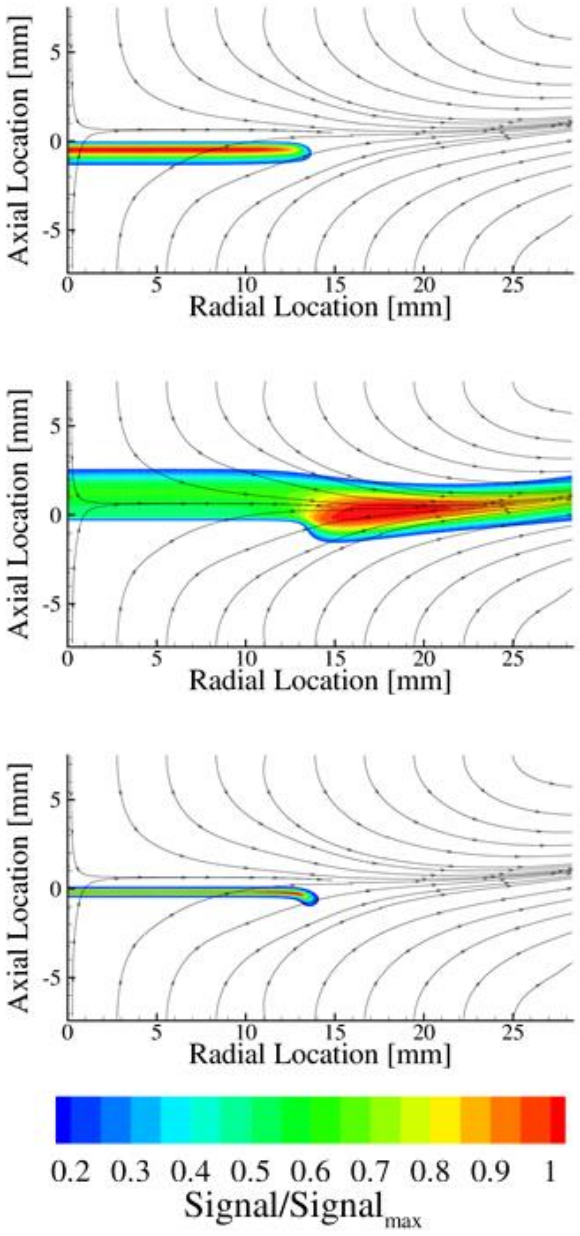

Figure 5.6: Simulated, normalized OH fluorescence, CH_2O fluorescence, and reaction rate signals for the 20:40 case with velocity streamlines. The effects of Boltzmann fraction variations were included, and the OH field includes predicted quenching rates.

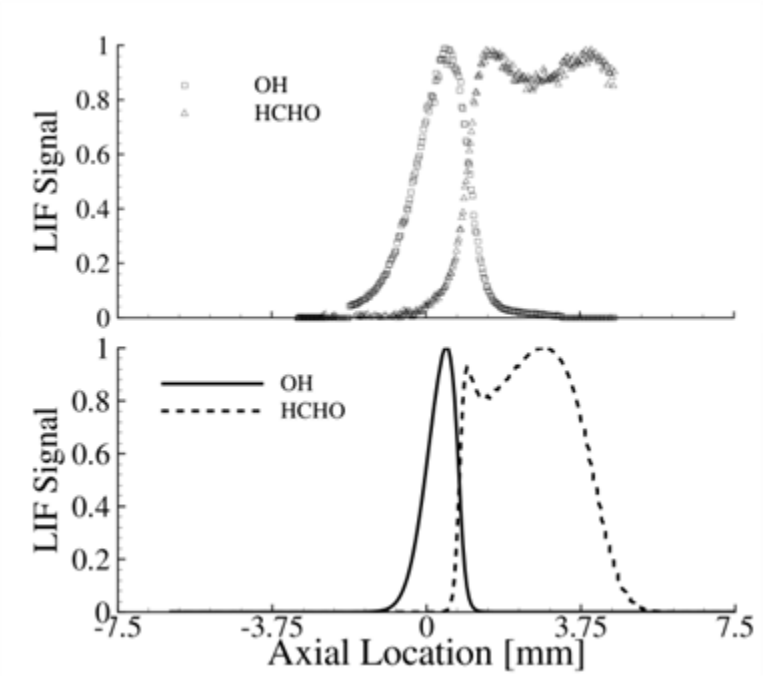

Figure 5.7: Comparison of measured OH and CH_2O fluorescence signals (top panel) with predictions from 2-D simulations (bottom panel) on the burner centerline for the 10:40 case.

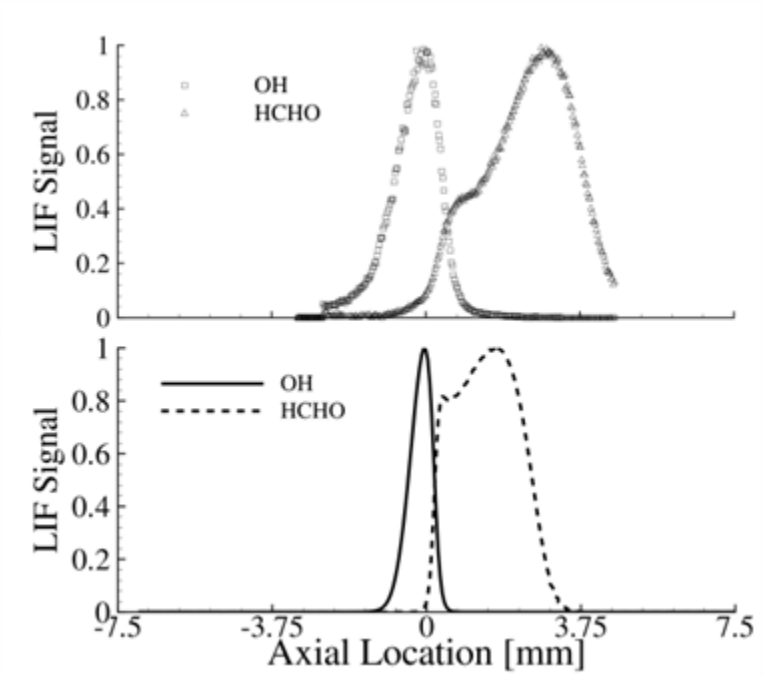

Figure 5.8: Comparison of measured OH and CH_2O fluorescence signals (top panel) with predictions from 2-D simulations (bottom panel) on the burner centerline for the 20:40 case.

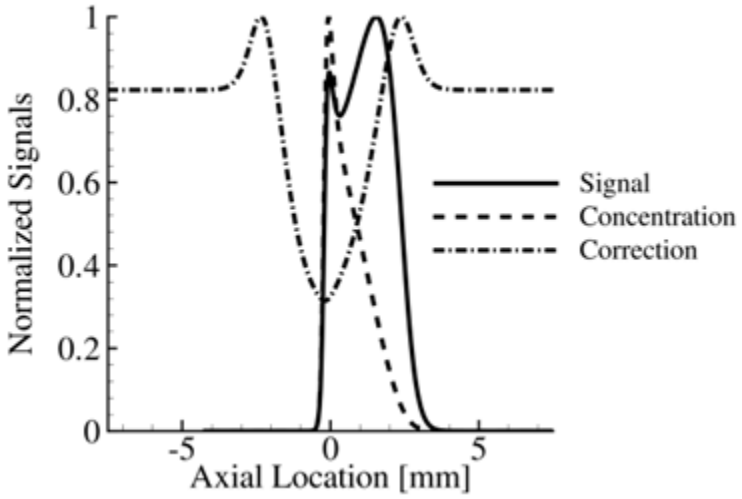

Figure 5.9: Simulated formaldehyde concentration, simulated formaldehyde fluorescence, and Boltzmann correction (all normalized) as a function of axial location along the burner centerline.

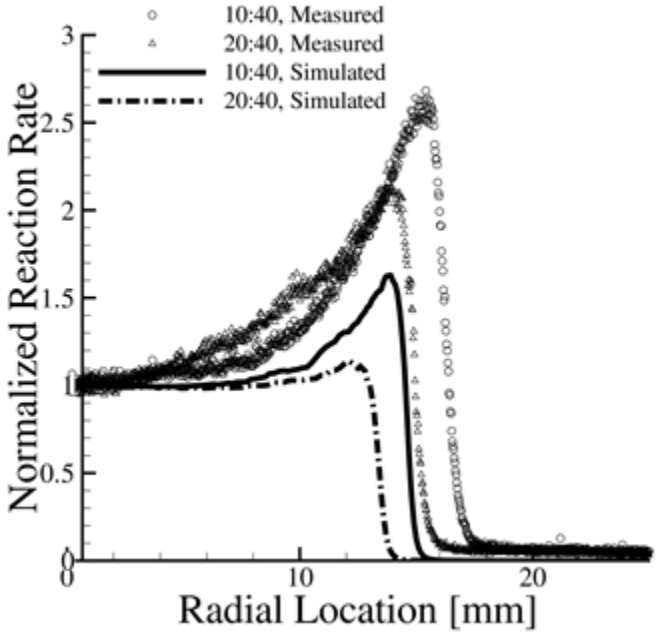

Figure 5.10: Peak axial reaction rate, normalized by the centerline value, in the radial direction for the 10:40 and 20:40 flames as compared to 2D simulation results.

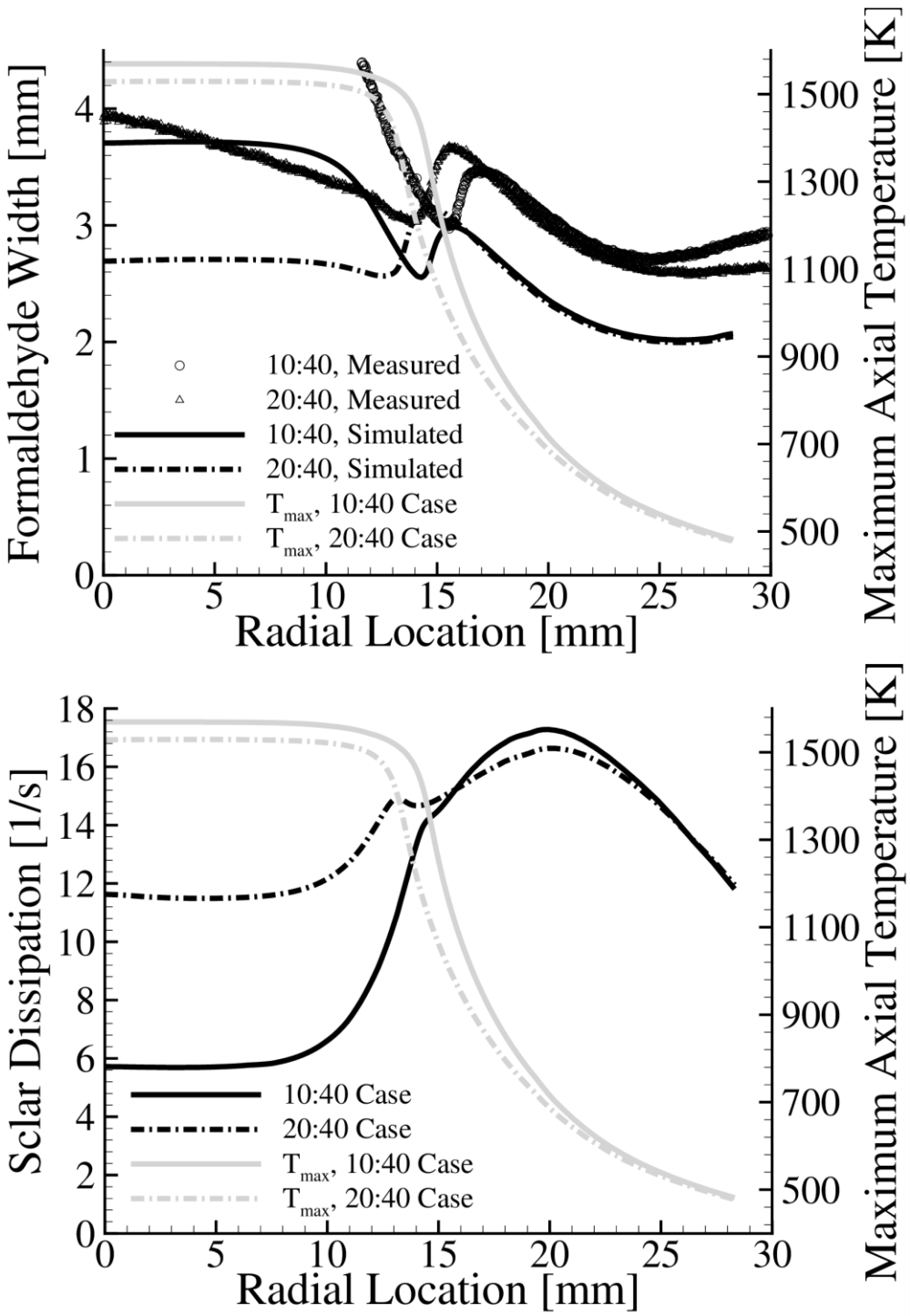

Figure 5.11: Measured and simulated formaldehyde layer width (FWQM) as a function of radial location (top panel) and simulated scalar dissipation rate along the stoichiometric contour (bottom panel), with overlaid peak temperature profiles.

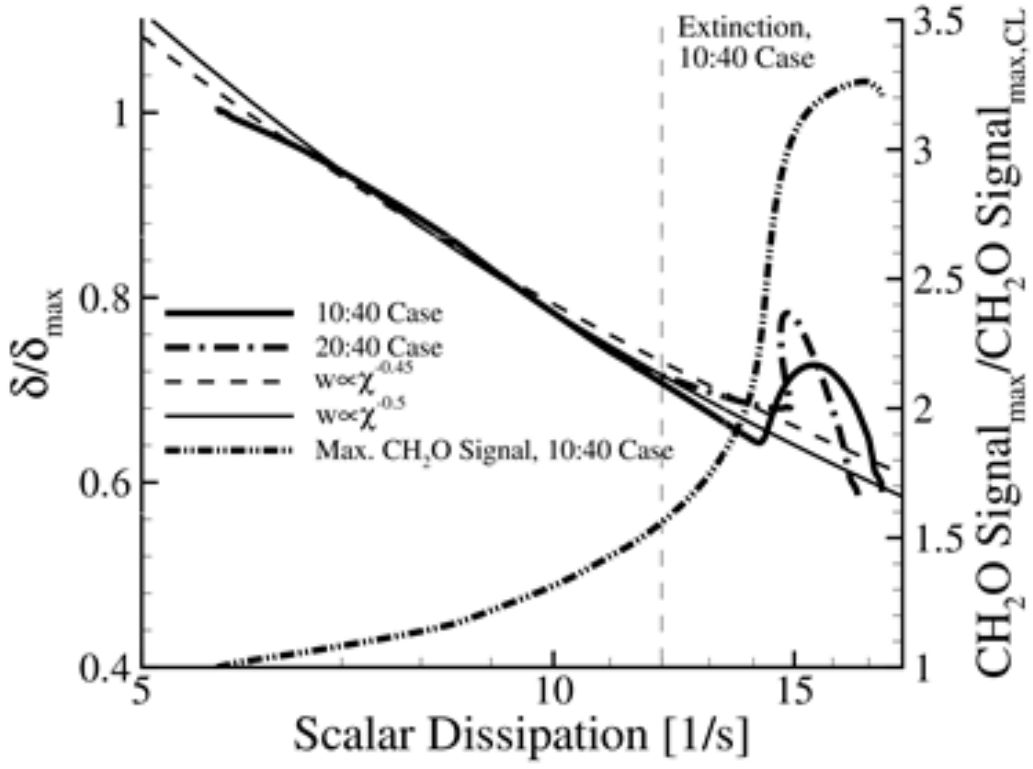

Figure 5.12: Simulated formaldehyde layer width (w, FWHM) for the 10:40 and 20:40 cases and maximum formaldehyde fluorescence signal for the 10:40 case as a function of scalar dissipation rate (χ).

6. Analysis of Scalar Dissipation Rate and Heat Transfer in a Negative Edge Flame

6.1 Background and Motivation

In the laminar flamelet model, extinction is modeled as a one-dimensional balance between heat release and scalar dissipation. Depending on the particular execution of the model, extinction occurs at a critical reaction rate (Spalding, 1953), scalar dissipation rate (Peters, 1988), or Damköhler number (T'ien, 1975). Previous work by Carnell and Renfro (2006) demonstrated that a simulated negative edge flame stabilized off-axis in a modified counterflow burner exhibits scalar dissipation rates higher than those predicted by centerline extinction simulations. This is due to advection through the extinction edge, which acts as an energy gain due to the alignment of the velocity field and the temperature gradient. However, the relationship between advection and extinction scalar dissipation rate was too complex to quantify. Additionally, a generalized understanding of the impact of thermal and molecular diffusivity could not be determined, as this analysis was only performed on methane flames. A previous extension of this work to negative edges in ethane and hydrogen counterflow diffusion flames (Gosselin *et al.*, 2013b) showed that the impact of advection was enhanced for these fuels, particularly hydrogen, but the specific reasons for this were not examined. Several groups have shown that reactant leakage in flames with non-unity Lewis numbers can significantly alter the reaction region, either strengthening or weakening the flame (Chung and Law, 1983, Kim and Williams, 1997, Wang *et al.*, 2007).

6.2 Specific Objectives

The current work extends the efforts of Carnell and Renfro (2006) with further energy analysis, with special attention paid to the laminar flamelet model understanding of extinction, particularly with respect to reactant leakage in non-unity Lewis number fuels. It has also been extended to two additional fuels, ethane and hydrogen, in order to analyze the impact of molecular and thermal diffusivity. This work will attempt to

1. Better understand impact of advection on extinction in negative edge flames.
2. Offer a phenomenological description of the deviation of negative edge flames from the 1-D laminar flamelet model.
3. Examine the effects of reactant leakage on extinction in the presence of a negative flame edge.

6.3 Numerical Methods

The burner studied numerically consisted of the same modified counterflow burner described in Section 5.3, which was previously characterized by Carnell and Renfro (2005). The axisymmetric computational domain used in this work is shown in Fig. 6.1 in relation to a schematic of the experimental burner. A burner separation of 15 mm was used, and the burner nozzles were modeled as velocity inlets with uniform velocity and species profiles. The velocity inlets and the walls representing the lip of the cooling jacket and the small section of wall between the inner and outer nozzles were fixed at a temperature of 300 K. The cooling jacket

forms a lip of 2.5 mm above the nozzle, and it extends 14 mm beyond the outer nozzle. The outflow was modeled as a constant pressure outlet.

The resolution of the mesh was divided into three regions: first, a coarse mesh with a resolution of 250 μm for the cool, non-reacting flow near the nozzles, then a second mesh with a resolution of 125 μm, centered around the physical midpoint of the burner, and finally a fine resolution mesh with a resolution of 62.5 μm, centered around the heat release zone, which varied based on the fuel used.

A steady, segregated, axisymmetric, implicit solver (Fluent v. 14.0) was utilized for the numerical simulations. One-step reaction models were used; the rate exponents and pre-exponential factors used for each fuel are shown in Table 6.1, along with the activation energies used to calculate the reaction rate. One-step models are not expected to quantitatively predict extinction behavior, since they are known to under-predict parameters such as flame speed in certain conditions (Westbrook and Dryer, 1981); however, one-step chemistry should sufficiently capture the trends of interest to this work as shown for methane flames by Carnell and Renfro (2007). Species, momentum, mass conservation, and energy equations were solved via second order upwind discretization. The SIMPLE scheme (semi-implicit method for pressure linked equation (Patankar and Spalding, 1972, Caretto *et al.*, 1973)) was utilized, as well as PRESTO! (PREssure Staggering Option (Patankar, 1980)) to determine the pressure/velocity field.

The ideal gas model is used for the fluid mixture, which allows the thermal conductivity, λ, the mixture viscosity, ν, and the mixture specific heat, c_p, to be determined via ideal gas mixing laws from individual species' properties. Kinetic theory was used to calculate the individual

species' conductivity and viscosity. Lennard-Jones characteristic lengths and energy parameters were taken from the Gas Research Institute (GRI) transport database (Smith et al.).

Full multicomponent diffusion was enabled, which means that the diffusive mass flux vector for each species i, $\vec{J_i}$, was obtained by solving the Maxwell-Stefan equations. This gives the generalized Fick's law diffusion coefficients (Taylor and Krishna, 1993), D_{ij}, which in turn are dependent upon the binary mass diffusion coefficients, calculated via a modified Chapman-Enskog formula (McGee, 1991). An empirically based composition-dependent equation derived from (Kuo, 1986) was used to model the thermal diffusion coefficient, $D_{T,i}$.

Buoyancy effects were not included, as they were shown to be negligible in a previous study (Carnell, Jr. and Renfro, 2005), and pressure work, kinetic energy, and viscous dissipation terms were not included in the energy equation for simplicity. Case convergence was determined via a change of less than 0.001 K in peak centerline temperature over 1000 iterations. This resulted in scaled residuals of less than 1×10^{-7} and 1×10^{-4} for energy and continuity equations, respectively.

For the following analysis, simulations were performed at a wide variety of boundary conditions; however, for simplicity, some results such as energy balance analysis are presented for only a single case for each fuel, the boundary conditions of which are shown in Table 6.2. Mixture fraction and scalar dissipation rate were calculated as described in Section 2.3, and the stoichiometric mixture fraction is also listed in Table 6.2. A cubic interpolation scheme was used to calculate all values along the maximum temperature contour, and the error in the post-processed energy equation was less than 1% of peak heat release for all cases.

6.4 Results and Discussion

Simulated temperature contours with overlaid velocity contours for a stable flame with a negative extinction edge for each of the three fuels are shown in Fig. 6.2. The boundary conditions for these flames are listed in Table 6.2. In each case, fuel diluted in nitrogen flows from the bottom of the domain, while air flows from the top, and the left boundary is the axis of symmetry. The outflow region of the burner, including the lip of the cooling jacket, has been excluded from these images, although it was included in the simulations. In each case, a flame stabilizes within the inner nozzle, similar to a standard counterflow diffusion flame. The peak temperature in this region is relatively constant. The methane and ethane flames sit slightly to the air side of the stagnation plane, while the hydrogen flame sits slightly to the fuel side. However, increased strain in the outer nozzle "squeezes" the flame, eventually causing extinction in all three cases. It is clear from the overlaid streamlines that the velocity through the extinction edge is predominantly in the radial direction, meaning that it is fed by hot products from the flame itself and is therefore a negative edge. Methane exhibits the earliest extinction with respect to radial location, while hydrogen exhibits the latest.

Although results for ethane have been shown in Fig. 6.2, these simulations exhibited extreme stability. In order to achieve stability and convergence, the thermal conductivity and viscosity were both set to constants ($\lambda = 0.0454$ W/m·K, $\mu = 1.72 \times 10^{-5}$ kg/m·s). The reasons for this instability may be related to the relative molecular and thermal diffusivities, shown in Table 6.3 for all three fuels. The thermal diffusivity has been taken from the fuel stream of the Fluent simulations (that is, the combined thermal diffusivity of the fuel and nitrogen dilution), and the mass diffusivity listed is that for the fuel in question in nitrogen, as calculated from the modified

Chapman-Enskog formula (McGee, 1991). The Lewis numbers calculated from these values are also given; methane has a Lewis number close to unity, while hydrogen is less than unity, and ethane is significantly greater than unity. The previous work of Kim and Williams (1997) indicated that counterflow diffusion flames of fuels with Lewis numbers greater than unity will be less stable. The instability of ethane flames in the current work seems to support this theory; however, for the remaining results in this chapter, ethane will be excluded, as the simulations are not expected to accurately capture the heat transfer behavior through the extinction edge. Ethane – and fuels with Lewis numbers greater than unity in general – requires further study.

In order to assess the impact of advection on the extinction process, centerline extinction simulation studies were performed in addition to the negative edge flame simulations. In these cases, a standard counterflow flame was simulated, with identical velocities and fueling in the inner and outer nozzles. This velocity was increased in increments of 0.1 cm/s until the flame extinguished. The characteristics of the last stable flame before extinction represent the extinction criterion in the absence of advection. For example, the scalar dissipation rate immediately before extinction will be referred to as the 1-D extinction scalar dissipation rate, or $\chi_{ext,1-D}$. Previous work by Carnell and Renfro (Carnell, Jr. and Renfro, 2006) showed that advection through the negative edge of a methane flame allowed it to reach scalar dissipation rates higher than those predicted by centerline extinction studies.

In the previous study of methane flames, the steady energy equation

$$0 = -\rho c_p \left(V_r \frac{\partial T}{\partial r} + V_a \frac{\partial T}{\partial a} \right) + \lambda \left(\frac{\partial^2 T}{\partial r^2} + \frac{\partial^2 T}{\partial a^2} + \frac{1}{r} \frac{\partial T}{\partial r} \right) + \frac{\partial \lambda}{\partial r} \frac{dT}{dr} + \frac{\partial \lambda}{\partial a} \frac{\partial T}{\partial a} - \sum_i \nabla h_i \cdot \vec{J_i} + \dot{\omega}''' \Delta h \qquad (6.1)$$

was calculated along the contour of stoichiometric mixture fraction. The previous work (Carnell, Jr. and Renfro, 2006) established that several terms in Eqn. (6.1) were negligible. First, the

effects of energy transport by species diffusion, $\sum_i \nabla h_i \cdot \vec{J_i}$, are negligible in comparison to local velocities. Additionally, the term arising from radial geometry, $\lambda/r\,\partial T/\partial r$ is negligible, which indicates that the behavior of this edge flame is not affected by the burner geometry. That is, a flame formed in a straight burner under the same flow conditions would behave identically. The effects of variable thermal conductivity, $\partial\lambda/\partial r\,\partial T/\partial r$ and $\partial\lambda/\partial a\,\partial T/\partial a$, are also negligible. Axial advection, $-\rho c_p V_a\,\partial T/\partial a$ was shown in both previous work and in the current work to have little effect until after extinction, largely due to the proximity of the peak reaction rate to the peak axial temperature. This leaves the simplified energy equation

$$0 = \lambda\frac{\partial^2 T}{\partial a^2} + \lambda\frac{\partial^2 T}{\partial r^2} + \dot{\omega}'''\Delta h - \rho c_p V_r\frac{\partial T}{\partial r} \tag{6.2}$$

Although the previous analysis is useful for establishing the relationship between advection and excess scalar dissipation rate, Eqn. (6.1) does not explicitly include scalar dissipation rate, making it difficult to directly assess this relationship directly. To that end, the typical 1-D laminar flamelet model, informed by the approach of Liñán (1974), was extended to two dimensions by performing a coordinate transformation on temperature, from $T(a,r)$ to $T(Z,r)$, and analyzing the various terms along the maximum temperature contour. The significant terms resulting from this analysis are given in

$$0 = \frac{\partial^2 T}{\partial z^2}\rho c_p\chi + \dot{\omega}'''\Delta h\ - \rho c_p V_r\frac{\partial T}{\partial r} \tag{6.3}$$

These three terms have been plotted along the peak temperature contour in Fig. 6.3. In each case, a steady flame forms within the inner nozzle, where heat loss from axial diffusion is almost

perfectly balanced by heat release. As strain increases in the outer nozzle, heat loss to axial diffusion increases. Initially, the reaction rate also increases to counterbalance this; however, it eventually reaches a maximum and begins to decline as the temperature in the flame drops. As the temperature drops off, this causes advection through the edge to increase; this is a gain in the flame edge because the local velocity is aligned with the negative temperature gradient. Eventually, the reaction rate drops to zero as the flame extinguishes altogether.

Figure 6.4 shows the peak temperature as a function of local scalar dissipation rate for 1-D extinction (solid line) and a negative edge flame (dotted line) for both methane and ethane. In both cases, the peak temperature drops off more quickly in the 1-D extinction case than in the negative edge case, likely due to the impact of advection. However, it is obvious that this effect is much stronger in the case of hydrogen. Also marked on this figure are several flame conditions. First, a location "Far From Extinction" refers to the centerline location of the negative edge flame, and will be used for subsequent discussion. Also noted are the scalar dissipation rate at 1-D extinction, $\chi_{ext,1-D}$, and the peak temperature immediately prior to 1-D extinction, T_{ext}. For the purpose of consistency in this work, extinction in the negative edge cases will be referred to as the location on the peak temperature profile where $T_{max} = T_{ext}$. The scalar dissipation at this location will be referred to at the extinction scalar dissipation rate, χ_{ext}, and the difference between this value and the 1-D extinction value will be referred to as excess scalar dissipation rate.

In order to assess the specific impact of advection, the normalized excess scalar dissipation rate ($\chi_{excess}/\chi_{ext,1-D}$) has been plotted against the local magnitude of advection, $-\rho c_p V_r \frac{\partial T}{\partial r}$, for a number of negative edge flame cases for both hydrogen and methane. Methane experiences small

values of excess scalar dissipation rate, on the order of 5%, and they are generally proportional to the local advection. However, hydrogen experiences significantly higher values of excess scalar dissipation rate, ranging from 40% to 100% over the 1-D extinction scalar dissipation rate. The excess scalar dissipation rate appears to be linearly proportional to advection. The outsize impact of advection in methane flames cannot be explained in terms of relative energy magnitudes; that is, advection does not account for a significantly larger portion of the energy budget in hydrogen flames, as can be seen in Fig. 6.3. At extinction, the advection and heat release terms are of approximately the same magnitude in both fuels.

In order to uncover the reasons for the resiliency of hydrogen negative edge flames, methane and hydrogen flames (one case each) have been studied at the three conditions indicated in Fig. 6.4: far from extinction, at $\chi = \chi_{ext,1-D}$, and at $T_{max} = T_{ext}$. At each condition, axial profiles of reaction rate, temperature, and the product of fuel and oxidizer concentrations have been plotted as a function of local mixture fraction for both 1-D extinction and negative edge extinction. These results are shown in Figs. 6.6, 6.7, and 6.8. The location of peak temperature in each case is indicated with a dotted vertical line.

Far from extinction, Fig. 6.6, the 1-D extinction and negative edge cases match very closely. In the case of methane, the overlap of fuel and oxidizer is unimodal, and the location of peak temperature occurs on the air side of the flame. In hydrogen, the overlap of fuel and oxidizer is bimodal, due to incomplete combustion, which promotes leakage of fuel past the flame.

At the point where the scalar dissipation rate is equal to that of 1-D extinction, Fig. 6.7, the negative edge case departs from the 1-D case. Due to advection, the peak temperature in each case has increased – slightly in the case of methane, more significantly in the case of hydrogen.

Along with it, reaction rate has increased. The increase in scalar dissipation rate promotes the reaction rate as well. In both cases, the increase in reaction rate consumes the reactants more rapidly, decreasing leakage past the flame, as seen in the bottom panels. In the case of hydrogen, the location of peak temperature and thus reaction rate shifts toward the fuel size of the flame due to the enhanced diffusion and consumption of fuel. This figure quite clearly shows why extinction is extended in negative edge flames: although the increased scalar dissipation rate promotes heat loss, it is partially offset due to advection, which allows an increase in heat production due to the locally higher temperatures.

The point where $T_{max} = T_{ext}$, Fig. 6.8, can be fairly called the extinction point for both the 1-D case and the negative edge case. In both cases, the temperature profiles match closely. However, in each, the overlap of fuel and oxidizer at extinction is significantly different in the negative edge case. This is because extinction in the negative edge case occurs at a fundamentally different point, thermodynamically. Heat gain through advection causes the flame extinction to follow a different temperature history, which significantly alters reactant consumption. This is especially true in the case of hydrogen, where the enhanced diffusion of fuel past the flame allows the reaction rate to increase far past the value predicted in 1-D extinction.

This effect may also be seen in Fig. 6.9, which shows the local reaction rate as a function of the local scalar dissipation rate for 1-D extinction (red line) and a variety of negative edge cases (blue lines). One-dimensional extinction is marked with a vertical dotted line for each fuel. First, it should be noted that, as expected, the peak reaction rate for hydrogen occurs at a significantly higher scalar dissipation rate for the negative edge cases as opposed to the centerline case. Methane, on the other hand, shows minimal improvement in the negative edge cases. Also, the peak reaction rate in the hydrogen negative edge flames varies widely and appears to be strongly

correlated with the extinction scalar dissipation rate, while the peak reaction rate for methane and ethane is relatively unchanged for a variety of boundary conditions. This is due to the fact that an increase in scalar dissipation rate increases the reaction rate due to the influx of reactants, but simultaneously increases the heat loss due to axial diffusion. In the case of methane, these effects are approximately balanced, and advection offsets heat loss in the negative edge case only slightly. In hydrogen flames, a Lewis number less than 1 causes a significantly lower heat loss relative to the increase in reaction rate, allowing the local advection to have a greater impact on the extinction behavior.

One consequence of this behavior is that the local scalar dissipation rate is a poor marker for extinction in flames with non-unity Lewis numbers. Kim and Williams (1997) recognized this and proposed an altered Damköhler number which explicitly includes the Lewis number; however, their definition still excludes advection, as it was developed for 1-D asymptotic analysis. Advective heat flux in the negative edge means extinction behavior is path-dependent. Thus, local peak temperature may be a better marker for local extinction of a negative edge flame, as can be seen in Fig. 6.10, in which the reaction rate is plotted against peak temperature for a variety of negative edge cases, as well as 1-D extinction. Although the reaction rate still varies widely in the case of hydrogen, its peak empirically occurs at a relatively consistent temperature. Local temperature changes due to both advection and local molecular diffusion and is therefore path-dependent by default.

Taken together, the results presented here demonstrate that the 1-D laminar flamelet model does not predict extinction well in the presence of a negative edge, particularly in fuels with a non-unity Lewis number. The 1-D extinction criterion significantly overpredicts extinction in the case of hydrogen; however, the peak flame temperature shows promise as a marker for progress

toward extinction when molecular diffusion and advective heat flux are significant. Further study is needed, however, for fuels with a Lewis number larger than unity, as stability issues in the ethane negative edge flames prevented in-depth analysis.

6.5 Tables

Table 6.1: Pertinent one-step mechanism data used in two-dimensional simulations.

Fuel	Mechanism Source	Rate Exponent, Fuel	Rate Exponent, Oxidizer	Pre-Exponential Factor	Activation Energy [J/kmol]
Methane	(Westbrook and Dryer, 1981)	0.2	1.3	2.119×10^{4}	2.027×10^{8}
Ethane	(Westbrook and Dryer, 1981)	0.1	1.65	6.186×10^{9}	1.256×10^{8}
Hydrogen	(ANSYS, 2009)	1	0.5	1.8×10^{13}	1.4644×10^{8}

Table 6.2: Boundary conditions of fuel-side streams for energy analysis.

Fuel	Inner Nozzle Velocity (V_i, cm/s)	Outer Nozzle Velocity (V_o, cm/s)	Mole Fraction of Fuel ($X_i = X_o$)	Mass Fraction of Fuel ($Y_i = Y_o$)	Z_{st}
Methane	18	54	0.200	0.1252	0.318
Ethane	18	54	0.064	0.0726	0.4778
Hydrogen	18	54	0.096	0.0076	0.7947

Table 6.3: Thermal diffusivity, mass diffusivity, and approximate Lewis number for each of the fuel streams.

Fuel	$\boldsymbol{\alpha}$ [m^2/s]	$\boldsymbol{D_{ij}}$ [m^2/s] (ANSYS, 2009)	**Le**
Methane	2.18E-05	2.21E-05	0.99
Ethane	3.65E-05	1.83E-05	2.00
Hydrogen	2.68E-05	5.83E-05	0.46

6.6 Figures

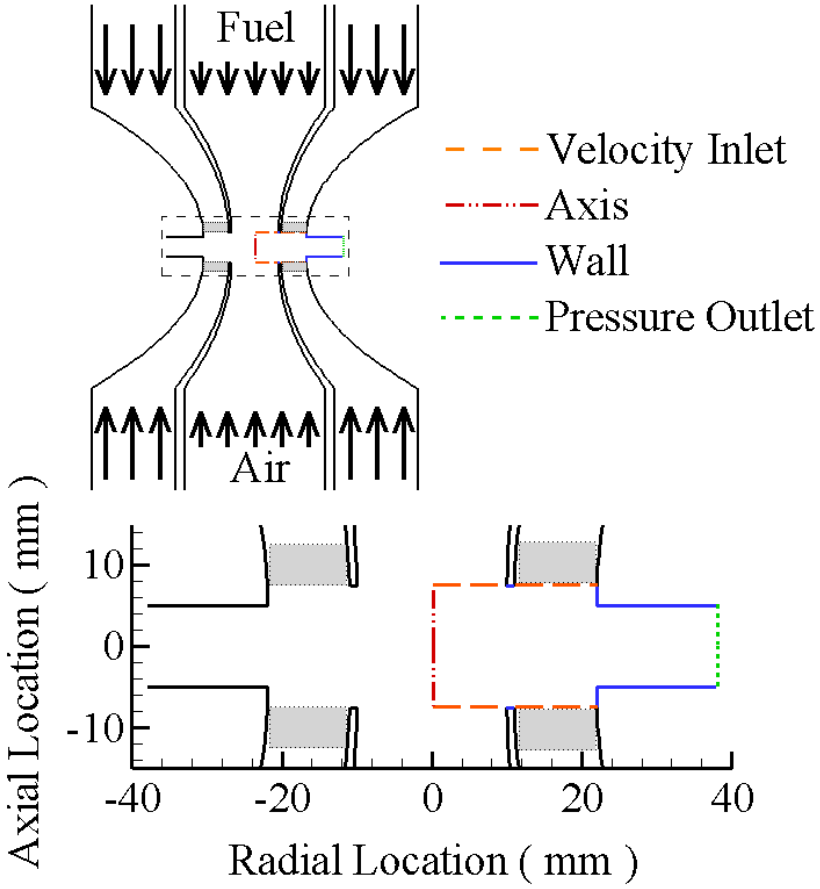

Figure 6.1: Burner geometry and computational domain with boundary conditions indicated.

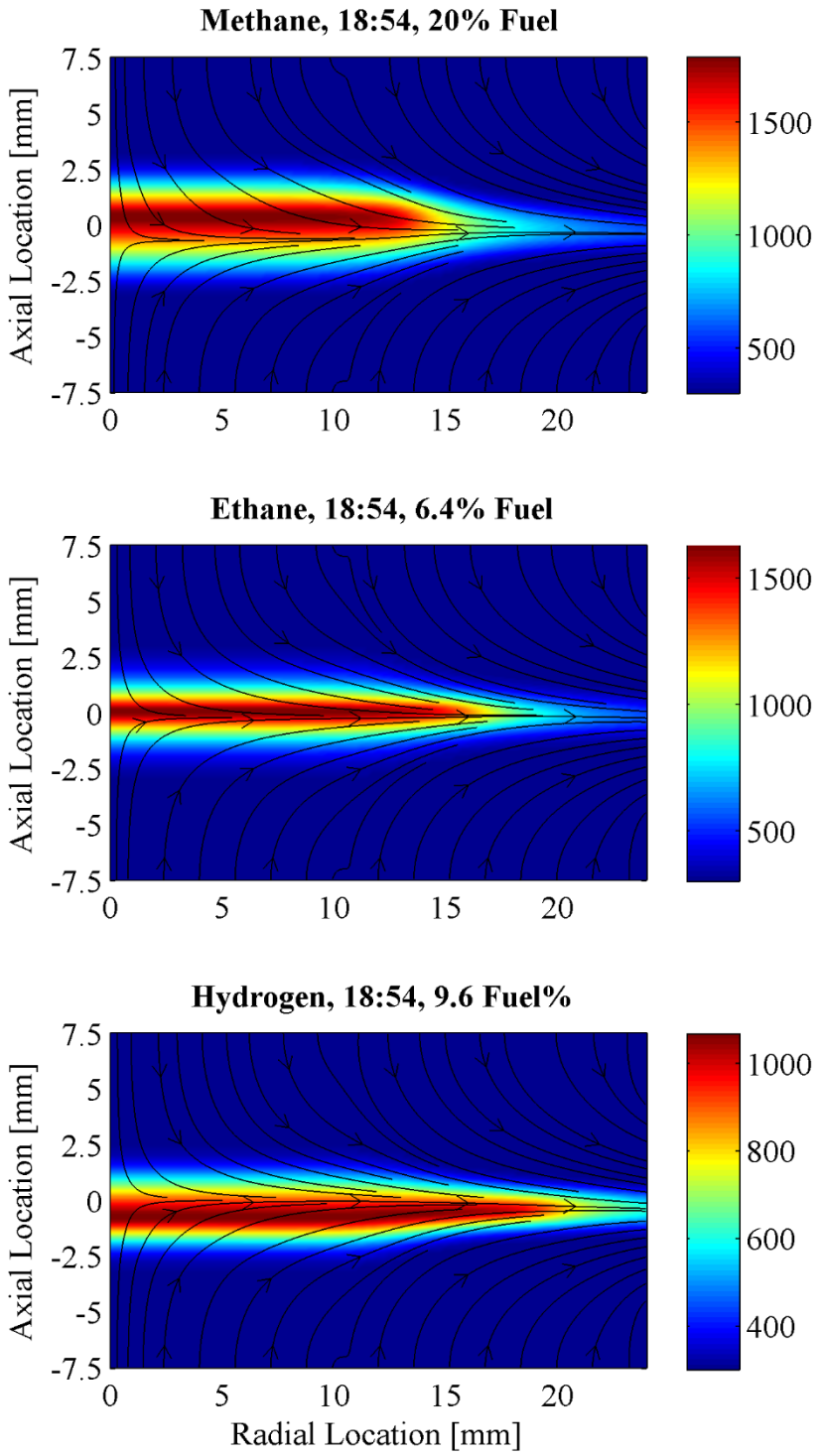

Figure 6.2: Simulated temperature contours [K] with overlaid velocity streamlines for methane (top), ethane (middle), and hydrogen (bottom) negative edge flames.

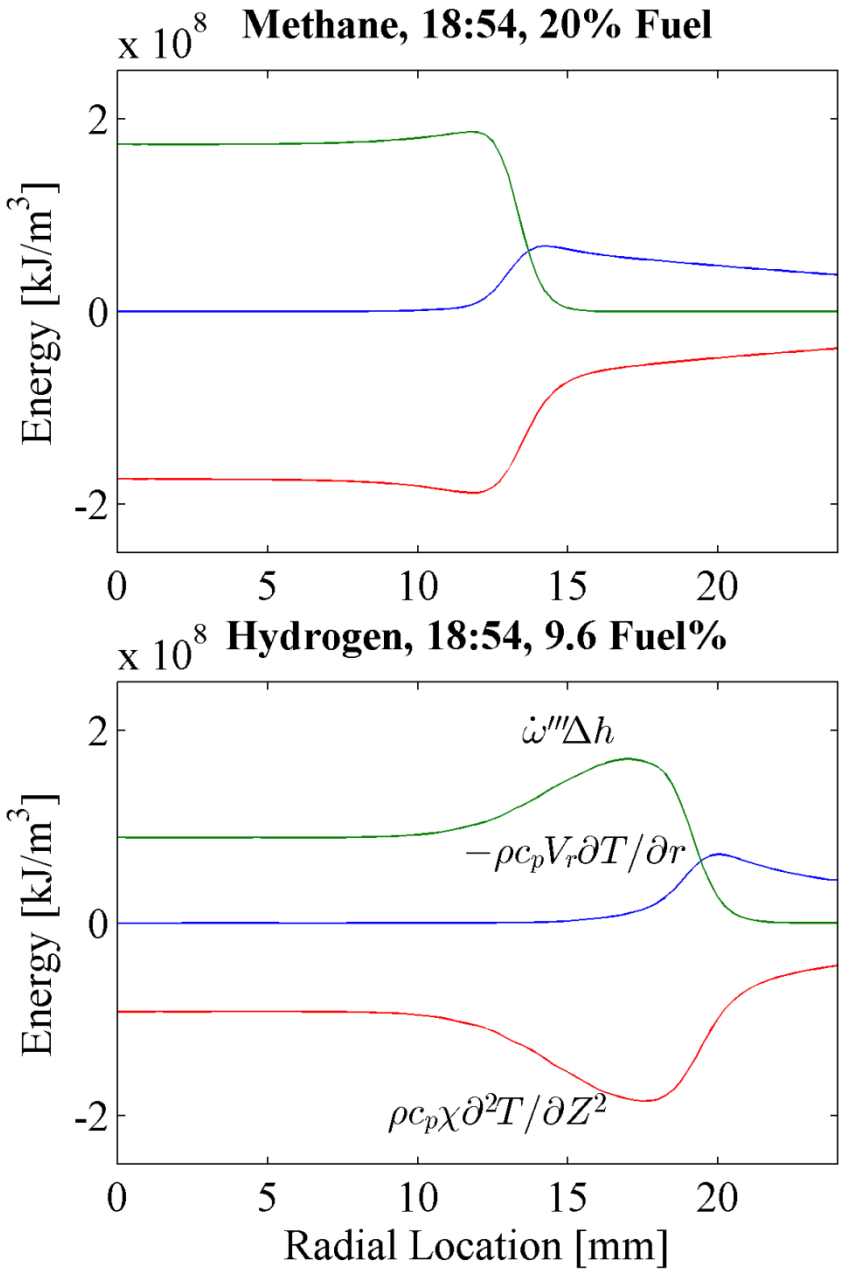

Figure 6.3: Individual transformed energy term variation for methane (top) and hydrogen (bottom) in the radial direction. The analysis has been performed along the maximum temperature contour.

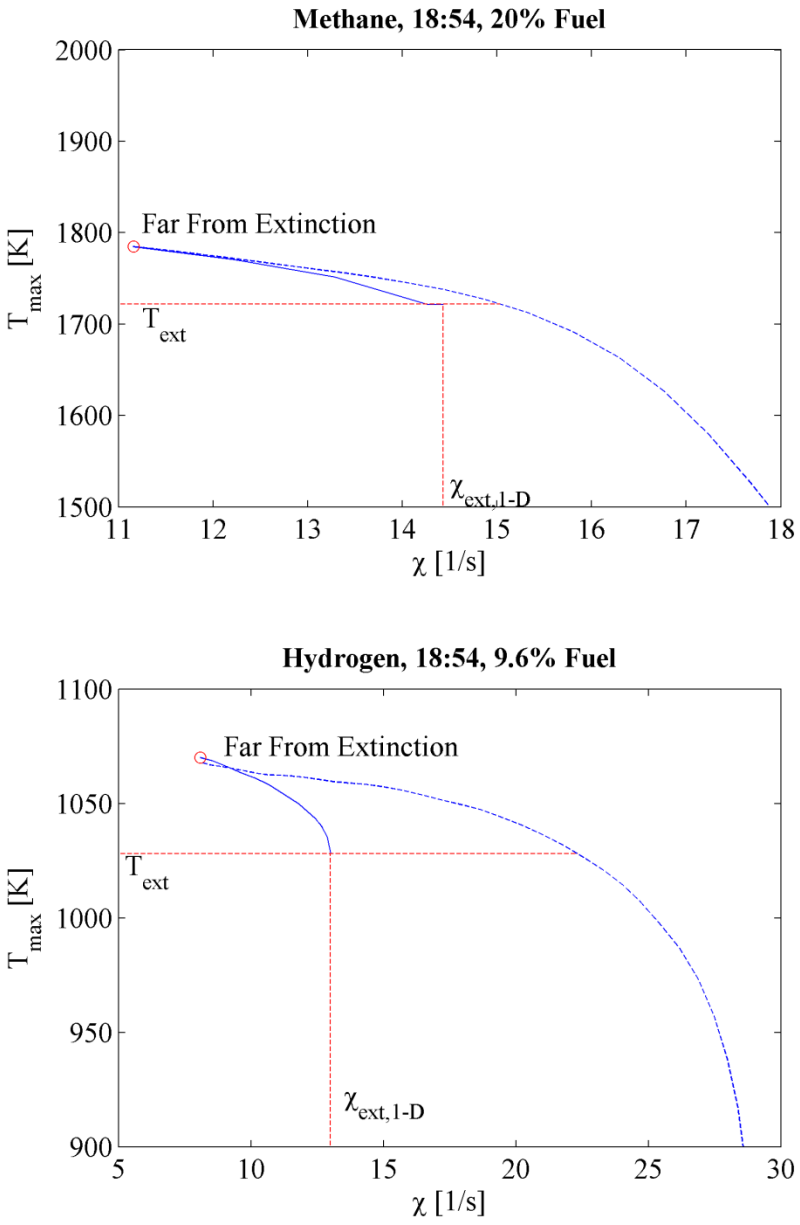

Figure 6.4: The peak temperature profile plotted as a function of corresponding local scalar dissipation rate for methane (top) and hydrogen (bottom). Profiles for centerline extinction (solid line) and a negative edge flame (dotted line) are both shown, and several flame conditions of interest are indicated.

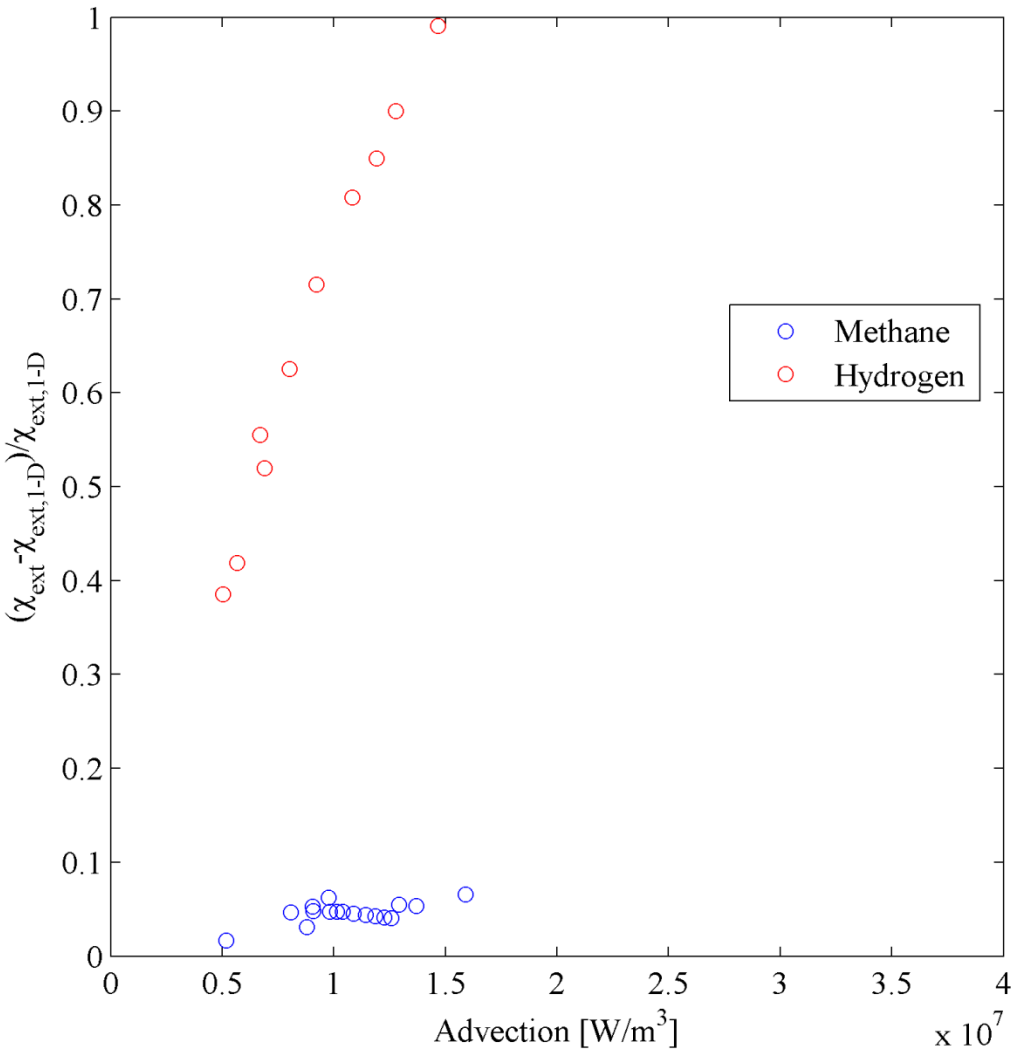

Figure 6.5: Excess scalar dissipation rate at the negative edge along the peak temperature contour as a function of advection through the edge at the location corresponding to the 1-D extinction temperature, for a variety of cases for both methane and hydrogen flames.

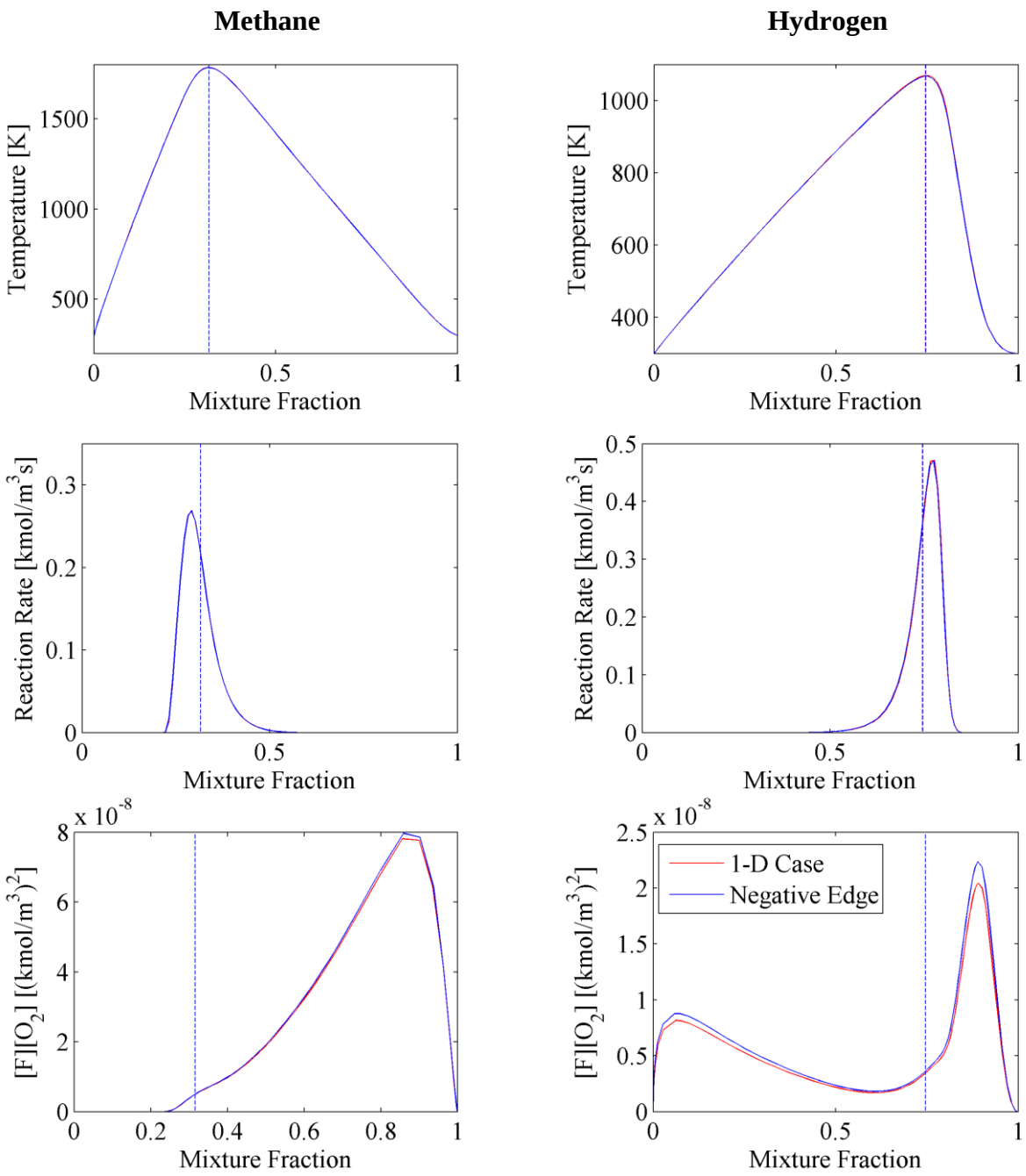

Figure 6.6: Temperature (top), reaction rate (center), and the product of fuel and oxidizer concentrations (bottom) for methane (left) and hydrogen (right) flames far from extinction. Both 1-D extinction (red) and a negative edge case (blue) are shown, and the location of peak temperature in each case is indicated by a vertical dotted line.

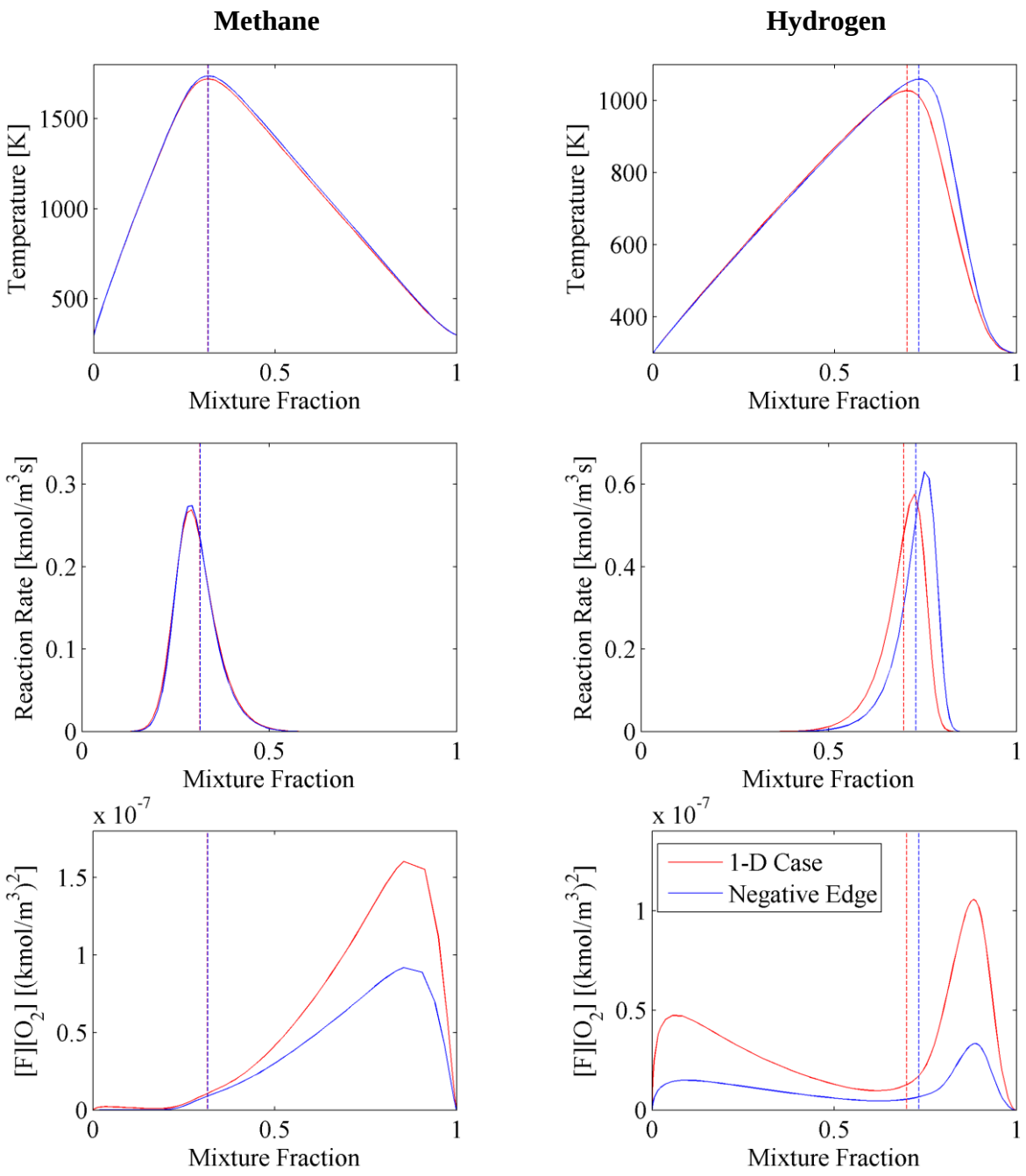

Figure 6.7: Temperature (top), reaction rate (center), and the product of fuel and oxidizer concentrations (bottom) for methane (left) and hydrogen (right) flames at the location where $\chi = \chi_{ext,1-D}$. Both 1-D extinction (red) and a negative edge case (blue) are shown, and the location of peak temperature in each case is indicated by a vertical dotted line.

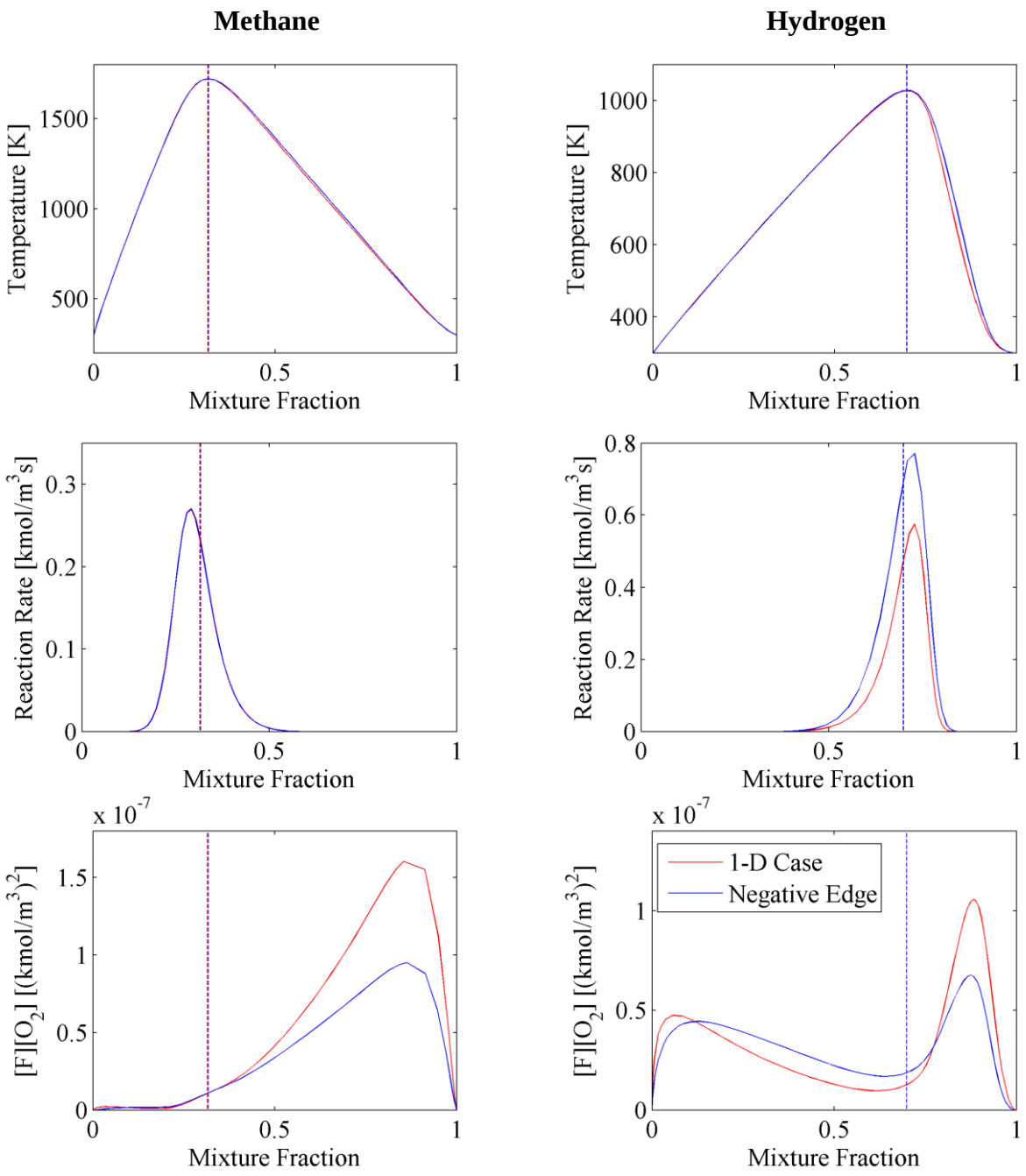

Figure 6.8: Temperature (top), reaction rate (center), and the product of fuel and oxidizer concentrations (bottom) for methane (left) and hydrogen (right) flames at the locations where $T_{max} = T_{ext}$. Both 1-D extinction (red) and a negative edge case (blue) are shown, and the location of peak temperature in each case is indicated by a vertical dotted line.

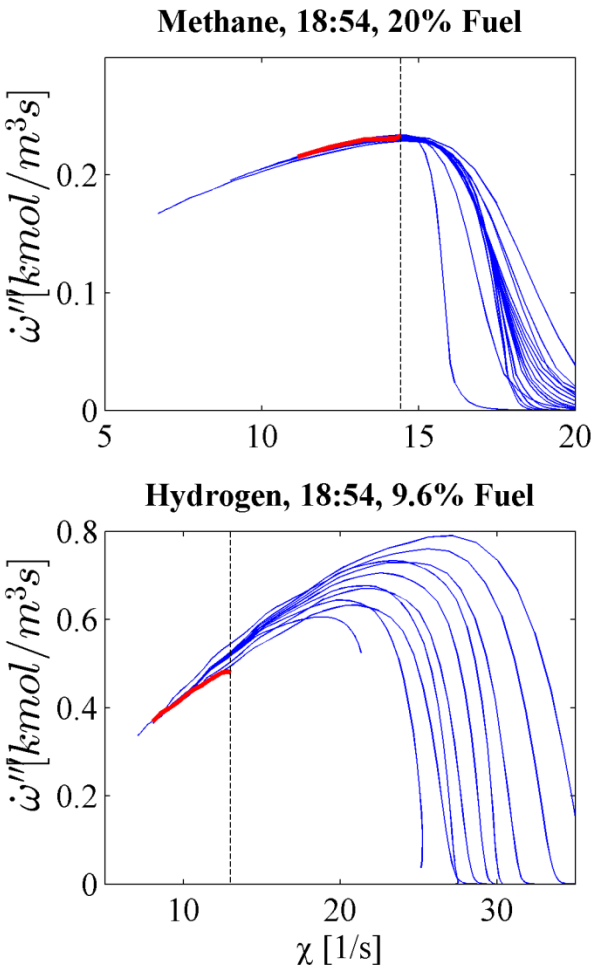

Figure 6.9: Reaction rate for 1-D extinction (red) and a variety of negative edge flames (blue) plotted as a function of local scalar dissipation rate. The scalar dissipation rate corresponding to 1-D extinction has been plotted with a dotted line.

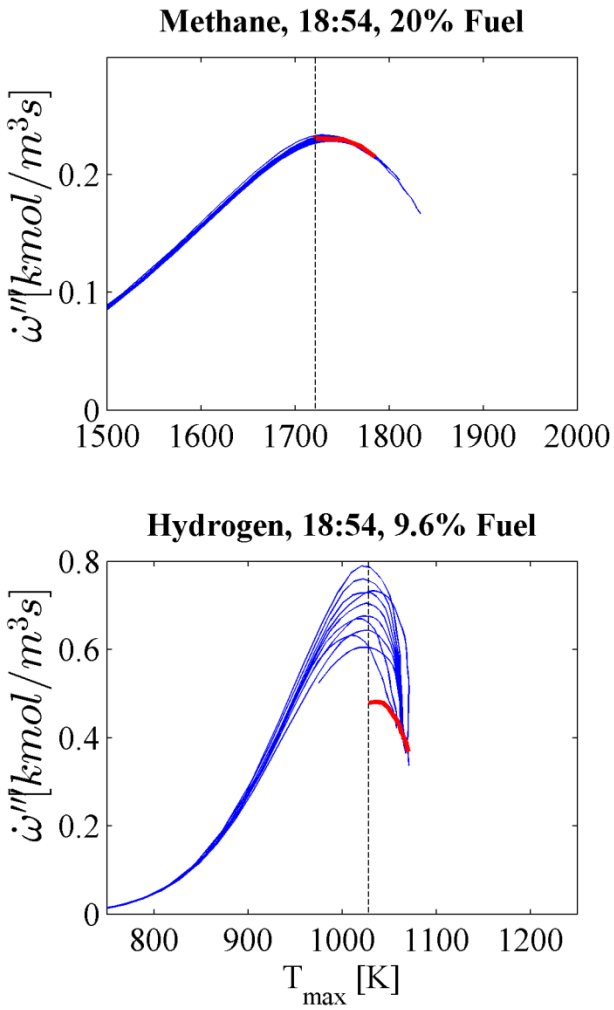

Figure 6.10: Reaction rate for 1-D extinction (red) and a variety of negative edge flames (blue) plotted as a function of local peak temperature. The temperature corresponding to 1-D extinction has been plotted with a dotted line.

7. Conclusions, Remarks, and Future Work

7.1 Three-Dimensional Flame Imaging

A Cassegrain system modeled on one previously used to make point measurements of chemiluminescence (Akamatsu *et al.*, 1999) was adapted and demonstrated to be useful for chemiluminescence imaging. The use of a Cassegrain system, as compared to a single lens system, improves spatial resolution and line-of-sight interference by reducing spherical and other aberrations. Images collected by the optimized Cassegrain system have a reduced depth of field as compared to the single lens imaging. This narrow depth of field helps to discern 2-D structures in the focused object plane of a 3-D object. These structures can be further enhanced by a maximum entropy algorithm that has been modified in this dissertation for use in three-dimensional imaging. By scanning one mirror in the Cassegrain system, the focused object plane was translated through a 3-D flame to measure a family of images with different focused depths. This set of stacked images of simple multi-flame configurations showed significant improvement over traditional single-lens images, though some out-of-plane interference remained in each image. Application of the maximum entropy algorithm reduced this interference considerably, and the reconstructed three-dimensional object matched the expected structure of the flame. Separation of out-of-plane flame fronts were clear over distances as small as 1 mm. Not only are two flames clearly visible, but the space between the two is clear – the flames do not overlap, and out of plane interference is minimal.

7.2 Chemiluminescence Turbulent Time-Series

High-speed chemilumescence videos were collected in a series of canonical, turbulent, nonpremixed jet flames. Time-series statistics such as power spectral densities (PSD's), autocorrelation functions (ACF's), and integral time scales. These line-integrated results were compared to previous spatially-resolved laser-induced fluorescence measurements (Renfro *et al.*, 2000c) of methyldine in order to assess the impact of line integration on measured integral time scales. The integral time scales calculated from the chemiluminescence videos were found to be universally longer than measured via LIF, due to out-of-plane contributions from regions of the flame with slower temporal behavior. However, this impact was reduced significantly by applying an Abel inversion to the frequency spectra, which are expected sum linearly due to the linearity of the Fourier transform. At a location of x/D = 10, the calculated integral time scales compare well to the previous LIF data. Additionally, simulated time series were generated in order to assess the impact of cross-correlation among constituent time series when performing an Abel inversion. It was discovered that cross-correlation has a significant impact upon recovered time series data in both correlated and uncorrelated cases. The measurement system was also found to be a large source of error in this work, as the high-speed camera used in data collection is prone to spatial artifacts in low signal-to-noise measurements. These artifacts were amplified during the inversion procedure, leading to significant noise in the reconstructed autocorrelations. However, this method of recovering frequency information from line-integrated videos shows promise in cases where optical access of an axisymmetric jet is limited, or when LIF is not possible due to cost or complexity.

7.3 Measurement of Scalar Dissipation Rate

Measurements of hydroxyl and formaldehyde PLIF in a steady flame with a stationary local extinction point were reported and compared to two-dimensional numerical simulations with detailed chemistry. Good qualitative agreement was shown between the measured and simulated signals. The usefulness of formaldehyde width as a predictor for local scalar dissipation rate was also evaluated for several simulated cases. Prior to extinction, the formaldehyde profile is self-similar and its width is correlated directly to local scalar dissipation rate. After extinction, however, formaldehyde production increases significantly due to incomplete combustion in the hot combustion products, as well as an increase in the Boltzmann fraction at low temperature. The width of the fluorescence profile is not correlated to scalar dissipation rate immediately following a local extinction event. However, in the strongly burning portion of the flame and through much of the extinction process (until a peak temperature of approximately 1400 K is reached), formaldehyde is still a useful predictor for scalar dissipation rate and the extinction point is well marked by the significant increase in fluorescence signal intensity (factor of more than 5). A combination of the fluorescence intensity used to identify the location of extinction and the fluorescence width upstream of this extinction point can still identify the scalar dissipation rate just preceding local extinction. Future work should look to apply this measurement technique to other canonical flames with local extinction events, particularly in the presence of turbulence.

7.4 Role of Heat Transfer in a Negative Edge Flame

Simulations of negative edge flames were performed with three fuels: methane (Le=1), ethane (Le>1), and hydrogen (Le<1) in order to better understand the impact of advection and molecular diffusion on the extinction process. Previously, Carnell and Renfro (2006) showed that advection through a negative edge causes extinction to occur at a higher scalar dissipation rate than is predicted by centerline extinction studies. The same effect was seen here, and was significantly enhanced when hydrogen was used as a fuel. This is due to enhanced molecular diffusion, which, when paired with heat addition from advection, increases the peak reaction rate considerably and allows the flame to burn at scalar dissipation rates approximately 100% higher than predicted by 1-D studies. This indicates two things: first, that the 1-D laminar flamelet model may significantly overpredict extinction in the presence of a negative edge, and second, that the local scalar dissipation rate is insufficient as an extinction criterion in this case, as it fails to account for molecular diffusion or advection. Further study is needed to understand the behavior of fuels with a Lewis number greater than unity.

Appendix: Ray-Tracing Algorithm

```
clear all

for k = 1:20

    X0 = [0 10 0];          %starting x locations [mm]
    Y0 = [0 0 10];          %starting y locations [mm]
    r1 = 304.8;             %radius of first mirror [mm]
    d1 = 152.4;             %diameter of first mirror [mm]
    M1 = [r1/2+180+(k-1)*1];    %location of first mirror [mm]
    r2 = 1000;               %radius of second mirror [mm]
    d2 = 25.4;              %diameter of second mirror [mm]
    S2 = 1/(2/r1-1/M1(1));  %determine and set ideal location
for second mirror
    M2(1) = M1(1)-S2+d2/d1*S2 + (k-10)*0.1;
    M2(2) = 0;
    Foc = 0;
    bins = [0 1 2 3 4 5];

    %Set maximum angle to minimize "junk" rays
    maxAng = atan((d1/2)/M1(1));

    %Generate 1000 rays over the range -maxAngle to maxAngle
    theta = linspace(-maxAng,maxAng,1000);

    %repeat for three locations to establish magnification and
DOF
    for i = 1:3

        count = 1;

        Obj = [X0(i) Y0(i)];

        %repeat for 1000 rays
        for j = 1:1000

            %calculate resultant x and y components of vector
            v01 = [cos(theta(j)) sin(theta(j))];

            %rewrite vector in y=mx+b form
            m01 = tan(theta(j));
            b01 = Obj(2) - m01*Obj(1);

            %determine if ray is blocked by second mirror
```

```
            y2 = m01*M2(1) + b01;

            if abs(y2) <= d2/2                          %blocked
                errors(i,j) = 1;
            else                                        %not blocked

                %find intersection of vector and first mirror
                cx1 = M1(1)-r1;
                poly01 = [(m01^2+1) (2*m01*b01-2*cx1)
(cx1^2+b01^2-r1^2)];
                roots01 = roots(poly01);

                %determine if roots are real
                if real(roots01) ~= roots01         %not real
                    errors(i,j) = 2;
                else                                %real

                    %determine if ray hits mirror1
                    int01(1) = max(roots01);
                    int01(2) = m01*int01(1)+b01;

                    if abs(int01(2)) > d1/2     %misses
                        errors(i,j) = 3;
                    else                            %hits

                        %define surface normal for mirror 1
                        n1 = [(int01(1)-cx1) (int01(2))];
                        n1 = n1/norm(n1);

                        %reflect vector about normal
                        v12 = v01 - 2*dot(v01,n1)*n1;

                        %write in y=mx+b form
                        m12 = v12(2)/v12(1);
                        b12 = int01(2) - m12*int01(1);

                        %find intersection with mirror 2
                        cx2 = M2(1)-r2;
                        poly12 = [(m12^2+1) (2*m12*b12-2*cx2)
(cx2^2+b12^2-r2^2)];
                        roots12 = roots(poly12);

                        %determine if roots are real
                        if real(roots12) ~= roots12     %not
real
                            errors(i,j) = 4;
                        else                            %real
```

```
                            %determine if ray hits mirror 2
                            int12(1) = max(roots12);
                            int12(2) = m12*int12(1)+b12;

                            if abs(int12(2)) > d2/2     %misses
                                errors(i,j) = 5;
                            else                        %hits

                                %define surface normal for
mirror 2
                                n2 = [(int12(1)-cx2) int12(2)];
                                n2 = n2/norm(n2);

                                %reflect vector about normal
                                v23 = v12 - 2*dot(v12,n2)*n2;

                                %write in y=mx+b form
                                m23(count) = v23(2)/v23(1);
                                b23(count) = int12(2)-
m23(count)*int12(1);

                                %if focal plane has not been
defined,
                                %record where each ray focuses
                                if i == 1

                                    Foc(count) = -
b23(count)/m23(count);
                                    count = count + 1;

                                else

                                    rays{i}(count) =
m23(count)*FocA+b23(count);
                                    count = count+1;
                                end
                            end
                        end
                    end
                end
            end
        end


        if i == 1
            SA = range(Foc);
```

```
            FocA = mean(Foc);
            rays{1} = m23*FocA+b23;
        end

        clear m23
        clear b23

        errorA(i,:) = hist(errors(i,:),bins);

    end

    if min(errorA(:,1))~=0

        mag = (mean(rays{3})-mean(rays{1}))/10;

        results(k,1) = M1(1);
        results(k,2) = M2(1);
        results(k,3) = FocA;
        results(k,4) = SA;
        results(k,5) = range(rays{1});
        results(k,6) = min(abs(rays{2}))/10;
        results(k,7) = mag;
        results(k,8) = errorA(1,1)/1000;
        results(k,9) = min(abs(rays{1}));
        results(k,10) = max(abs(rays{1}));

        clear rays
        clear errorA
        clear errors

    end

end
```

List of References

Akamatsu, F., Wakabayashi, T., Tsushima, S., Katsuki, M., Mizutani, Y., Ikeda, Y., Kawahara, N., and Nakajima, T. 1999. The development of a light-collecting probe with high spatial resolution applicable to randomly fluctuating combustion fields. *Meas. Sci. Technol.*, 10 (12), 1240–1246.

Amantini, G., Frank, J.H., and Gomez, A. 2005. Experiments on standing and traveling edge flames around flame holes. *Proc. Combust. Inst.*, 30, 313–321.

ANSYS 2009. *Fluent User Manual, Version 12.0*.

Ayoola, B.O., Balachandran, R., Frank, J.H., Mastorakos, E., and Kaminski, C.F. 2006. Spatially resolved heat release rate measurements in turbulent premixed flames. *Combust. Flame*, 144, 1–16.

Balachandran, R., Ayoola, B.O., Kaminski, C.F., Dowling, A., and Mastorakos, E. 2005. Experimental investigation of the nonlinear response of turbulent premixed flames to imposed inlet velocity oscillations. *Combust. Flame*, 143 (1-2), 37–55.

Barlow, R.S., Fiechtner, G.J., Carter, C.D., and Chen, J.Y. 2000. Experiments on the scalar structure of turbulent $CO/H_2/N_2$ jet flames. *Combust. Flame*, 120 (4), 549–569.

Bergmann, V., Meier, W., Wolff, D., and Stricker, W. 1998. Application of spontaneous Raman and Rayleigh scattering and 2D LIF for the characterization of a turbulent $CH_4/H_2/N_2$ jet diffusion flame. *Appl. Phys. B Lasers Opt.*, 66, 489–502.

Bevensee, R.M. 1993. *Maximum Entropy Solutions to Scientific Problems*. Edgewood Cliffs, NJ: Prentice-Hall, Inc.

Bheemul, H.C., Lu, G., and Yan, Y. 2002. Three-dimensional visualization and quantitative characterization of gaseous flames. *Meas. Sci. Technol.*, 13 (10), 1643–1650.

Bheemul, H.C., Lu, G., and Yan, Y. 2005. Digital imaging-based three-dimensional characterization of flame front structures in a turbulent flame. *IEEE Trans. Instrum. Meas.*, 54 (3), 1073–1078.

Bijjula, K. and Kyritsis, D.C. 2005. Experimental evaluation of flame observables for simplified scalar dissipation rate measurements in laminar diffusion flamelets. *Proc. Combust. Inst.*, 30 (1), 493–500.

Bilger, R.W. 1988. The structure of turbulent nonpremixed flames. *Symp. Combust.*, 22 (1), 475–488.

Bolan, J.T., Johnson, K.C., and Thurow, B.S. 2014. Preliminary investigation of three-dimensional flame measurements with a plenoptic camera. *In*: *AIAA Aviat.* Atlanta, GA.

Boulanger, J. and Vervisch, L. 2002. Diffusion edge-flame: approximation of the flame tip Damköhler number. *Combust. Flame*, 130, 1–14.

Box, G.E.P., Jenkins, G.M., and Reinsel, G.C. 2008. *Time Series Analysis*. Hoboken, NJ: John Wiley & Sons, Inc.

Bracewell, R.N. 2004. *Fourier Analysis and Imaging*. New York: Springer.

Brackmann, C., Nygren, J., Bai, X., Li, Z., Bladh, H., Axelsson, B., Denbratt, I., Koopmans, L., Bengtsson, P.-E., and Aldén, M. 2003. Laser-induced fluorescence of formaldehyde in combustion using third harmonic Nd:YAG laser excitation. *Spectrochim. Acta Part A Mol. Biomol. Spectrosc.*, 59, 3347–3356.

Brisley, P.M. and Lu, G. 2005. Three-dimensional temperature measurement of combustion flames using a single monochromatic CCD camera. *IEEE Trans. Instrum. Meas.*, 54 (4), 1417–1421.

Broda, J.C., Seo, S., Santoro, R.J., Shirhattikar, G., and Yang, V. 1998. An experimental study of combustion dynamics of a premixed swirl injector. *Symp. Combust.*, 27 (2), 1849–1856.

Bryan, R.K. and Skilling, J. 1980. Deconvolution by maximum entropy, as illustrated by application to the jet of M87. *Mon. Not. R. Astron. Soc.*, 191, 69–79.

Buckmaster, J. 1996. Edge-flames and their stability. *Combust. Sci. Technol.*, 115, 41–68.

Caretto, L.S., Gosman, A.D., Patankar, S. V., and Spalding, D.B. 1973. Two calculation procedures for steady, three-dimensional flows with recirculation. *Lect. Notes Phys.*, 19, 60–68.

Carnell, Jr., W.F. 2006. *Experimental and numerical study of extinction in negative edge laminar flames*. University of Connecticut, Storrs, Connecticut.

Carnell, Jr., W.F., Gosselin, K.R., and Renfro, M.W. 2009. Comparison of measured and simulated OH and CH_2O distributions through a local extinction. *In*: *Proc. 2009 Jt. U.S. Sect. Meet. Combust. Inst.* Ann Arbor, MI: The Combustion Institute.

Carnell, Jr., W.F. and Renfro, M.W. 2005. Stable negative edge flame formation in a counterflow burner. *Combust. Flame*, 141 (4), 350–359.

Carnell, Jr., W.F. and Renfro, M.W. 2006. Influence of advective heat flux on extinction scalar dissipation rate and velocity in negative edge flames. *Combust. Theory Model.*, 10 (5), 815–830.

Carnell, Jr., W.F. and Renfro, M.W. 2007. Measurement of temperature gradients through local extinction using Raman scattering spectroscopy. *Int. J. Altern. Propuls.*, 1 (2), 135–153.

Cha, M.S. and Ronney, P.D. 2006. Propagation rates of nonpremixed edge flames. *Combust. Flame*, 146, 312–328.

Chen, J.H. and Im, H.G. 1998. Correlation of flame speed with stretch in turbulent premixed methane/air flames. *Symp. Combust.*, 27 (1), 819–826.

Cho, Y.T. and Na, S.-J. 2005. Application of Abel inversion in real-time calculations for circularly and elliptically symmetric radiation sources. *Meas. Sci. Technol.*, 16, 878–884.

Chung, S.H. and Law, C.K. 1983. Structure and extinction of convective diffusion flames with general Lewis numbers. *Combust. Flame*.

Clemens, N.T. and Paul, P.H. 1995. Effects of heat release on the near field flow structure of hydrogen jet diffusion flames. *Combust. Flame*, 102 (3), 271–284.

Compact Kinematic Mounts [online] 2015. *Thorlabs*. Available from: http://www.thorlabs.com/newgrouppage9.cfm?objectgroup_id=52 [Accessed 8 May 2015].

Coriton, B. and Frank, J.H. 2014. High-speed tomographic PIV measurements of strain rate intermittency and clustering in turbulent partially-premixed jet flames. *Proc. Combust. Inst.*, 35 (2), 1243–1250.

Cornwell, T.J. and Evans, K.F. 1985. A simple maximum entropy deconvolution algorithm. *Astron. Astrophys.*, 143 (1), 77–83.

Daou, R., Daou, J., and Dold, J. 2002. Effect of volumetric heat loss on triple-flame propagation. *Proc. Combust. Inst.*, 29, 1559–1564.

Dasch, C.J. 1992. One-dimensional tomography: a comparison of Abel, onion-peeling, and filtered backprojection methods. *Appl. Opt.*, 31 (8), 1146–1152.

Davis, M.R. 1987. Determination of turbulent flow properties by a penetrating beam dynamic shadowgraph method. *J. Phys. E.*, 20, 1271–1277.

Doroshko, M.V., Penyaz'kov, O.G., Rankin, G., Sevruk, K.L., Khramtsov, P.P., and Shikh, I.A. 2006. Talbot interferometry in measurements of the parameters of an axisymmetric turbulent jet. *J. Eng. Phys. Thermophys.*, 79 (5), 937–942.

Experimental Data Archives [online] 2014. *TNF Work.* Available from: http://www.sandia.gov/TNF/simplejet.html [Accessed 7 May 2014].

El Fagrich, M. and Chehouani, H. 2012. A simple Abel inversion method of interferometric data for temperature measurement in axisymmetric medium. *Opt. Lasers Eng.*, 50 (3), 336–344.

Favier, V. and Vervisch, L. 2001. Edge flames and partially premixed combustion in diffusion flame quenching. *Combust. Flame*, 125, 788–803.

Fayoux, A., Zähringer, K., Gicquel, O., and Rolon, J.C. 2005. Experimental and numerical determination of heat release in counterflow premixed laminar flames. *Proc. Combust. Inst.*, 30, 251–257.

Floyd, J., Geipel, P., and Kempf, A.M. 2011. Computed tomography of chemiluminescence (CTC): instantaneous 3D measurements and phantom studies of a turbulent opposed jet flame. *Combust. Flame*, 158 (2), 376–391.

Freeman, R. and Garcia, H. 1982. High-speed deformable mirror system. *Appl. Opt.*, 21 (4), 589–595.

Frenklach, M., Wang, H., Goldenberg, M., Smith, G.P., Golden, D.M., Bowman, C.T., Hanson, R.K., Gardiner, W.C., and Lissianski, V. 1995. *GRI-Mech---An Optimized Detailed Chemical Reaction Mechanism for Methane Combustion, Report No. GRI-95/0058*.

Frieden, B.R. 1972. Restoring with maximum likelihood and maximum entropy. *J. Opt. Soc. Am.*, 62 (4), 511.

Fujita, O., Ito, K., Kang, W., Tanaka, K., and Morita, T. 1995. Visualization of formaldehyde distribution produced in catalytic oxidation of methanol on platinum plate by LIF method. *Trans. Japan Soc. Mech. Eng. Part B*, 61 (591), 4214–4218.

Future Climate Change [online] 2014. *U.S. Environ. Prot. Agency*. Available from: http://www.epa.gov/climatechange/science/future.html.

Gaskey, S., Vacus, P., David, R., Villermaux, J., and André, J.C. 1990. A method for the study of turbulent mixing using fluorescence spectroscopy. *Exp. Fluids*, 9 (3), 137–147.

Geitlinger, H., Streibel, T.H., Suntz, R., and Bockhorn, H. 1999. Statistical Analysis of Soot Volume Fractions, Particle Number Densities and Particle Radii in a Turbulent Diffusion Flame. *Combust. Sci. Technol.*, 149 (1-6), 115–134.

Giacomazzi, E., Bruschi, R., Giammartini, S., Giulietti, E., Manfredi, F., Stingola, C., Daniele, S., and Troiani, G. 2005. Experimental and numerical unsteady characterization of turbulent combustion. *41st AIAA/ASME/SAE/ASEE Jt. Propuls. Conf. Exhib.*, (2005-3579).

Giacomazzi, E., Troiani, G., Giulietti, E., and Bruschi, R. 2008. Effect of turbulence on flame radiative emission. *Exp. Fluids*, 44 (4), 557–564.

Gilabert, G., Lu, G., and Yan, Y. 2007. Three-dimensional tomographic reconstruction of the luminosity distribution of a combustion flame. *IEEE Trans. Instrum. Meas.*, 56 (4), 1300–1306.

Gord, J.R., Meyer, T.R., and Roy, S. 2008. Applications of ultrafast lasers for optical measurements in combusting flows. *Annu. Rev. Anal. Chem. (Palo Alto. Calif).*, 1, 663–87.

Gosselin, K.R., Carnell, Jr., W.F., and Renfro, M.W. 2013a. Formaldehyde fluorescence as a marker for scalar dissipation through local extinction. *In*: *Meet. East. States Sect. Combust. Inst.*

Gosselin, K.R., Carnell, Jr., W.F., and Renfro, M.W. 2015a. Formaldehyde fluorescence as a marker for scalar dissipation through local extinction. *Combust. Sci. Technol.*, in press.

Gosselin, K.R., Kopp-Vaughan, K.M., and Renfro, M.W. 2013b. Influence of fuel type on advective heat flux and extinction scalar dissipation rate in negative edge flames. *In*: *Proc. 2013 Jt. Sect. Meet. Combust. Inst.* Park City, UT.

Gosselin, K.R., Kopp-Vaughan, K.M., and Renfro, M.W. 2015b. Influence of advection in the stability of negative edge flames. *Prep.*

Gosselin, K.R. and Renfro, M.W. 2011. Reconstruction of three-dimensional chemiluminescence images with a maximum entropy deconvolution algorithm. *In*: *Proc. 2011 Jt. U.S. Sect. Meet. Combust. Inst.* Atlanta, GA, GA, 1671–80.

Gosselin, K.R., Stoddard, J.P., and Renfro, M.W. 2015c. Measuring time-series statistics in an axisymmetric, turbulent jet with line-integrated chemiluminescence. *Prep.*

Gull, S.F. and Skilling, J. 1984. Maximum entropy method in image processing. *IEE Proc. F Commun. Radar Signal Process.*, 131 (6), 646.

Gut, Z. and Wolanski, P. 2010. Flame imaging using 3D electrical capacitance tomography. *Combust. Sci. Technol.*, 182 (11-12), 1580–1585.

High-Performance Long-Travel Linear Motor Stages IMS-LM Series [online] 2015. *Newport Opt.* Available from: http://www.newport.com/IMS-LM-Series-High-Performance-Long-Travel-Linear/400011/1033/info.aspx [Accessed 8 May 2015].

Hult, J., Meier, U.E., Meier, W., Harvey, A.P., and Kaminski, C.F. 2005. Experimental analysis of local flame extinction in a turbulent jet diffusion flame by high repetition 2-D laser techniques and multi-scalar measurements. *Proc. Combust. Inst.*, 30 (1), 701–709.

Ida, T. and Ohtake, K. 1997. Experimental study of turbulent diffusion flame structure and its similarity. *JSME Int.*, 40 (2), 304–311.

Ihme, M. and Pitsch, H. 2008. Prediction of extinction and reignition in nonpremixed turbulent flames using a flamelet/progress variable model. 2. Application in LES of Sandia flames D and E. *Combust. Flame*, 155 (1-2), 90–107.

Janus, B., Dreizler, a., and Janicka, J. 2005. Experimental study on stabilization of lifted swirl flames in a model GT combustor. *Flow, Turbul. Combust.*, 75 (1-4), 293–315.

Karpetis, A.N. and Barlow, R.S. 2005. Measurements of flame orientation and scalar dissipation in turbulent partially premixed methane flames. *Proc. Combust. Inst.*, 30 (1), 665–672.

Karpetis, A.N., Settersten, T.B., Schefer, R.W., and Barlow, R.S. 2004. Laser imaging system for determination of three-dimensional scalar gradients in turbulent flames. *Opt. Lett.*, 29 (4), 355.

Katta, V.R., Meyer, T.R., Brown, M.S., Gord, J.R., and Roquemore, W.M. 2004. Extinction criterion for unsteady, opposing-jet diffusion flames. *Combust. Flame*, 137, 198–221.

Kheirkhah, S. and Gülder, Ö.L. 2013. Turbulent premixed combustion in V-shaped flames: Characteristics of flame front. *Phys. Fluids*, 25 (055107), 1–24.

Kiefer, J., Li, Z.S., Zetterberg, J., Bai, X.S., and Aldén, M. 2008. Investigation of local flame structures and statistics in partially premixed turbulent jet flames using simultaneous single-shot CH and OH planar laser-induced fluorescence imaging. *Combust. Flame*, 154 (4), 802–818.

Killer, C. 2014. Abel Inversion Algorithm [online]. *MATLAB File Exch.* Available from: http://www.mathworks.com/matlabcentral/fileexchange/43639-abel-inversion-algorithm.

Kim, J.S. and Williams, F.A. 1997. Extinction of diffusion flames with nonunity Lewis numbers. *J. Eng. Math.*, 101–118.

Kioni, P.N., Bray, K.N.C., Greenhalgh, D.A., and Rogg, B. 1999. Experimental and numerical studies of a triple flame. *Combust. Flame*, 116, 192–206.

Kioni, P.N., Rogg, B., Bray, K.N.C., and Liñán, A. 1993. Flame spread in laminar mixing layers: the triple flame. *Combust. Flame*, 95, 276–290.

Kolmogorov, A.N. 1991. Local structure of turbulence in an incompressible fluid for very large Reynolds numbers. *In*: *Proc. R. Soc. London A*. 9–13.

Kuo, K.K. and Acharya, R. 2012. *Fundamentals of Turbulent Combustion and Multiphase Combustion*. Hoboken, NJ: John Wiley & Sons, Inc.

Kuo, K.K.Y. 1986. *Principles of Combustion*. New York: John Wiley & Sons, Inc.

Kyritsis, D.C., Santoro, V.S., and Gomez, A. 2004. The effect of temperature correction on the measured thickness of formaldehyde zones in diffusion flames for 355 nm excitation. *Exp. Fluids*, 37, 769–772.

Landenfeld, T., Sadiki, a., and Janicka, J. 2002. A turbulence-chemistry interaction model based on a multivariate presumed beta-PDF method for turbulent flames. *Flow, Turbul. Combust.*, 68, 111–135.

Laurendeau, N.M. 1988. Temperature measurements by light-scattering methods. *Prog. energy Combust. Sci.*, 14, 147–170.

Laurendeau, N.M. 2005. *Statistical Thermodynamics*. New York: Cambridge University Press.

Law, C.K. 2006. *Combustion Physics*. New York: Cambridge University Press.

Lawn, C.J. 2000. Distributions of instantaneous heat release by the cross-correlation of chemiluminescent emissions. *Combust. Flame*, 123 (00), 227–240.

Lee, J., Won, S.H., Jin, S.H., and Chung, S.H. 2003. Lifted flames in laminar jets of propane in coflow air. *Combust. Flame*, 135, 449–462.

Lee, U.D., Yoo, C.S., Chen, J.H., and Frank, J.H. 2010. Effect of NO on extinction and re-ignition of vortex-perturbed hydrogen flames. *Combust. Flame*, 157 (2), 217–229.

Lee, W. and Na, Y.D. 2000. Soot study in laminar diffusion flames at elevated pressure using two-color pyrometry and Abel inversion. *JSME Int. J.*, 43 (4), 550–555.

Leonard, B.P. 1979. A stable and accurate convective modelling procedure based on quadratic upstream interpolation. *Comput. Methods Appl. Mech. Eng.*, 19, 59–98.

Lewis, K.J. and Moss, J.B. 1979. Time-resolved scalar measurements in a confined turbulent premixed flame. *Symp. Combust.*, 17 (1), 267–277.

Li, Z.S., Li, B., Sun, Z.W., Bai, X.S., and Aldén, M. 2010. Turbulence and combustion interaction: high resolution local flame front structure visualization using simultaneous single-shot PLIF imaging of CH, OH, and CH_2O in a piloted premixed jet flame. *Combust. Flame*, 157 (6), 1087–1096.

Liñán, A. 1974. The assymtotic structure of counterflow diffusion flames for large activation energies. *Acta Astronaut.*, 1, 1007–1039.

Long, M., Kaiser, S. a., and Frank, J.H. 2006. Imaging scalar dissipation in flames. *Laser Applilcations to Chem. Secur. Environ. Anal.*, MB1.

Luque, J., Jeffries, J.B., Smith, G.P., Crosley, D.R., Walsh, K.T., Long, M.B., and Smooke, M.D. 2000. CH(A-X) and OH(A-X) optical emission in an axisymmetric laminar diffusion flame. *Combust. Flame*, 122 (1-2), 172–175.

Magnotti, G. and Barlow, R.S. 2014. Effects of high shear on the structure and thickness of turbulent premixed methane/air flames stabilized on a bluff-body burner. *Combust. Flame*, 1–15.

Mayrhofer, N. and Woisetschläger, J. 2001. Frequency analysis of turbulent compressible flows by laser vibrometry. *Exp. Fluids*, 31, 153–161.

McGee, H.A. 1991. *Molecular Engineering*. New York: McGraw-Hill.

MEMS-Based Deformable Mirrors [online] 2015. *Thorlabs*. Available from: https://www.thorlabs.com/newgrouppage9.cfm?objectgroup_id=3258 [Accessed 8 May 2015].

Metz, T., Bai, X., Ossler, F., and Aldén, M. 2004. Fluorescence lifetimes of formaldehyde (H_2CO) in the A1A2 --> X1A2 band system at elevated temperatures and pressures. *Spectrochim. Acta Part A Mol. Biomol. Spectrosc.*, 60, 1043–1053.

Monthly Energy Review, October 2014 2014. Washington, D.C.

Olofsson, J., Richter, M., Aldén, M., and Augé, M. 2006. Development of high temporally and spatially (three-dimensional) resolved formaldehyde measurements in combustion environments. *Rev. Sci. Instrum.*, 77 (1), 013104.

Olofsson, J., Seyfreid, H., Richter, M., Aldén, M., Vressner, A., Hultqvist, A., Johansson, B., and Lombaert, K. 2005. High-speed LIF imaging for cycle-resolved formaldehyde visualization in HCCI combustion. *In*: *SAE Tech. Pap.*

Panoutsos, C.S., Hardalupas, Y., and Taylor, a. M.K.P. 2009. Numerical evaluation of equivalence ratio measurement using OH* and CH* chemiluminescence in premixed and non-premixed methane-air flames. *Combust. Flame*, 156 (2), 273–291.

Pantano, C. 2004. Direct simulation of non-premixed flame extinction in a methane–air jet with reduced chemistry. *J. Fluid Mech.*, 514, 231–270.

Patankar, S. 1980. *Numerical heat transfer and fluid flow*. Ser. Comput. Methods Mech. Therm. Sci. Washington, D.C.: Hemisphere Publishing Corp.

Patankar, S.V. and Spalding, D.B. 1972. A calculation procedure for heat, mass and momentum transfer in three-dimensional parabolic flows. *Int. J. Heat Mass Transf.*, 15, 1787–1806.

Paul, P.H. and Najm, H.N. 1998. Planar laser-induced fluorescence imaging of flame heat release rate. *Proc. Combust. Inst.*, 27, 43–50.

Peters, N. 1988. Laminar flamelet concepts in turbulent combustion. *Symp. Combust.*, 21 (1), 1231–1250.

Plessing, T., Terhoeven, P., Peters, N., and Mansour, M.S. 1998. An experimental and numerical study of a laminar triple flame. *Combust. Flame*, 115, 335–353.

Pope, S.B. 2011. *Turbulent Flows*. New York: Cambridge University Press.

Pretzler, G. 1991. A new method for numerical abel-inversion. *Zeitschrift für Naturforschung. A, A J. Phys. Sci.*, 46a, 639–641.

Pretzler, G., Jäger, H., Neger, T., and Philipp, H. 1992. Comparison of different methods of Abel inversion using computer simulated and experimental side-on. *Zeitschrift für Naturforsch. A*, 0 (1992).

Puri, I.K., Aggarwal, S.K., Ratti, S., and Azzoni, R. 2001. On the similitude between lifted and burner-stabilized triple flames: a numerical and experimental investigation. *Combust. Flame*, 124 (1-2), 311–325.

Qin, X., Puri, I.K., and Aggarwal, S.K. 2002. Characteristics of lifted triple flames stabilized in the near field of a partially premixed axisymmetric jet. *Proc. Combust. Inst.*, 29, 1565–1572.

Rankin, B.A., Blunck, D.L., and Gore, J.P. 2013. Infrared imaging and spatiotemporal radiation properties of a turbulent nonpremixed jet flame and plume. *J. Heat Transfer*, 135 (2), 021201.

Rankin, B.A., Magnotti, G., Barlow, R.S., and Gore, J.P. 2014. Radiation intensity imaging measurements of methane and dimethyl ether turbulent nonpremixed and partially premixed jet flames. *Combust. Flame*, 161 (11), 2849–2859.

Renfro, M.W. 2000. *Quantitative Time Series for Minor-Species Concentrations: Measurements and Modeling in Turbulent Nonpremixed Flames*. Purdue University.

Renfro, M.W., Chaturvedy, A., King, G.B., Laurendeau, N.M., Kempf, A., Dreizler, A., and Janicka, J. 2004. Comparison of OH time-series measurements and large-eddy simulations in hydrogen jet flames. *Combust. Flame*, 139 (1-2), 142–151.

Renfro, M.W., Gore, J.P., King, G.B., and Laurendeau, N.M. 2000a. Self-similarity of hydroxyl-concentration temporal statistics in turbulent nonpremixed jet flames. *AIAA J.*, 38 (7), 1230–1236.

Renfro, M.W., Gore, J.P., and Laurendeau, N.M. 2002. Scalar time-series simulations using flamelet state relationships for turbulent non-premixed flames. *Combust. Flame*, 129 (1-2), 120–135.

Renfro, M.W., Guttenfelder, W.A., King, G.B., and Laurendeau, N.M. 2000b. Scalar time-series measurements in turbulent $CH_4/H_2/N_2$ nonpremixed flames: OH. *Combust. Flame*, 123, 389–401.

Renfro, M.W., King, G.B., and Laurendeau, N.M. 2000c. Scalar time-series measurements in turbulent $CH_4/H_2/N_2$ nonpremixed flames: CH. *Combust. Flame*, 122 (1-2), 139–150.

Röder, M., Dreier, T., and Schulz, C. 2012. Simultaneous measurement of localized heat release with OH/CH 2O-LIF imaging and spatially integrated OH* chemiluminescence in turbulent swirl flames. *Appl. Phys. B Lasers Opt.*, 107 (2), 611–617.

Rolon, J.C., Aguerre, F., and Candel, S. 1995. Experiments on the interaction between a vortex and a strained diffusion flame. *Combust. Flame*, 100, 422–429.

Santoro, V.S., Kyritsis, D.C., Smooke, M.D., and Gomez, A. 2002. Nitric oxide formation during flame/vortex interaction. *Proc. Combust. Inst.*, 29, 2227–2233.

Santoro, V.S., Liñán, A., and Gomez, A. 2000. Propagation of edge flames in counterflow mixing layers: Experiments and theory. *Proc. Combust. Inst.*, 28 (2), 2039–2046.

Schneider, M.D. 2014. *Experimental Studies of Turbulent Local Extinction*. Storrs, Connecticut: M.S. Thesis, University of Connecticut.

Seitzman, J.M., Kychakoff, G., and Hanson, R.K. 1985. Instantaneous temperature field measurements using planar laser-induced fluorescence. *Opt. Lett.*, 10 (9), 439.

Shaevitz, J.W. and Fletcher, D.A. 2007. Enhanced three-dimensional deconvolution microscopy using a measured depth-varying point-spread function. *J. Opt. Soc. Am. A. Opt. Image Sci. Vis.*, 24 (9), 2622–7.

Shay, M.L. and Ronney, P.D. 1998. Nonpremixed edge flames in spatially varying straining flows. *Combust. Flame*, 112, 171–180.

Shih, H.-Y. 2009. Computed extinction limits and flame structures of H2/O2 counterflow diffusion flames with CO2 dilution. *Int. J. Hydrogen Energy*, 34 (9), 4005–4013.

Shimura, M., Ueda, T., Choi, G.M., Tanahashi, M., and Miyauchi, T. 2011. Simultaneous dual-plane CH PLIF, single-plane OH PLIF and dual-plane stereoscopic PIV measurements in methane-air turbulent premixed flames. *Proc. Combust. Inst.*, 33 (1), 775–782.

Shore, J.E. and Johnson, R.W. 1980. Axiomatic derivation of the principle of maximum entropy and the principle of minimum cross-entropy. *IEEE Trans. Inf. Theory*, 26 (1), 26–37.

Smith, G.P., Golden, D.M., Frenklach, M., Moriarty, N.W., Eiteneer, B., Goldenberg, M., Bowman, C.T., Hanson, R.K., Song, S., Gardiner, W.C., Lassianski, V. V., and Qin, Z. n.d. No Title [online]. *GRI Mech. Database*. Available from: http://www.me.berkeley.edu/gri_mech/.

Spalding, D.B. 1953. The combustion of liquid fuels. *Symp. Combust.*, 4 (1), 847–864.

Spalding, D.B. 1972. A novel finite difference formulation for differential expressions involving both first and second derivatives. *Inernational J. Numer. Methods Eng.*, 4, 551–559.

Sripagakorn, P., Satoshi, M., Kosaly, G., and Pitsch, H. 2004. Extinction and reignition in a diffusion flame: a direct numerical simulation study. *J. Fluid Mech.*, 518, 231–259.

T'ien, J.S. 1975. A discussion on the extinction condition of a diffusion flame. *J. Fire Flammabl.*, 6, 101–104.

Tamura, M., Berg, P.A., Harrington, J.E., Luque, J., Jeffries, J.B., Smith, G.P., and Crosley, D.R. 1998. Collisional Quenching of CH(A), OH(A), and NO(A) in Low Pressure Hydrocarbon Flames. *Combust. Flame*, 114, 502–514.

Taylor, R. and Krishna, R. 1993. *Multicomponent Mass Transfer*. New York: John Wiley & Sons, Inc.

Upton, T.D., Verhoeven, D.D., and Hudgins, D.E. 2010. High-resolution computed tomography of a turbulent reacting flow. *Exp. Fluids*, 50 (1), 125–134.

VanDerWege, B. a., O'Brien, C.J., and Hochgreb, S. 1999. Quantitative shearography in axisymmetric gas temperature measurements. *Opt. Lasers Eng.*, 31 (1), 21–39.

Veynante, D., Lodato, G., Domingo, P., Vervisch, L., and Hawkes, E.R. 2010. Estimation of three-dimensional flame surface densities from planar images in turbulent premixed combustion. *Exp. Fluids*, 49 (1), 267–278.

Veynante, D.P., Piana, J., Duclos, J.M., and Martel, C. 1996. Experimental analysis of flame structure surface density models for premixed turbulent combustion. *Proc. Combust. Inst.*, (3), 413–420.

Wang, G.-H., Clemens, N.T., Varghese, P.L., and Barlow, R.S. 2008. Turbulent time scales in a nonpremixed turbulent jet flame by using high-repetition rate thermometry. *Combust. Flame*, 152 (3), 317–335.

Wang, H.Y., Chen, W.H., and Law, C.K. 2007. Extinction of counterflow diffusion flames with radiative heat loss and nonunity Lewis numbers. *Combust. Flame*, 148 (3), 100–116.

Wang, Y.M., Wang, H.B., Li, F.H., Jia, L.S., and Chen, X.L. 2005. Maximum entropy image deconvolution applied to structure determination for crystal Nd1.85Ce0.15CuO4-delta. *Micron*, 36 (5), 393–400.

Watson, K.A., Lyons, K.M., Donbar, J.M., and Carter, C.D. 2000. Simultaneous Rayleigh Imaging and CH-PLIF Measurements in a Lifted Jet Diffusion Flame. *Combust. Flame*, 123, 252–265.

Westbrook, C.K. and Dryer, F.L. 1981. Simplified reaction mechanisms for the oxidation of hydrocarbon fuels in flames. *Combust. Sci. Technol.*, 27, 31–43.

Wolfe, D.C. and Byer, R.L. 1982. Model studies of laser absorption computed tomography for remote air pollution measurement. *Appl. Opt.*, 21 (7), 1165–78.

Wu, N. 1997. *The Maximum Entropy Method*. Berlin: Springer.

Yamamoto, K., Isii, S., and Ohnishi, M. 2011. Local flame structure and turbulent burning velocity by joint PLIF imaging. *Proc. Combust. Inst.*, 33 (1), 1285–1292.

Yang, S.Y., Ryu, S.K., Lee, B.K., and Chung, S.H. 2009. Extinction of interacting nonpremixed flames and existence of stationary retreating edges in twin-jet counterflow. *Combust. Theory Model.*, 13 (2), 235–250.

Zhao, Z., Kazakov, A., and Dryer, F.L. 2004. Measurements of dimethyl ether/air mixture burning velocities by using particle image velocimetry. *Combust. Flame*, 139 (1-2), 52–60.

Zhou, B., Zhang, J., and Wang, S. 2011. Reconstruction of flame temperature field with optical sectioning method. *IET Image Process.*, 5 (5), 382.